UNIVERSITY OF CAPE TOWN

An investigation into the influence of autoignition chemistry and charge cooling under ”Beyond RON” operating conditions on the improved knock resistance of ethanol over iso-octane

by Bradley BOCK

Thesis presented for the degree of Master of Science in Engineering
in the Department of Mechanical Engineering,
University of Cape Town

Cape Town, South Africa
May 29, 2013

Abstract

The growing interest in alcohol fuels has led to the finding that benefits in terms of efficiency and power compared to traditional petrols can be gained due to the improved knock resistance of alcohols. This improved knock resistance has been widely credited to the differences in autoignition chemistry and charge cooling caused by the alcohols' high latent heat of vapourisation.

This interest initiated a research project to further understand the influence exerted by the autoignition chemistry and high latent heat of vapourisation in the alcohols' higher knock resistance. Ethanol and iso-octane were chosen as the representative fuels for alcohols and traditional petrols respectively.

The study was conducted through a modelling exercise that made use of experimental data to calibrate subsections of the model and validate the overall model performance.

The experimental investigation made use of a boosted 0.45 ℓ single cylinder Port Fuel Injected (PFI) engine with a specially designed manifold. The manifold allowed for upstream injection of the fuel and recording of the evaporative cooling that occurred along the length. The engine was run under a number of operating conditions and the knock limited spark advance was determined to capture a measure of the knock resistance of the respective fuels at each operating point.

The modelling study consisted of a steady state one-dimensional evaporative model to predict the charge cooling caused by the fuels in the inlet manifold under the various conditions that the fuels were exposed to.

A two-zone zero dimensional combustion model with an empirical knock model was implemented to study the influences of differences in inlet air cooling and autoignition chemistries on the knock resistance.

The modelling study showed that the autoignition chemistry plays the largest role in determining the magnitude of ethanol's advantage over iso-octane. The size of this advantage is dependant on the operating temperatures experienced, with cooler temperature increasing ethanol's advantage. This is due to iso-octane's cool flame phenomenon, which widens the gap in knock resistance between the fuels at low temperatures due to its greater influence under these conditions.

The evaporation modelling showed that there is only a small difference in cooling between the fuels under the conditions they experienced in the test engine. However literature points to direct injection as a technology that may offer the opportunity to take further advantage of the cooling potential of ethanol.

Acknowledgements

I would like to express my gratitude and thanks to all those who helped, guided, advised and endured me during this thesis. I would like to single out a few whose contributions were larger than most:

- Dr. Arthur Bell, with whom I met continually and discussed endlessly while providing guidance throughout.
- Dr. Gareth Floweday, whose experience and advice were invaluable.
- Gerhard Lourens and Toby Rockstroh, who assisted in all things practical involving the Hydra engine and who kept me company down in the lab.
- The other students and staff at the Sasol Advanced Fuels Lab, who were always willing to help when they could or discuss ideas when they were near.
- My patient friends for putting up with me during this work.
- My parents for a lifetime of support.

RATIO OMNIA VINCIT

Plagiarism Declaration

- I know the meaning of plagiarism and declare that all the work in the document, save for that which is properly acknowledged, is my own.
- I have not allowed, and will not allow, anyone to copy my work with the intention of passing it off as his or her own work.

Bradley Denis Bock

Table of Contents

List of Figures

List of Tables

List of Acronyms

AF Air/Fuel

CAD Crank Angle Degrees

CFR Co-operative Fuels Research

CR Compression Ratio

DI Direct Injection

DISI Direct Injection Spark Ignition

E100 100% ethanol fuel

EVO Exhaust Valve Open

FPGA Field-Programmable Gate Array

IMEP Indicated Mean Effective Pressure

IVC Inlet Valve Closure

KA Knock Amplitude

KL Knock Limit

KLMP Knock Limited Maximum Pressure

KLSA Knock Limited Spark Advance

KO Knock Onset

MBT Minimum advance for Best Torque

MFB Mass Fraction Burnt

MON Motor Octane Number

NA Naturally Aspirated

NEDC Normalised European Driving Cycle

NTC Negative Temperature Coefficient

OI Octane Index

OR Octane Requirement

PFI Port Fuel Injected

PRF Primary Reference Fuel

REG Residual Exhaust Gas

RON Research Octane Number

RPM Revolutions per Minute

SI Spark Ignition

SMD Sauter Mean Diameter

VVT Variable Valve Timing

WOT Wide Open Throttle

Chapter 1

Introduction

1.1 Background

Internal combustion engines, despite the age of the central concept, play a large role in modern transport needs. Despite the resurgence of many competing power-train technologies in light of concerns over global warming and crude oil prices, the internal combustion engine is expected to continue being the dominant vehicle power-train over at least the next decade [1].

Continuous research over the decades has meant that while Spark Ignition (SI) engines still rely on the same basic principles as their earliest counterparts, vast improvements in terms of power, efficiency and reliability have been made. More recently, research interest has been shown in highly boosted fuel injected engines [2] , as these engines offer advantages when replacing much larger engines with smaller more fuel efficient counterparts that produce equivalent power outputs.

The aforementioned pressures have however renewed interest in finding alternative fuels for internal combustion engines. Alcohols, such as methanol and ethanol, are one group of non-crude derived fuels that have garnered significant interest due to their properties that suit operation in SI engines [3–7].

This thesis was born out of the growing interest in the operation of these highly boosted engines on alcohol fuels [3–7]. These engines have shown improved efficiency and power when operated on alcohol fuels compared to traditional petrols, or alcohol fuels running in more traditional naturally aspirated engines.

This is achieved by the alcohol fuels having greater knock resistance than traditional petrol fuels in these highly-boosted engines, allowing for the engine to be operated under conditions that allow for greater fuel efficiency. Traditional petrols are unable to operate under these high efficiency conditions as they are limited by knock [3–7].

The improved knock resistance offered by alcohol fuels over traditional petrols has been widely attributed to the increased charge cooling brought about by the high latent heat of vapourisation of the alcohols as well as the autoignition chemistry they possess [3–6].

Understanding the interplay between these two characteristics is important for fuel companies such as Sasol, as they need to understand these modern engines and their preferred fuel appetites to understand the future requirements their fuels may have. This may also present opportunities or restrictions for fuel companies and so further knowledge is vital for decision making.

Thus the goal of this research was to further understand the role that the alcohol fuels' high latent heat of vapourisation and autoignition characteristics have in increasing their knock resistance over traditional petrols in highly boosted injection engines.

1.2 Dissertation Approach

The approach taken was to make use of a mathematical model to simulate the described phenomena. This model was verified against and tuned with experimental runs on a boosted port-fuelled single cylinder research engine. Specifically the focus of the modelling and experimentation was the differences between alcohol fuels and traditional fuels.

Additionally, with the focus of the investigation was on the charge cooling resulting from the heat of vapourisation and autoignition chemistry effects, the experimental set-up allowed for the physical separation of the charge cooling effects from the autoignition chemistry effects.

Ethanol and iso-octane were chosen to represent the alcohol fuels and traditional petrols respectively for this study. (This is discussed further in Chapter 3.1.2.)

1.3 Objectives

The objective of this dissertation was to investigate the reason for alcohol fuels' improved performance over traditional petrols in highly-turbocharged fuel injected engines, with the focus on the influences of the autoignition chemistry and the charge cooling.

The experimental investigation was required primarily to provide data for the verification of the mathematical modelling, and secondarily to provide a physical indication of the influence of charge cooling and autoignition chemistry.

The modelling investigation was required to simulate the data gathered to validate its functioning and then to provide insight into the differing roles played by charge cooling and autoignition chemistry in alcohol fuels and traditional petrols.

Chapter 2

Literature Review

A review of literature concerning the central aspects of this thesis was conducted and is documented here. A background to knock in Spark Ignition (SI) engines was covered, followed by an overview of the charge preparation of modern engines. The interplay between knock and modern engine technologies was reviewed, focusing on the idea of engine operating regions and particularly the so called ”Beyond RON” region, current engines and their operation in this region and the research into opportunities that have been identified in this field. A review of fuel and its influence in knock was conducted. Lastly a review of modelling techniques that would be required for the evaporation and combustion modelling was conducted.

2.1 Knock in Spark Ignition Engines

2.1.1 Introduction to Knock

Knock is an abnormal combustion phenomena that occurs in SI engines, traditionally identified by a sharp metallic ringing sound. During regular SI engine operation, a flame front propagates from the spark plug outwards, consuming the unburnt charge in a controlled fashion. This flame front compresses the unburnt charge, raising its temperature and pressure. Knock occurs when this temperature and pressure rise causes the unburnt gas to autoignite before it is consumed by the flame front [8].

The combustion resulting from this autoignition is different from the combustion produced by the spark induced propagating flame front. Whereas the spark-induced flame front progressing through the chamber results in a controlled pressure rise, knock causes a rapid pressure rise rate that results in pressure waves that bounce off the cylinder walls, producing the characteristic ringing sound [8]. This knock phenomenon results in an increased heat flux to the engine wall and local pressure pulses, both of which can damage an engine [9]. It is this damage caused by knock that makes it such an important design consideration for SI engines, limiting the maximum Compression Ratio (CR) that can be used for a given combustion chamber size and design [8].

Knock is thus an important consideration in SI engines as it is an inherent design constraint on these engines, limiting power and thermodynamic efficiency [8].

Spark knock is not to be confused with the variety of other pre-ignition events that can occur in an engine, such as ping and pre-ignition. These are not initiated by the mechanism described above and can often be solved through appropriate engine design. See Heywood [8] for a further description of these. Throughout this work the term “knock” will be used to describe only the end gas autoignition phenomenon described here rather than any of the other pre-ignition phenomena.

2.1.2 Engine Operating Influences on Knock

Knock resistance describes the difficulty at which knock occurs. A fuel with high knock resistance would thus not knock or knock less under the same conditions as a fuel with low knock resistance.

The tendency for knock to occur is affected by parameters that influence the end-gas temperature-pressure history and the time spent under these conditions [8].

The fuel used, the engine operating conditions and the engine geometry are all parameters that influence knock suppression. The influence that fuel plays will be discussed in Chapter 2.5.

Increases in CR, inlet temperature and inlet pressure all tend to increase the propensity of the end gas to knock. Air/Fuel (AF) ratio also influences knock propensity, with the highest being for a slightly rich mixture and decreasing if the mixture is further leaned or enriched about this point. [8].

Spark timing affects peak cylinder pressures and temperatures. As the spark timing is advanced (that is, as the spark plug fires earlier in the compression stroke), the in-cylinder peak pressures and temperatures are increased, thus increasing the tendency for knock to occur. However at the same time, this advanced timing increases engine torque output and fuel efficiency, up until a point known as Minimum advance for Best Torque (MBT) timing. The spark timing can be easily changed and so it is usually the first control parameter used to regulate or reduce knock, at the expense of torque output and fuel efficiency [8].

An engine is generally less prone to knock as speed increases due to the shorter time available for the end gas to autoignite. However, the knock resistance of different fuels respond differently to changes in speed. This is dealt with further in Chapter 2.5, as it covers the relationship between fuels and knock.

2.1.3 Introduction to Autoignition

The autoignition characteristics of fuels are important as the fundamental theories of knock are based on models of the autoignition [8] of the end gas during combustion.

Autoignition describes rapid combustion that is not brought about by an external ignition source. It only occurs if the combustion material temperature is above a

certain limit for a period of time (often in the range of milliseconds) [8]. The time taken for a substance to autoignite after being rapidly raised to a specific temperature and pressure is known as the autoignition delay (τ).

Autoignition delay is a function of temperature, pressure, equivalence ratio and fuel type, among others, [8] and different fuels vary both in magnitude and sensitivity to these factors.

Temperature increases generally decrease the autoignition delay time; however this is not always the case for all fuels. Figure 2.1 shows a typical plot illustrating n-heptane's autoignition delay response to temperature and pressure, where it can be seen that a temperature range exists in which an increase in temperature causes an increase in autoignition delay. Further discussions concerning this important phenomenon are found in Chapter 2.5.1.

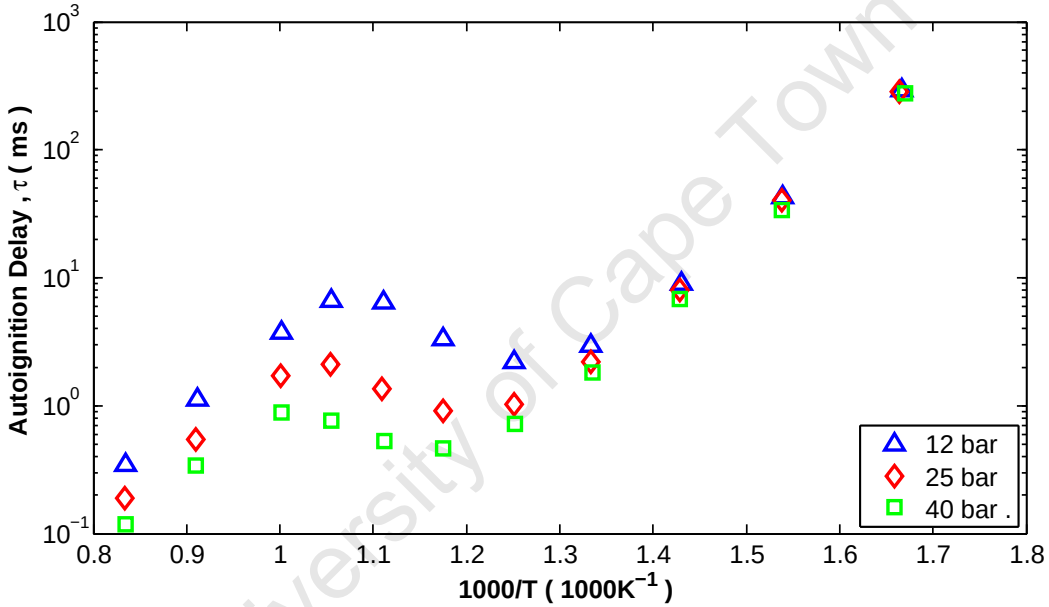

Figure 2.1: Autoignition delay of n-heptane at various pressures and temperatures (Taken from [10])

2.1.4 The Octane Number Scales

A standardised method to quantify the knock resistance of petrol fuels was required as research into this field increased in the early and middle 20th century [11]. This resulted in the octane rating scale to quantify a fuel's resistance to knock.

The octane scale was developed by using a blend of two fuels, 2,2,4-trimethyl-pentane (commonly referred to as iso-octane) and n-heptane as a standard for comparison. These two fuels, with similar physical properties but greatly differing knock resistances , were designated the Primary Reference Fuels (PRFs). iso-Octane, with a high knock resistance, was assigned an octane number of 100 and n-heptane, with its low knock resistance, an octane number of 0. The octane number of a PRF blend

was defined as the volume of iso-octane in a PRF blend (a 67/33 % volume blend of iso-octane/n-heptane has an octane number of 67 and is referred to as a PRF 67) [8].

The knock resistance of a fuel is determined by increasing the CR of a standardised Co-operative Fuels Research (CFR) engine until knock occurs at a specific level. Then a PRF blend is found that matches the fuel's knock propensity [8] and the fuel is given the octane number of the PRF blend.

As knock resistance is dependant on engine operating conditions, standardised conditions were required. Two sets of operating conditions were finally settled on with each set producing its own octane number, namely the Research Octane Number (RON) and the Motor Octane Number (MON). The most important respective conditions for each test can be seen in Table 2.1, while the full details of the determination of the RON and MON numbers can be found in the ASTM D2699 [12] and ASTM D2700 [13] standards respectively.

Table 2.1: Octane number operating condition

	RON	MON
Test Method	ASTM D2699	ASTM D2700
Test Engine	CFR Engine	
Engine Speed	600 RPM	900 RPM
Ignition Timing	13 °BTDC	Varies with CR from 19 to 26 °BTDC
Inlet Air Temperature	52 °C	38 °C
Inlet Mixture Temperature	Not controlled	149 °C
Air/Fuel Ratio	Adjusted for maximum knock intensity	

Two important points relevant to this work must be kept in mind.

Firstly, the octane number of a fuel compares its knock resistance to that of a PRF, and this is determined under two specific sets of operating conditions. A fuel with a higher octane number for one of the tests does not necessarily always outperform a counterpart under all other operating conditions, as the knock resistance of fuels respond differently to changes in operating conditions, for reasons that are discussed further in Chapter 2.5.2.

Secondly, the knock resistance of a fuel, and thus its octane numbers, are not only a function of its autoignition characteristics but also the charge cooling that it causes through the evaporation of the fuel during the inlet and compression process. This particularly applies to the RON test, where only the inlet air temperature is controlled. The MON test requires the inlet mixture temperature to be controlled, which has been shown [14] to remove all of the charge cooling capabilities of a fuel.

2.1.5 Knock Limit

There are a variety of approaches to quantifying the severity of knock so that useful comparison between knock data can be performed.

Knock quantification in laboratory work where in-cylinder pressure measurements are available often make use of the peak amplitude of the pressure oscillations, designated the Knock Amplitude (KA). This amplitude is a useful measure as it depends on the amount of end gas that undergoes autoignition [8]. This KA is obtained by extracting the high frequency pressure oscillations caused by knock through the use of a high pass filter, in the range of 3 to 10 kHz, depending on the cylinder geometry [8].

A limit may be set to this KA, known as the Knock Limit (KL). As KA varies greatly from cycle-to-cycle [8], this KL must incorporate an averaging mechanism over a number of engine cycles.

A number of differing KLs have been used in literature:

- Rothe et al. [15] defined a limit where over 3000 cycles, 1% of the cycles have a knock amplitude greater than 4 bar.
- Kalghatgi [16] defined a limit where over 400 cycles, the cycles have an average knock amplitude of 0.5 bar.
- Mittal and Heywood [17] defined a limit where over 400 cycles, 50% had 6kHz pressure oscillations greater than 2 bar.

2.2 Charge Preparation

2.2.1 Boosting

To boost the power of a particular sized SI engine, the density of the inlet air can be raised by increasing the inlet air pressure.

The two most common methods of boosting are turbocharging and supercharging, both of which make use of a compressor to boost the inlet air pressure. Turbocharging drives the inlet air compressor with power derived from a turbine placed in the exhaust gas, while supercharging drives the inlet air compressor with power from the engine crankshaft [8].

Boosting is advantageous to SI engines as it provides a more fuel efficient engine for a fixed power output. Boosting an engine causes it to have a higher specific power output, meaning that a smaller boosted engine can output the same peak power at the same speed as a larger Naturally Aspirated (NA) engine. During normal driving, when an engine is operated under part load, the turbocharged smaller engine provides better fuel efficiency as it has reduced pumping losses and better mechanical efficiency [18].

A turbocharged engine also benefits from the mass savings compared to a larger NA engine with the same peak power output [2].

Turbochargers have the added benefit of utilizing the exhaust gas energy to power the compression process, allowing them an efficiency advantage over supercharging [19].

These advantages are however limited by knock considerations, as increasing the inlet pressure increases the engine's tendency to knock (as mentioned in Chapter 2.1.2).

Thus, while a naturally aspirated engine may have sufficient margin of safety in terms of knock to allow mild boosting, changes would have to be made in terms of its design or operating conditions to decrease knock if higher boosting was implemented [8].

The compression of the inlet charge however also leads to an increase in temperature. This is not favourable, as knock is highly dependent on inlet air temperature, as discussed in Chapter 2.1.2. To overcome this, as well as to provide a further density increase, inter-cooling can be employed to reduce the compressor outlet temperature [19].

2.2.2 Charge Cooling in Engines

Fuel Delivery

The method of fuel delivery influences the amount of charge cooling the air experiences due to fuel evaporation. This in turn influences engine performance as the decreased temperature of the inlet gas results in suppression of knock in the end gas, as well as the air density increase that increases the volumetric efficiency of the engine.

Two of the most prevalent current fuel delivery technologies in SI engines will be reviewed here, namely Port Fuel Injected (PFI) and Direct Injection (DI) systems. Figure 2.2 illustrates the two technologies.

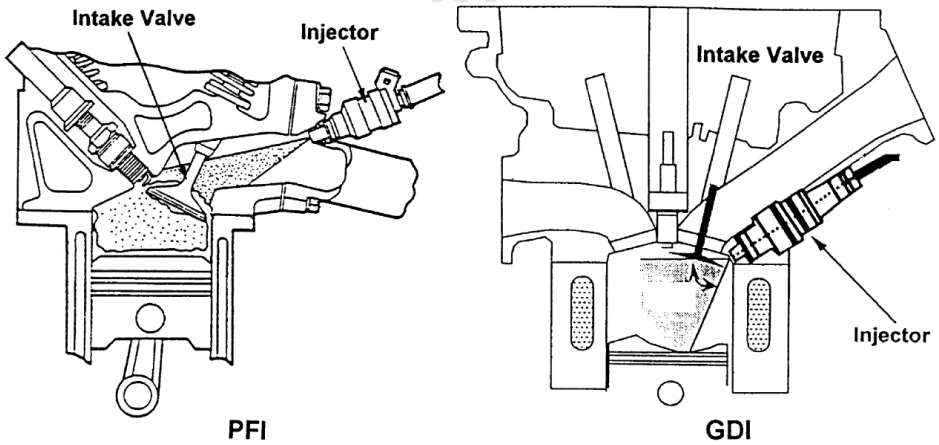

Figure 2.2: Illustration of a PFI system and a DI system (reproduced from [20] and [21])

PFI involves the injection of fuel into the inlet port of the engine. Most modern PFI engines direct this fuel spray onto the back of the inlet valve when the valve is closed, just prior to the valve opening [22]. This means that there is a time lag between the injection and the induction of the fuel into the cylinder.

PFI results in wall wetting of the port wall and a build-up of a wall film. This wall film reduces the transient response of the engine AF ratio control [22]. Wall wetting also

reduces the maximum possible cooling of the air as the wall film gains vapourisation energy from the hot port walls rather than the air.

DI injects the fuel directly into the cylinder during inlet and compression, depending on the timing strategy involved, thus reducing the degree of wall wetting.

This decreased amount of wall wetting and reliance on wall film evaporation provides enhanced control of transient fuel metering, so allowing for lower emissions and better transient response [23]. It should be noted that wall wetting is still present in DI engines, especially for injection strategies that make use of wall-guided combustion chamber concepts [23], and has been found to be particularly relevant when injecting fuels that have high latent heats of vapourisation [24].

DI also offers the benefit of providing greater charge cooling. This is also achieved by the lower amounts of wall wetting as well as a greater degree of fuel atomization that increases fuel droplet vapourisation rates while airborne [23]. This results in greater knock suppression through lower end gas temperatures and greater volumetric efficiency through denser inlet charge [23].

PFI does offer some advantages over DI, such as a less complex fuel delivery system and lower particulate emissions [23].

Improvements in fuel delivery systems have increased the amount of charge cooling possible with a fuel.

Anderson et al. [25] demonstrated this when they compared PFI and DI systems running on iso-octane. Tests were conducted on a single-cylinder engine at Wide Open Throttle (WOT), stoichiometric air fuel ratio and running at 1500 Revolutions per Minute (RPM). They showed that DI had a volumetric efficiency improvement of between 2-3% over PFI and a part load fuel consumption improvement of 4-5%. This is because of the increased charge cooling that DI allows, and the subsequent improvement in Knock Limited Spark Advance (KLSA) possible due to lowered charge temperatures.

Wyszynski et al. [26] conducted tests on a single-cylinder engine and found that DI offered an approximately 9-12% improvement in volumetric efficiency over PFI at 1000 RPM, WOT. Wyszynski et al. noted this improvement could be theoretically higher, but is limited by the finite time for evaporation and the direct impingement of the fuel spray onto the combustion chamber, which causes the fuel to cool the chamber walls rather than the charge.

Fuel Latent Heat of Vapourisation

Changes in fuel composition or type influence the charge cooling through the greater heat of vapourisation that is available to cool the charge during evaporation.

Szybist et al. [27] conducted research on ethanol-petrol blends in a DI engine and illustrated the potential of fuels with greater heat of vapourisation values. They found that E85 (85% ethanol blend with petrol, by volume) had an approximately 2% greater air flow than regular petrol. This can be attributed to the charge cooling effect increasing the density of the incoming air, allowing more air mass to enter the cylinder.

Nakata et al. [4] shows that when using alcohol fuels in non-DI engines, volumetric efficiency can in fact decrease. A PFI vehicle fuelled on 100% ethanol fuel (E100) had a decreased volumetric efficiency of approximately 2% compared to a petrol. This is due to ethanol's stoichiometric AF ratio of 9 as compared to petrol's of approximately 15, resulting in the ethanol vapour occupying a greater proportion of inlet charge and so reducing the amount of air that could be drawn into the engine. A DI engine is able to offset this due to improved charge cooling, as demonstrated by Szybist et al. [27].

2.3 Modern Engines and Knock

2.3.1 Octane Index

The Octane Index (OI) is a measure used to capture the knock resistance of fuels under operating conditions experienced in commercial automobile engines.

The OI represents the octane number of a PRF that would have the same knock resistance at the given operating condition of the fuel in question [16]. Thus the OI of a fuel in the CFR engine under the RON and MON operating conditions are the fuel's RON and MON numbers respectively.

The OI is mathematically described as a function of RON and MON with a K weighting factor, and is defined as [16]:

$$OI = (1 - K)RON + K \cdot MON \tag{2.1}$$

where OI : Octane Index
RON : Research Octane Number
MON : Motor Octane Number
K : weighting factor

From the definition it can be seen that the OI quantifies the knock resistance of a fuel by using the RON and MON numbers as two set points and linearly interpolating or extrapolating the octane resistance of the fuel to the operating condition it finds itself in. The K factor acts to weight where the engine operating conditions is in relation to the two octane test conditions. It should be noted that this K factor is only able to be defined if the engine is operating under knock limited conditions.

The K factor is thus assumed to be dependant only on operating condition [16] relative to the operating conditions of the RON and MON tests, and is not a characteristic of the fuel. By definition a K value of 1 indicates the operating conditions match those of the MON test, while a K value of 0 means that the operating conditions match those of the RON test. K values between 0 and 1 indicate intermediate operating conditions. K is not bound however and K values less than 0 or above 1 indicate that conditions are now moving beyond the range of operating conditions that the RON-MON tests bracket.

The Octane Requirement (OR) describes the maximum octane required by an engine at a certain operating condition for no knock to occur [16]. It is thus the octane number of the PRF that would just allow for the engine to operate at its MBT timing. If the OI of the fuel is greater than the OR of the engine at a certain operating condition, the engine can run knock-free at MBT timing and is thus not limited by the fuel in terms of power, performance and efficiency.

To calculate K and the OI at a specific operating condition in an engine, a quantitative measure of the knock resistance of a number of fuels is needed, such as KLSA or Knock Limited Maximum Pressure (KLMP).

The knock resistance indicator of the fuel is then correlated to OI. A K value is then found, through linear regression, that provides the best fit for this correlation [16]. The full method and derivation of the correlation used to calculate K and OI is detailed in Appendix B.6.

2.3.2 Influences on K

Mittal and Heywood [17] experimentally explored the dependence of K on spark location, CR, AF ratio, engine speed, intake air temperature and intake pressure and showed that of these parameters, K is strongly dependant on intake air temperature, engine speed, air fuel ratio and intake pressure.

They showed that K increases with increases in inlet air temperature and that K decreases for increases in inlet air pressure. Kalghatgi [16] showed that with the RON test (where K = 0) generally having conditions of lower peak temperatures and higher peak pressures with respect to the MON test (K = 1), we would expect parameters that lower the temperature and increase the pressure of the end-gas to decrease K, and vice versa. The above findings of Mittal and Heywood corroborate this reasoning.

Mittal and Heywood [17] found that decreases in speed decrease K, which is confirmed by Kalghatgi in various works [16, 28, 29].

Mittal and Heywood [17] found that K depends on air fuel ratio, with K being the highest at stoichiometric conditions and decreasing to either side. This is corroborated by Kalghatgi in [16].

Mittal and Heywood [17] found that increasing the CR weakly decreased K, which was noted to disagree with results from Kalghatgi's work [16, 28], where a strong correlation was found. Mittal and Heywood suggested that this discrepancy may be have been caused by differences in the calculation of the OI by the two groups of authors. Kalghatgi however pointed out in a later work [29] that increased CR resulted in a decrease of K due to the reduced levels of hot residuals mixing with the new charge.

Additionally, Mittal and Heywood noted that as K is expected to be only dependant on operating condition, and is defined as a constant value at the RON and MON conditions, they hoped that it would be independent of CR, as the CR is changed when determining the RON and MON numbers of a fuel. Thus two fuels with different RON

numbers would be subjected to different CRs but both conditions would be defined as having occurred at a K value of 0.

This issue merits further investigation, especially if the use of the OI gains popularity.

Kalghatgi [16, 28] found that K tended to decrease when changing the throttle setting from part throttle to WOT or increasing the CR of an engine, while holding all other operating conditions constant. Kalghatgi subsequently concluded that "as the operating conditions change to make the engine more prone to knock the value of K decreases" [16]. As already described, the increase of inlet temperature makes the engine more prone to knock and increases the value of K, which contradicts the previous statement of Kalghatgi's.

A possible reason for Kalghatgi's above correlation may be that while increasing the CR and moving to WOT both increase the temperature and pressure of the end gas, the pressure increase may outweigh the temperature increases influence on the K value, as increases in inlet pressure have been found to decrease K. This relationship however requires further investigation.

2.3.3 Current Engines' Octane Appetite

The "Beyond RON" regime refers to the operating regime where K is negative. The operating regimes of production engines, which started at a value of approximately 0.5 in the early 20th century [17], have dropped during the late 1980s [29] and a number of studies [16, 17, 29, 30] have shown that modern engines operate under primarily negative K conditions.

This can be attributed to the direction that modern vehicle technology in SI engines has moved in, with the use of higher CRs, DI and turbocharging with intercooling. These have moved the operating ranges of engines towards lower temperatures and higher pressures, which result in these more negative K values.

In studies conducted on Japanese and European cars (consisting of turbocharged and Direct Injection Spark Ignition (DISI) vehicles) operating under knock limited conditions, most operating conditions were found to have negative K values [30]. In a study of a commercial DISI engine and a single-cylinder DISI engine, Kalghatgi et al. [28] found that most knock limited conditions had negative K values. Mittal and Heywood [17] found similar results for a single-cylinder turbocharged engine.

As these engines operate in pressure and temperature regimes that produce negative K values, we can deduce that they would prefer fuels with larger octane sensitivities (a sensitive fuel being one with a large difference between RON and MON numbers. This is dealt with in detail in Chapter 2.5.2). This is because, referring to Equation 2.1, we can see that for two fuels with the same RON, a smaller MON produces a higher OI if K is negative.

2.3.4 Taking Advantage of "Beyond RON"

A number of computational and engine studies have been conducted to show the potential of "Beyond RON" engines when run on sensitive fuels. They gain their advantage from making use of the higher OI of sensitive fuels when operating under negative K conditions. This subsequently allows them to operate under higher CRs and inlet pressures, allowing for greater engine thermal efficiency.

Downsized Highly Turbocharged Engines

Downsized highly turbocharged engines are designed for higher specific power output by operating in the "Beyond RON" region where they can take advantage of a fuel's increased OI in this region due to its sensitivity. These small turbocharged engines have a number of other advantages over larger NA engines with the same peak power output. These include greater mechanical efficiency due to reduced friction losses as a result of the small size, improved thermal efficiency over an urban drive cycle as less throttling is required to achieve the same part loads as the larger NA engine and reduced heat losses resulting from the exhaust heat recovery of the turbine [18].

Attard [2] calculated using that using his 0.43ℓ prototype downsized turbocharged engine to replace the 1.25ℓ normally aspirated engine in the 2007 Ford Fiesta would produce a 22% reduction in fuel consumption and CO_2 emissions over the Normalised European Driving Cycle (NEDC) while producing similar power outputs. This calculation was done through the use an empirical correlation developed by Beer et al. [31] to determine the influence of vehicle mass on fuel consumption over the NEDC.

The benefits seen are thus calculated based on the lower vehicle mass and the engines better fuel consumption due to its ability to run closer to peak efficiency for longer. Attard noted that the results of the downsized engine were based on experimental runs made on 98 RON fuel, while the Fiesta engine was run on 95 RON pump petrol. These results are thus somewhat misleading, as it is difficult to quantify the influence the improved RON number had on the downsized engine's performance.

Petitjean et al. [32] conducted a study to investigate the benefits that downsized turbocharged engines have had in the market. Comparing production sedans over a period of ten years they were able to conclude that downsizing had allowed for a 8-10% improvement in fuel economy in these vehicles while achieving the same power output.

Alcohols in PFI Engines

Alcohol fuels, such as ethanol and methanol blends, have high RON, high sensitivity and large latent heats of vapourisation. As a result, they are ideal for "Beyond RON" engines.

Turner et al. [3] compared a 95 RON petrol against a E85 blend in a 4-cylinder supercharged PFI engine with a CR of 11.5 (E85 has a RON number of approximately

106 [33, 34]). The wet compressor approach was used, with some of the E85 fuel injected prior to the supercharger. A 14% improvement in peak power and 10% improvement in peak thermal efficiency was seen. This was due to the improved spark advance allowed by the E85's larger knock resistance.

Nakata et al. [4] experimentally showed the effects that E100, with a RON of 108.6 [35], has in a PFI engine with the CR raised to 13. They showed that a thermal efficiency of 40% can be achieved with E100 (at 2800 RPM and WOT), compared to the 32% of a 92 RON or the 38% of a 100 RON, an improvement of 25% and 4% respectively. The torque was similarly increased, with a 20% and 5% increase over 92 RON and 100 RON petrol respectively. This was once again due to more advanced spark timing being able to be employed.

They operated the engine at MBT timing when using a blend of E50 fuel, thus satisfying the engine's octane requirement. This means that with the E100 blend they could have improved the efficiency further, through measures such as increasing the CR.

Alcohols in DI Engines

Alcohol fuels are particularly suited to DISI engines for the reasons mentioned previously as well as the increased charge cooling resulting from DI.

Kapus et al. [5] showed in a 2ℓ 4-cylinder turbocharged DISI engine with a CR of 10.5, that E85 allowed for a 20% increase in fuel efficiency over a 95 RON petrol due to the more efficient spark timing it allows for.

Brewster [7] compared 98 RON petrol against E100 (RON : 108.6) in a 2ℓ 4-cylinder Variable Valve Timing (VVT) DISI engine with a CR of 10.4 over a range of speeds with the same output torque. The E100 produced a thermal efficiency that ranged across speeds from approximately 32% to 37% compared to the 98 RON petrol which ranged from approximately 29% to 34% over the same speed range. The improvement in efficiency that E100 provided ranged from 7 to 13%.

Brewster [7] noted that as E100 was not knock limited with MBT timing being employed, while the 98 RON petrol was knock limited, it may be possible to further improve the efficiency of the engine running on E100 through the increasing of the CR or some degree of downsizing.

Alcohols in Large Engines

Alcohol fuels also show promise in larger engines at lower speeds, a particularly challenging operating environment for SI engines due to the high octane requirement.

Brusstar and Gray [6] modified a turbocharged 4.5ℓ V6 diesel truck engine with a CR of 16.3 to a PFI SI engine. Running on E85 a peak thermal efficiency of 40% was achieved while M85 (a fuel blend consisting of 85% volume methanol and the remaining amount petrol) achieved a similar peak thermal efficiency, but over a wider operational range.

These efficiencies are comparable with diesel engines [8], and thus offers possibilities for the replacement of larger diesel engines with these alcohol fuelled engines.

Computational Studies on Alcohol Fuelled Engines

Boretti [36] used the WAVE code developed by Ricardo industries to compare the performance of ethanol and indolene (a petrol surrogate) in a simulated 4-cylinder turbocharged DISI engine with a CR of 13 and 9 for the E100 and indolene respectively. The ethanol was able to provide a peak brake efficiency of about 39% compared to a value of 33% for the indolene, an improvement of 18%.

2.4 End Gas Temperature Effects

Nakata et al. [4] found that at 2800 RPM and WOT, E100 achieved a thermal efficiency of about 39.6% compared to the 37.9% achieved by 100 RON petrol with the same spark timing, an improvement of 4.5%. They measured the in-cylinder combustion temperatures under the same conditions and showed that ethanol has the lower combustion temperature of the two fuels. They attributed the greater thermal efficiency achieved by ethanol to this lower combustion temperature and the resulting reduction in heat loss from the combustion chamber. Nakata et al. ascribed the lower combustion temperatures to the greater proportion of triatomic molecules present in the products of ethanol combustion. This results in a higher heat capacity of the products of ethanol combustion and so lower combustion temperatures.

Another contributing factor to this lower combustion temperature that Nakata et al. did not mention is that the lower heating value for a stoichiometric mixture of ethanol and air is 2% [8] less than that of iso-octane.

Szybist et al. [27] further highlight this advantage that ethanol has in terms of greater thermal efficiency over regular petrol under the same engine conditions. A DISI engine with a CR of 9.2, throttled to 80 kPa absolute inlet manifold pressure, was used to show that E85 increased the thermal efficiency compared to petrol from approximately 34% to 37%, an improvement of approximately 8%.

Szybist et al. attribute this increased thermal efficiency to possibly two main influences. Ethanol blends have a lower ratio of number of moles of product to number of moles of reactant than regular petrol. As a result, lower combustion temperatures are achieved, which can be inferred from the ideal gas law. Ethanol blends also produce a lower ratio of specific heats for AF mixtures than petrol, and this too may have an influence, although the full extent is unknown.

2.5 Fuel and Knock

Fuel influences knock resistance chiefly through the direct influence of the fuel chemical autoignition kinetics as well as the indirect influence on these kinetics that the heat of vapourisation of the fuel has by cooling the charge and thus delaying autoignition.

2.5.1 Chemical Influences on Knock

Knock, being an autoignition phenomenon, is thus influenced by the fuel's own particular autoignition chemistry. Figure 2.3 illustrates the autoignition delay times versus temperature of a variety of fuels, highlighting both the differences in response to temperature change as well as differences in absolute magnitude at particular temperatures.

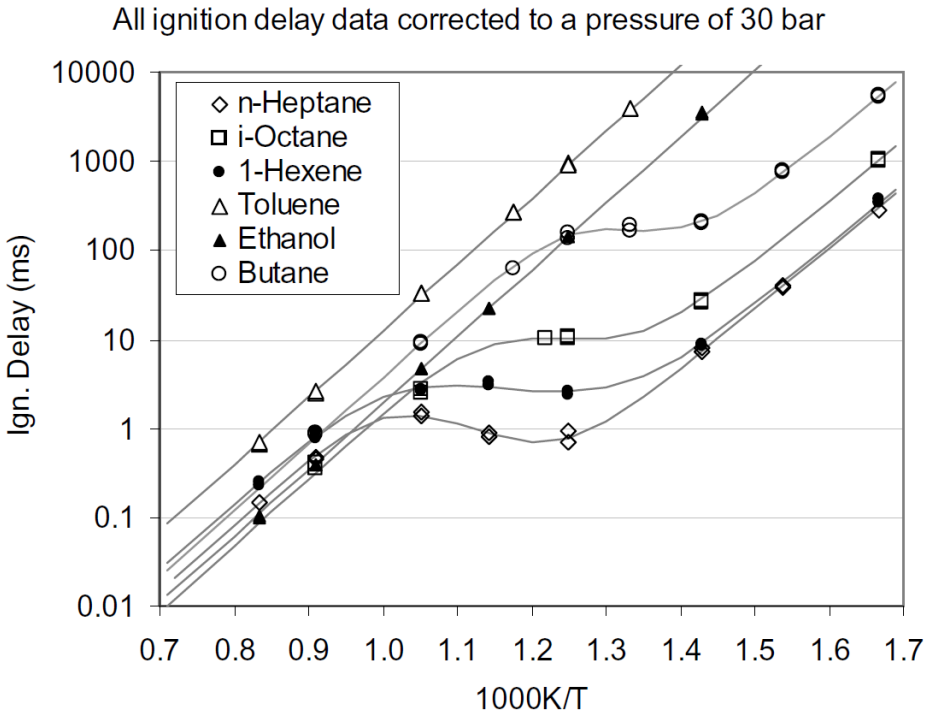

Figure 2.3: Autoignition delay of various fuels (reproduced from [37])

The detailed process of autoignition is beyond the scope of this work. However the phenomena of single stage and two stage autoignition is of relevance, as it has a strong influence on the autoignition profiles of a number of fuels. Figure 2.3 highlights this phenomenon, seen by the two distinctive profiles that are present, namely the straight line profiles of fuels with single stage autoignition and the 'S' shaped profiles of the fuels with two stage autoignition.

The autoignition chemistry of fuels that exhibit a single stage of autoignition, viz. single-stage fuels, produce an autoignition delay characterized by a relatively constant temperature, followed by combustion characterized by a exponential temperature rise.

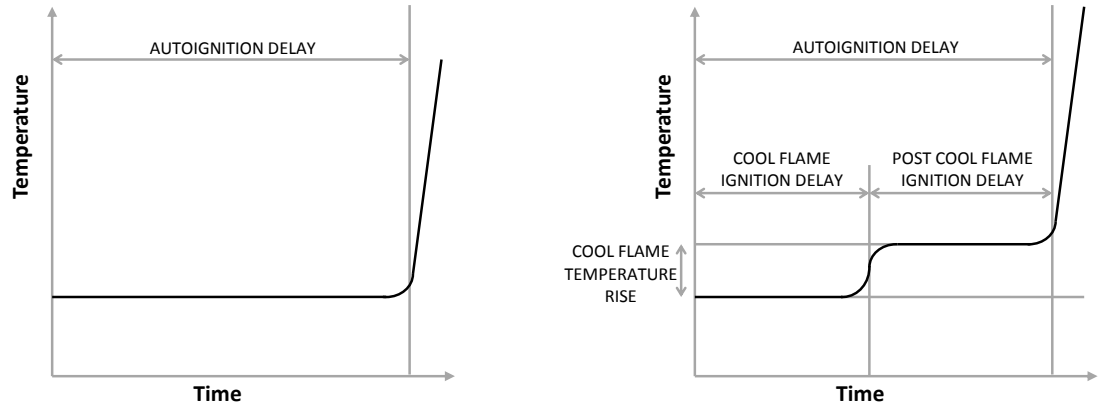

(a) Single-stage fuel (b) Two-stage fuel

Figure 2.4: Representation of the temperature history for a single stage fuel and a two stage fuel

Two-stage fuels however exhibit a two stage autoignition process under certain conditions. This two stage ignition consists of an initial period, the pre cool flame delay, of negligible exothermic chemical activity, during which the temperature of the fuel-air mixture remains relatively constant. Then an abrupt temperature jump occurs, the so called “cool flame”. After this there is another period of relative temperature stability, the post cool flame delay. After this, the fuel fully autoignites producing a sharp rise in pressure and temperature. [38]. Figure 2.4 shows an idealised temperature history of a two-stage fuel and a single-stage fuel.

The result of these differing autoignition processes manifest themselves through the fuels’ overall autoignition delay response to physical conditions.

Single-stage fuels, such as methanol and toluene, exhibit steadily decreasing autoignition times as temperature increases, producing the characteristic straight line relationship when plotted as in Figure 2.3. (It should be noted this is an exponential relationship, as the plot is a logarithmic one).

Two-stage fuels, such as iso-octane and n-heptane, have two regions where autoignition times decrease with temperature, with an intermediate region where autoignition delay has a negative or near constant relationship with temperature, producing the characteristic “S” shaped plot, as seen in Figure 2.3. The intermediate region where autoignition delay may exhibit a negative or decreasing dependency on temperature is known as the Negative Temperature Coefficient (NTC) region.

This characteristic “S” shape is produced by the cool flame phenomenon’s influence. The cool flame phenomenon is shown to decrease the autoignition times of two-stage fuels in the low temperature region. The chemical cause of this phenomenon is associated with an underlying temperature dependant equilibrium reaction [39]. This results in the straight line that is offset from the high temperature section’s straight line by the decrease in overall autoignition delay that the cool flame causes [40].

As temperatures increase, this cool flame phenomenon becomes less prominent and

its ability to accelerate autoignition diminishes. This transition NTC region thus occurs as the cool flame influence peters out. Finally, the high temperature section is a straight line, where the cool flame has no influence [40].

2.5.2 Fuel Sensitivity

Fuel sensitivity is essentially the sensitivity of a fuel's knock resistance to the different operating conditions of the MON and RON tests compared to the PRFs [17].

It is witnessed in the octane tests in that many fuels do not have the same knock resistance under the RON and MON conditions in comparison to the PRFs (as demonstrated by Table 3.1, showing the octane numbers of the fuels used in this study). This difference in performance, and thus difference in octane numbers, is known as sensitivity. It is defined as the difference between the RON and MON numbers, as seen in Equation 2.2.

$$S = RON - MON \tag{2.2}$$

where S : sensitivity
RON : Research Octane Number
MON : Motor Octane Number

The exact causes of fuel sensitivity and their relative influence is still not fully understood. Both the differences in fuel chemistry and heat of vapourisation of fuels compared to the PRFs have been attributed to causing this sensitivity.

Leppard [38] attributed the fuel sensitivity to the NTC behaviour shown by the paraffinic PRFs compared to the lack of NTC behaviour of the sensitive fuels studied in his work.

Mittal et al. [41] investigated the underlying chemistry behind fuel sensitivity. They found that for the fuels investigated, those whose autoignition delay had a stronger dependence on temperature in a transition regime between 775 K and 900 K were more sensitive. This is analogous to attributing the fuel sensitivity to a lack of NTC region being present, as the NTC region is identified by a lower dependence of autoignition delay on temperature (Chapter 2.5.1).

The influence that charge cooling may have on fuel sensitivity was however not considered by either Leppard or Mittal et al.

Charge cooling may play a part as fuels with greater heat of vapourisation than the PRFs may produce greater cooling under the RON conditions and thus improve the antiknock resistance of the fuels. This is due to the differences in the inlet air temperature control of the RON and MON, as discussed previously. From this, we could expect fuel with higher heat of vapourisation than the PRFs to perform better under the RON conditions than the MON conditions. Interestingly enough, often fuels with high heat of vapourisation are single-stage fuels with large sensitivities.

Moran and Taylor [42] investigated the influence of charge cooling and came to the conclusion that fuel sensitivity can be completely attributed to this effect. The study

used a steady state evaporative model to determine the reduction in inlet temperature due to fuel evaporation and the subsequent increase in CR required to have the same peak in-cylinder temperature. The change in octane number that can be related through the octane guide tables to this change in CR was thus the resultant contribution of the charge cooling to fuel sensitivity. Moran and Taylor applied this method to a number of fuels with varying heats of vapourisation and achieved good agreement.

Their analysis method however took no note of chemical factors or the influence of the temperature-pressure history on knock, instead assuming that equivalent end temperatures equate to equivalent knock.

2.5.3 Separation of Fuel Influences on Knock

The separation of the relative influence of the autoignition and charge cooling properties of a fuel on knock suppression is still not fully understood. The relative contributions of these two influences may also be expected to change for different fuels and under different operating conditions.

Octane Test Conditions

Research into understanding fuel sensitivity, as discussed in the previous chapter, unintentionally provides insight into this question. The octane numbers produced by the octane tests are influenced by both a fuel's autoignition and charge cooling properties. In particular, as the MON test specifies a high mixture temperature and so removes a fuel's charge cooling [14], while the RON test has a inlet air temperature specification and not mixture specification, which we would expect to allow some influence of a fuel's charge cooling.

Thus, the understanding of fuel sensitivity would provide insight into the relevant influences of the these two phenomena.

As discussed in the previous chapter, Moran's work [43, 44] indicates that charge cooling fully accounts for these differences while Leppard [38] and Mittal et al. [41] considered only the chemical influences in explaining sensitivity.

Beyond RON

Work conducted by Milpied et al. [45] was the only work of direct relevance that could be found on the topic of separating the influences of fuel autoignition chemistry and charge cooling on knock suppression in the "Beyond RON" operating regime. However the paper looked specifically at separating the influence of the properties of octane number and heat of vapourisation. These two properties are strongly linked to but not the same as autoignition chemistry and charge cooling.

Their approach was to use fuel matrices consisting of fuels with varying values of RON, MON and heat of vapourisation to separate these properties' influence on knock

resistance. They conducted tests in a single-cylinder 300 cm^3 downsized turbocharged DISI engine, with an Indicated Mean Effective Pressure (IMEP) of up to 30bar. Knock resistance was quantified by the IMEP achievable at KLSA. No indication of the levels of boost used during the study are given.

While no K analysis was performed for this study, we would expect that these tests were run in the “Beyond RON” regime, as they were conducted in a downsized DISI engine, and as discussed in Chapter 2.3.3, these types of engines are found to mostly operate in the Beyond RON regime when knock limited.

Figures 2.5 and 2.6 reproduce the results of this study. The ”Fuel impact” quantity quoted on the vertical axes is a measure of the impact that particular fuel property graphed has on knock resistance. It is calculated as the ratio of the knock limit load (in bar) to the particular fuel property, namely the RON number, MON number or cooling power of the fuel, in kJ/kg. The cooling power of the fuel is defined as the energy that would be taken from the stoichiometric air-fuel mixture by the complete vapourisation of the injected fuel.

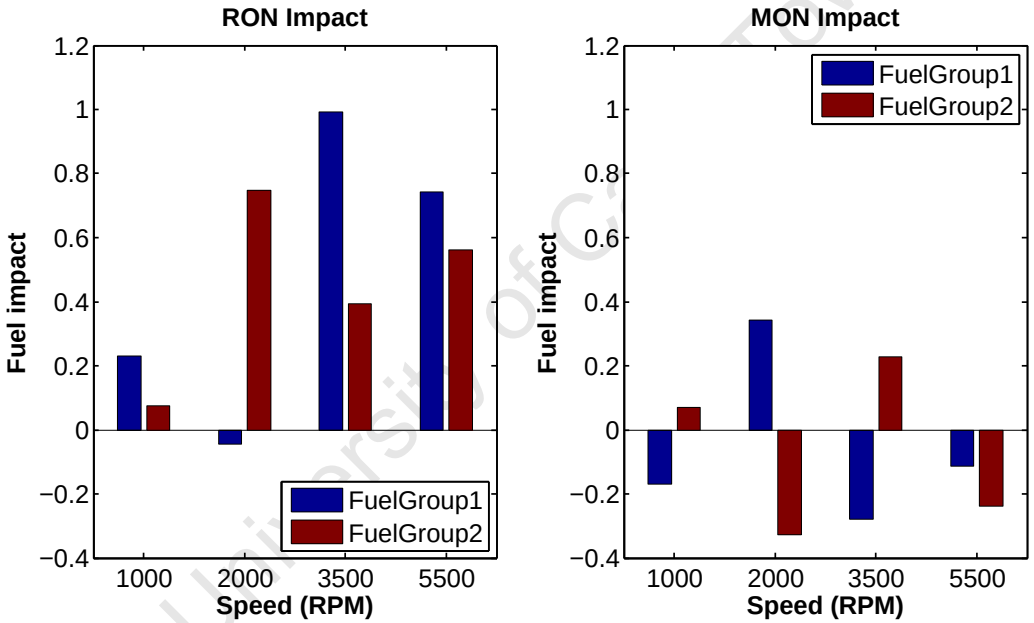

Figure 2.5: Separation of RON and MON impact (reproduced from [45])

The knock limit load mentioned is a measure of knock resistance, as it is the IMEP produced by the engine with KLSA timing. Thus the more knock resistant the fuel, the greater the spark advance that can be employed and the greater IMEP that can be achieved. This only stays valid up until MBT timing though.

The authors reported that for the separation of the RON-MON influence, RON has a significant impact on the knock limit load that is at a maximum at medium engine speed while MON has no clear impact.

As can be seen however from these results reproduced in Figure 2.5, the trends described by the authors are weak ones. For example, the 2000 RPM RON impact varies from approximately -0.1 to 0.8 bar for the two tests. The influence of RON and the lack of influence of MON on predicting knock resistance in modern engines does agree with findings of other authors [17, 30].

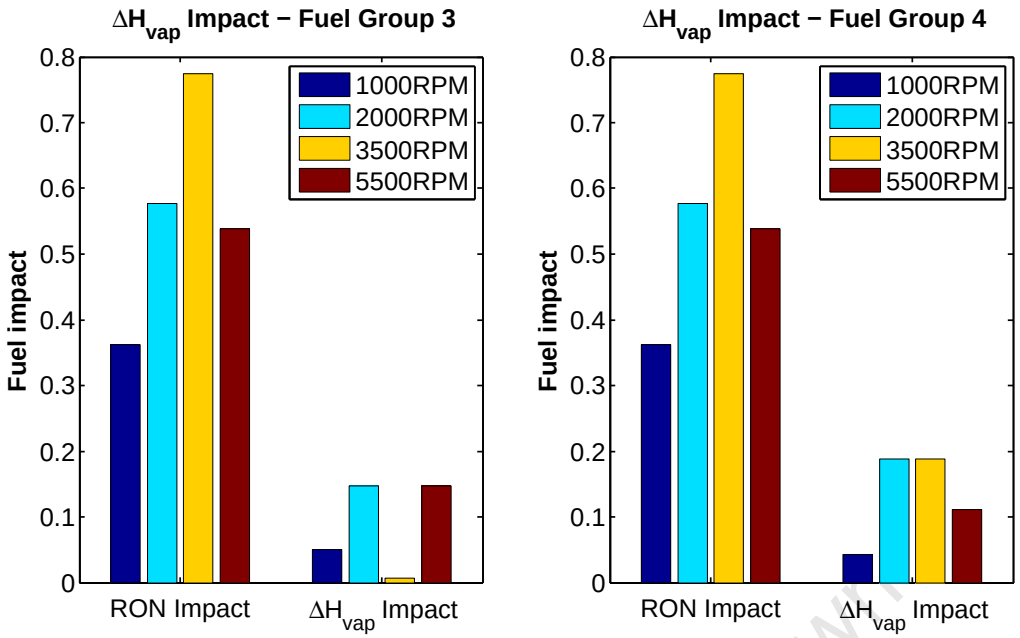

Figure 2.6: Separation of RON and heat of vapourisation (ΔH_{vap}) impact (reproduced from [45])

The separation of RON and heat of vapourisation, reproduced in Figure 2.6, was reported to show that heat of vapourisation effects are constant over the operating speeds, while RON's influence once again peaks at medium speeds. Once again we find the data is less than satisfactory. The heat of vapourisation influence shows a definite peak at medium speeds for the second group of results, while the heat of vapourisation influence disappears for 3500 RPM for the first set of tests and also has a peak at the medium speeds.

2.6 Modelling Knock in Engines

Modelling of knock in engines can be grouped as one of two methods, namely empirical correlations or mechanisms that simulate the chemical processes that occur during fuel oxidation.

These models must also allow for the correlation of the autoignition times seen in a constant pressure temperature environment (such as the experimental equipment used to measure autoignition times) to the changing pressure temperature environments of engines.

Livengood and Wu [46] proposed an empirical approach that is still widely used to provide this correlation. This formulation relied heavily on the assumptions that autoignition takes place when the concentration of a certain critical species reaches a threshold and the production of the critical species is dependant on the gas state while the threshold is not dependent on the gas state. These assumptions predict that autoignition will occur when Equation 2.3 is satisfied. A function relating autoignition

delay to the gas state is thus required for this integral approach.

$$\int_{t=0}^{t_i} \frac{1}{\tau(p,T)}\, dt = 1 \tag{2.3}$$

where $\tau(p,T)$: autoignition delay at the instantaneous pressure and and temperature the fuel is experiencing
t_i : time when autoignition occurs

This method was shown to work well for single stage autoignition prediction, despite the lack of validation of the assumptions. Livengood and Wu highlighted that two stage autoignition would not be well described by this approach and suggested a double integral method.

Douaud and Eyzat [47] developed a function to describe autoignition delay with respect to the critical gas properties. An Arrhenius function ($k = Ae^{\frac{-E}{RT}}$) was used to fit autoignition delays from knocking engine data. Equation 2.4 shows the equation with relevant coefficients produced for the PRF fuels.

$$\tau = 17.68 \frac{ON}{100}^{3.402} p^{-1.7} e^{\frac{3800}{T}} \tag{2.4}$$

where τ : autoignition delay
T : temperature
p : pressure
ON : Octane Number

In light of modern knowledge, this model was a crude one to describe autoignition delay of two-stage fuels. This equation produces a straight line on a Arrhenius plot (Figure 2.3), and so it is immediately apparent that this formulation is adequate over a limited range of pressure and temperatures at best, as it does not account for the NTC behaviour of two-stage fuels.

Yates et al. [37] developed a model using three Arrhenius equation, Equation 2.5, to overcome the shortfalls of the single Arrhenius approach. This approach produced good agreement for two-stage fuels over the NTC region. However it merely predicted the overall autoignition delay and could not predict any cool flame dynamics and their influence on the engine operation or be used for fitting to experimental data from autoignition measuring devices.

$$\tau_{overall} = \left\{(\tau_1 + \tau_2)^{-1} + (\tau_3)^{-1}\right\}^{-1} \tag{2.5}$$

where $\tau_{overall}$: overall auto ignition delay
τ_1 , τ_2 , τ_3 : Arrhenius equations

Yates and Viljoen [40] then developed a model to include the capability to predict cool flame timing and temperature rise. Three separate Arrhenius equations were

used and combined in Equation 2.6. It produced good agreement with experimental data. But while it allows for the prediction of the magnitude of the cool flame heat release, it does not predict the rate of this heat release, or that of the main peroxide heat release. Additionally, this model did not take into account inert diluents (such as Residual Exhaust Gas (REG)).

$$\tau_{overall} = \tau_1 + \tau_{h,CF}\left(1 - \frac{\tau_1}{\tau_{h,i}}\right) \tag{2.6}$$

where $\tau_{overall}$: overall autoignition delay
τ_1 : Arrhenuis function describing cool flame autoignition delay
$\tau_{h,i}$, $\tau_{h,CF}$: Arrhenius functions describing main heat release for the two temperature regimes before and after the cool flame respectively

Yates et al. [10] subsequently published a paper using the same model formulation as Yates and Viljoen [40], but with revised coefficients.

Figure 2.7 shows an Arrhenius plot of the implementation of the 1978 Douaud and Eyzat model [47], the 2005 Yates et al. model [37], the 2008 Yates and Viljoen model [40] and the 2010 Yates et al. model [10] for iso-Octane. These models are then compared to data from the results of a detailed kinetic modelling study also found in Yates et al. [37].

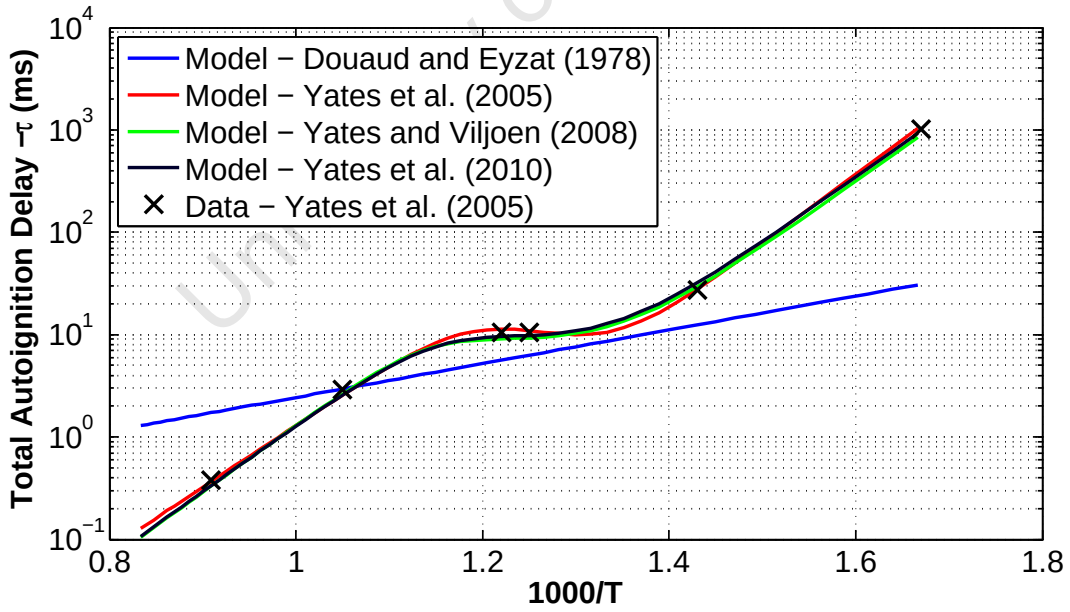

Figure 2.7: Comparison of empirical models reviewed, for iso-octane at 30 bar

Floweday [48] developed a functional global autoignition model that made use of representative reactions to simulate the detailed kinetics of fuel autoignition. The model bared closer resemblance to the actual processes involved in autoignition and so offered more insight to the underlying processes. This model predicted the heat

release rates and magnitudes of both the cool flame and main heat release reactions for two-stage fuels. It also offered the benefit of tracking species development during autoignition, which can thus be transported between computation cells and took into account inert component dilution. It however is more complex in implementation than the empirical models previously mentioned.

2.7 Modelling Fuel Delivery in Engines

2.7.1 Overview of Engine Evaporation Modelling Approaches

The evaporation of fuel in SI engines is complex, consisting of two-phase flow in a pulsating turbulent environment, with liquid fuel in both the droplet and wall film form. A number of phenomena are to be considered, such as spray modelling, droplet and wall film evaporation, wall wetting and wall film dynamics.

Modelling this rigorously is thus a computationally complex and expensive undertaking. Certain simplifying assumptions can be used however to simplify the problem while maintaining validity and usefulness of the model.

Only one dimensional engine manifold evaporation modelling was reviewed as it was considered sufficiently detailed for this study, with the results of Moran [43] highlighting this.

The modelling is concerned with the detailing of the mass, heat and momentum transfer that occurs during the evaporation and flow processes involved in the fuel delivery and preparation of an AF charge.

2.7.2 Overview of Evaporation Phenomena

Evaporation occurs when molecules at a liquid's surface gain enough energy, through the random interaction with their neighbours, to escape the intermolecular forces of the liquid. This process is illustrated in Figure 2.8. Thus, while the liquid's overall temperature may be well below the saturation temperature and thus not be changing phase as a whole, phase change is still able to take place. These molecules result in the overall average particle kinetic energy of the liquid dropping, as they have higher than average particle kinetic energy when they escape to vapour. As such, the overall temperature and energy content of the liquid decreases [49].

The layer of vapour molecules at the surface of the liquid can be considered to be at the saturation pressure of the liquid for that particular temperature. Evaporation occurs when this pressure at the droplet surface is greater than the pressure of the vapour in the surrounding gas (i.e. the partial pressure of the vapour in the gas mixture). This difference in pressure (or concentration, as concentration and pressure are analogous) is the driving force of evaporation. [49]

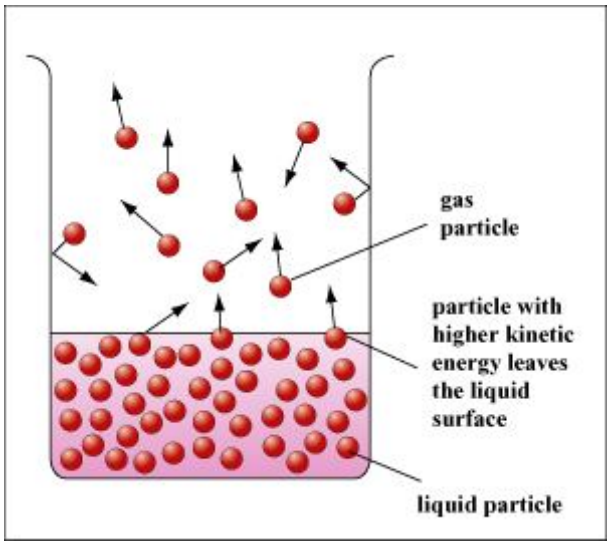

Figure 2.8: Schematic of the evaporation process (reproduced from [50])

2.7.3 Droplet Evaporation

The evaporation of a droplet in a gas stream is a complex process. Even with the assumption of axisymmetric flow and a spherical droplet, internal vortices result due to the flow, as seen in Figure 2.9. Modelling of the evaporation of these droplets in one-dimensional flow thus relies on a number of simplifying assumptions.

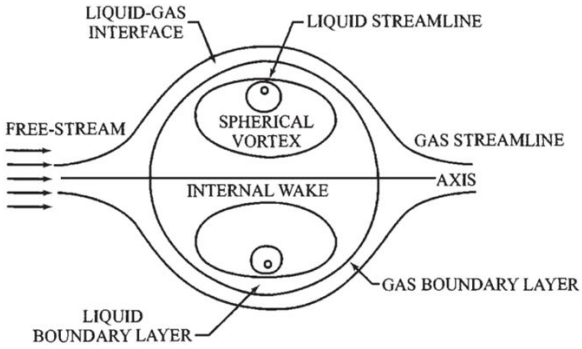

Figure 2.9: Droplet vapourisation in axisymmetric flow (reproduced from [51])

Droplet Size

Droplet spray produced by fuel injection can be described by a monosize droplet distribution or a varying size distribution.

A mono size droplet spray assigns all droplets a uniform diameter, usually that of the Sauter Mean Diameter (SMD), as it characterises a number of important evaporation processes [52]. The SMD is the diameter of a droplet that has the same volume to surface ratio of an actual droplet distribution and is denoted d_{32} as it is determined

using the three dimensional volume and the two dimensional surface area of the droplet.

Brown and Ladommatos [53], who were concerned with low load and low speed simulation of the mixture process in a port fuelled SI engine, argued for the acceptability of using a monosize droplet spray at low speeds as they found the fuel air mixture is controlled by fuel film evaporation as droplet evaporation during flight is low.

A distribution function can also be used to describe the droplet sizings produced by an injector [54, 55]. The Rosin-Rammler distribution (Equation 2.7) [56] is often used to describe the droplet size distribution for atomization process [52], with the two parameters, X and q, governing the distribution. Figure 2.10 shows an example plot of this distribution.

$$Y = e^{-\left(\frac{d}{X}\right)^q} \tag{2.7}$$

where Y : fraction of volume contained in droplets of diameter greater than d
d : droplet diameter
X : fitting coefficient
q : fitting coefficient

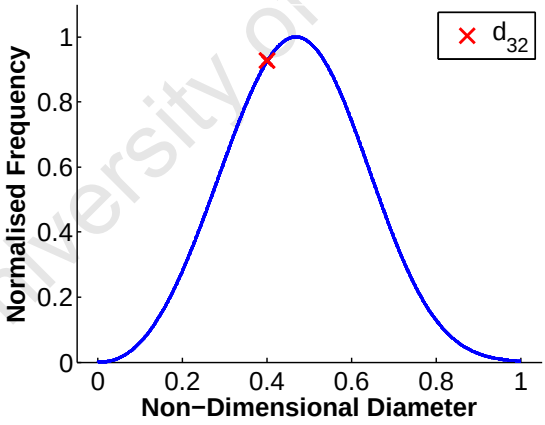

Figure 2.10: Rosin-Rammler distribution with Sauter mean diameter (d_{32}) plotted

The value of the droplet sizing can be either described by a user input based on measurements taken of the droplet sizing produced by the injector (such as Moran [43]) or can be predicted by modelling methods such as empirical correlations [51, 54].

Zero Dimensional Models

The assumption of either complete or zero vapourisation of the droplets by the air stream is the simplest approach to modelling evaporation.

For port fuel and carburettor engines, significant wall wetting takes place [8], and thus some assume that the fuel gets all its vapourisation energy from the walls. For DI, some assume that all the vapourisation energy is drawn from the air, and thus assume no wall wetting.

However, these assumptions are crude, and particularly invalid when fuels with high heats of vapourisation are used. For example, Marriot et al. [24] showed that the modelling of DI engines running on fuels with high heats of vapourisation without compensation for wall wetting will lead to errors, with over predictions of engine volumetric efficiency.

Curtis et al. [55] used the droplet size distribution to account for the vapourisation process. Those droplets below a threshold (10 μm) are assumed to vaporise. The droplet size distribution is determined by characterisation of the injector. No basis for this threshold is given by Curtis et al.. However, this threshold of 10 μm is mentioned by Heywood [8], who refers to empirical observations made by Trayser et al. [57]. The validity of this threshold for modern injectors and manifolds is unknown, and is thus another crude approximation that also offers little value in terms of understanding of the process.

Mass Transfer Modelling

Droplet evaporation can be modelled using the Film Theory of mass transfer. This assumes that evaporation can be represented by the mass transfer of a substance from a high concentration body to a low concentration body taking place over a very thin film of constant thickness [58, 59]. By doing this, the entire resistance to the mass transfer occurs over this film layer and can be described in terms of a diffusive mass transfer process. This approach results in Equation 2.8 governing the mass transfer from the droplet, which is the most commonly applied evaporation mass transfer description used for modern spray calculations [60].

$$\dot{m} = \pi d \rho_m D_{AB} Sh \ln(1 + B_M) \tag{2.8}$$

where m : rate of mass transfer
ρ_m : density of the mixture at the droplet surface
D : mass diffusivity
d : droplet diameter
B_M : Spalding mass transfer number

B_M is known as the Spalding Mass Transfer Number and represents the concentration gradient across the film that drives the process. It is given by:

$$B_M = \frac{\omega_{fs} - \omega_{f\infty}}{1 - \omega_{fs}} \tag{2.9}$$

where ω_{fs} : mass fraction of fuel vapour at droplet surface
$\omega_{f\infty}$: mass fraction of fuel vapour in free stream

The density of the mixture at the droplet surface is given by [53]:

$$\rho_m \approx \frac{p_\infty}{R_f T_d} \tag{2.10}$$

where p_∞ : pressure of the free stream
R_f : fuel gas constant
T_d : droplet temperature

Of the assumptions made in the derivation of this, the following should be highlighted [61]:

- Droplet is spherical
- Gas flow is constant across the droplet
- Film surrounding droplet is stagnant, of constant thickness and only has concentration change in direction perpendicular to the surface
- (Quasi) steady state in the gas

The Sherwood number is a dimensionless number that represents the ratio of convective mass transfer to diffusive mass transfer, and thus accounts for the effect that the relative velocity between the fluid and the gas has on evaporation. The Sherwood number is calculated using the Ranz-Marshall correlation [62], Equation 2.11.

$$Sh = 2 + 0.6 Re^{0.5} Sc^{0.33} \tag{2.11}$$

where Re : Reynold number
Sc : Schmidt number

This method has been used for numerous one dimensional droplet vapourisation models [54, 63–65].

Heat Transfer Modelling

The range of models available to account for droplet heating can be grouped as follows (taken from Sirignano [51]) in order of ascending complexity:

- The droplet temperature is uniform throughout and does not change with time;
- Infinite thermal conductivity models - The droplet temperature is uniform throughout, but changing with time

- Finite conductivity models - The droplet temperature varies with radius and with time, but re-circulation within the droplet is not taken into account
- Effective conductivity models - The droplet temperature varies with radius and time, and re-circulation is accounted for through correction factors
- Vortex models - The droplet description takes into account re-circulation through vortex models
- Full Navier-Stokes solutions

Only models from the first two groups were reviewed, as the complexity of the other groups was deemed unnecessary and prohibitive.

The constant droplet temperature approach ignores heat transfer, with the droplet temperature set to the wet bulb temperature. This results in the so called D^2 law [66], seen in Equation 2.12.

$$d^2 = {d_0}^2 - kt \tag{2.12}$$

where d : droplet diameter at time t
d_0 : initial droplet diameter
t : time
k : evaporation constant

The importance of droplet heating has been identified since the development of the D^2 law [60], and as such the various droplet heating models were introduced.

The infinite conductivity model assumes a uniform temperature across the droplet that varies with time. Using an energy balance across the droplet, Equation 2.13 is derived. The term on the left describes the heat transfer into the droplet, while the first term on the right describes the total heat transfer into the droplet due to the temperature difference, while the second term on the right describes the heat used to vaporise the liquid.

$$m_d c_{p,l} \frac{dT_d}{dt} = A h_{h,d}(T_\infty - T_d) - \dot{m_{d-g}} L \tag{2.13}$$

where m_d : droplet mass
$c_{p,l}$: specific heat of the droplet Liquid
A : droplet area
$h_{h,d}$: heat transfer coefficient of the droplet
T_∞ : free stream temperature
T_d : droplet temperature
$\dot{m_{d-g}}$: droplet mass transfer from droplet to gas
L : latent heat of vapourisation of the fuel

The Nussel number is a dimensionless number that represents the ratio of convective to conductive heat transfer (and is thus analogous to the Sherwood number) and is defined as:

$$Nu = \frac{hD}{k_g} \tag{2.14}$$

where h : convective heat transfer coefficient
D : characteristic length, namely the droplet diameter
k_g : thermal conductivity

Equation 2.13 can be rewritten in the form of Equation 2.15, using the Nussel number and the surface area of a sphere.

$$m_d c_{p,l} \frac{dT_p}{dt} = \pi D_p Nu k_m (T_\infty - T_P) - \dot{m_{d-g}} L \tag{2.15}$$

Corrections can be made to the energy balance, as suggested by Abramzon and Sirignano [67], to take into account the effects of Stefan flow. Stefan flow is flow induced due to the addition of a species at an interface. In evaporation's case, it is cased by the production of vapour at the droplet surface. This species production generates a mean flow. Diffusion also acts on this system due the concentration gradient present; thus the flow is faster with both Stefan flow and diffusion than that for pure diffusion. Stefan flow also distorts the thermal and diffusional films over which evaporation is assumed to take place, which requires correction to the previous model.

Abramzon and Sirignano's [67] resulting modification of Equation 2.13 to account for Stefan flow produces Equation 2.16:

$$m_d c_{p,l} \frac{dT_p}{dt} = \dot{m_{d-g}} \frac{c_{p,v}}{B_T} (T_\infty - T_P) - \dot{m_{d-g}} L \tag{2.16}$$

where $c_{p,v}$: specific heat of the fuel vapour

2.7.4 Wall Film Evaporation

Zero Dimensional Models

Any fuel that reaches the wall is assumed by Marriot et al. [24] to vaporise immediately, with all the vapourisation energy coming from the wall.

This assumption has been shown to produce realistic results for fuels with low heats of vapourisation by Brown and Ladommatos [53] in a one-dimensional modelling study of n-heptane in a PFI engine. They showed that wall film vapourisation is dominated by

the wall heating of the wall film, and thus the gas-wall film interactions can be ignored for these cases.

The validity of this approach to fuels with high heats of vapourisation is uncertain. The previous study suggests that the gas heating of the film would still be outweighed by the wall heating of the film. However, with the longer residence times that the fuel would have compared to a fuel with a lower heat of vapourisation, this may increase the cooling that the gas experiences. Secondly, the influence of this larger cooling on the wall itself is unknown.

Heat and Mass Transfer Modelling

Wall film evaporation is often dealt with in the same manner as droplet vapourisation [54, 55, 63] using the mass transfer given by Equation 2.8, but with the fuel film area and thickness replacing those of the droplets.

The energy balance for the film heat transfer is shown in Equation 2.17. The term on the left describes the overall energy content of the fuel film. The first term on the right describes the heat transfer from the gas to the film; the second term describes the heat transfer from the wall to the film; while the third term describes the heat used to vaporise the fuel [54].

$$\rho_f c_{p,f} \delta \frac{dT_f}{dt} = h_{h,g-f} A (T_\infty - T_{f,s}) + h_{h,w-f} (T_w - T_{fs}) - \dot{m_{f-g}} L \tag{2.17}$$

where
ρ_f : density of the film fluid
$c_{p,f}$: specific heat of the film liquid
δ : film thickness
$h_{h,g-f}$: heat transfer coefficient for the gas to film heat transfer
$T_{f,s}$: film Temperature at the surface
$h_{h,w-f}$: heat transfer coefficient for the wall to film heat transfer
T_w : wall temperature
$\dot{m_{f-g}}$: film mass transfer from film to gas

The heat transfer coefficients for the forced convection from the gas to the film are given by Equation 2.18 [62].

$$h_{h,g-f} = \frac{k_g}{d_m} 0.023 Re^{0.8} {Pr_g}^{0.4} \tag{2.18}$$

where
k_g : thermal conductivity of the gas
Re : Reynolds number of the mixture
Pr_g : Prandtl number of the gas

The heat transfer from the wall to the film is often assumed to be through conduction [53, 54]; thus the heat transfer coefficient is given simply by Equation 2.19.

$$h_{h,w-f} = \frac{k_f}{\delta} \tag{2.19}$$

where k_f : thermal conductivity of the film

Curits et al. [55] and Chen et al. [54] use the Woschni heat transfer coefficient [68] for the in-cylinder fuel film heat transfer coefficient.

Wall temperatures above the fuel's boiling temperature require separate treatment as described by Brown and Ladommatos [53]

The temperature profile across the wall film is assumed to be linear by many authors [53, 54], while some consider a constant temperature across the film. Modelling by Brown and Ladommatos [53] predicted a maximum temperature difference of 4℃ across the wall film, suggesting a constant temperature assumption is sufficient.

It should be noted that no evaporation models were found that considered the effect of the heat removal from the manifold and cylinder walls. This may not be valid for fuels with high heats of vapourisation. These fuels may draw enough energy from the walls and cylinder so that they operate at a lower temperature.

Wall Film Surface Area

Wall film evaporation is dependent on its surface area, and as one-dimensional modelling does not allow for a direct calculation of this, a number of strategies are employed to obtain a value for the wall film surface area.

Brown and Ladommatos [53] visually inspected the wall wetting and used this approximate value. A constant film thickness is assumed and is calculated by determining the film volume present at any one time.

Chen et al. [54] use a number of assumptions for different wall films. For example, wall films on valves are assumed to cover the entire rear face and cylinder wall films are assumed to cover half the instantaneous area at most. No basis for these assumptions are given,

Boam and Finlay [69] and Moran [43] assumed the film was evenly distributed around the wall. Moran however found this assumption incorrect that led to an over prediction of the film heating rate. After visual inspection of the wall film formation, the model was adjusted to have separate sections with different wall film profiles. This was shown to produce more accurate results as the wall film surface area was seen to change dramatically for different engine speeds.

Curtis et al. [55] used a constant to relate the film height to surface area. This aspect ratio constant can be altered for different engines and thus allows for tuning of the model.

There is thus no definitive approach to this problem faced by 1D models, with visual inspection when possible appearing to be the best approximation of this value.

2.7.5 Droplet Dynamics

Droplet Motion

The simplest approach is to assume that the droplets enter the duct with the same velocity as the gas, which Locatelli et al. [63] assumed. This approach thus ignores the effects on evaporation of the relative velocity between the droplet and the gas, as well as the diminishing influence of this effect as the droplets velocity approaches that of the main gas flow through drag interaction.

Full one-dimensional treatment of droplet dynamics assumes that the droplets are travelling along the centreline of the duct with the droplet motion governed by the momentum interaction between the droplet and the gas flow. The droplet velocity is calculated using Equation 2.20 , derived from a momentum balance on the droplet.

$$m_d \rho_d \frac{du_d}{dx} = \tau_{g-f} dA_{d,p} \tag{2.20}$$

where u_d : velocity of the droplet
τ_{g-d} : shear force applied by the gas to the droplet
$A_{d,c}$: cross sectional area of the droplet, $\frac{\pi d^2}{4}$

The shear force applied to the droplet is given by Equation 2.21.

$$\tau_d = \frac{1}{2} C_D \rho_g \left(u_g - u_d\right) \left|u_g - u_d\right| \tag{2.21}$$

where C_D : drag coefficient
u_g : velocity of the gas

Equation 2.22 from Choi and Lee [70] is argued by Chen et al. [54] to give better results than some of its compatriots as it gives a lower drag force, which compensates for the under-prediction of the gas velocity that one-dimensional modelling produces.

$$C_D = 2.3 Re^{-0.37} \tag{2.22}$$

Droplet Impingement

Wall wetting through droplet impingement needs to be taken into account artificially when conducting one-dimensional modelling of fuel flow, as the three-dimensional nature of the wall wetting phenomenon prevents direct calculation in one-dimensional modelling.

Authors have thus taken a number of approaches to account for wall wetting. They commonly determine the interaction between the spray and the manifold or cylinder wall either through observation or calculations based on geometric considerations.

Curtis et al. [55], as mentioned in Chapter 2.7.3, used droplet size as an evaporation criteria. Thus droplets above the 10μm threshold were distributed between fuel puddles based on observation.

Marriot [24] and Chen et al. [54] both determined the droplet impingement from the geometric interference of the spray plume and wall.

Chen et al. [54] make use of a method applied to their discrete particle approach, where the position of droplets is tracked along the distance of the manifold. They determine the fraction of droplets that must be removed from the gas stream at any point and added to an impingement site based on a calculated impingement probability. This probability is calculated depending on the geometry of the manifold and the spray plume at that impingement site. For example, the probability of impingement caused by the spray plume interfering with the wall is proportional to the spray plume cross sectional area and the manifold cross sectional area at a point, as seen in Equation 2.23.

$$Pr_{imp} = \frac{A_{nom} sin\theta_1}{A_{nom} sin\theta_1 + A_{duct} cos\theta_1} \tag{2.23}$$

where Pr_{imp} : probability of impingement
A_{nom} : nominal area covered by the spray
A_{duct} : area of the manifold duct
θ_1 : incidence angle relative to normal to the wall

Moran [43] made use of a droplet deposition function developed by Friedlander and Johnstone [71] for solid particle deposition rates from turbulent gas streams. This predicts the mass transfer of droplets from the free stream to the wall as a result of turbulent flow. Moran [43] notes that this is a traditional approach adopted previously by other authors.

The calculation of wall wetting in 1D modelling is thus still largely dependent on user observation. The accuracy of these assumptions will be dependent on the complexity of the fuel and air flow the engine produces.

2.7.6 Wall Film Dynamics and Re-entrainment

Wall film dynamics are ignored by some researchers, with the wall film assumed to be a stagnant layer [53]. This thus ignores the transport of fuel into the cylinder through wall film flow.

When accounting for wall film motion the influence of the gas flow dragging the film forwards must be taken into account, as well as the friction between the wall and the

film holding the film backwards. The equation governing the velocity of the fuel film determined from a momentum balance can be seen in Equation 2.24.

$$\rho_f m_f \frac{du_{fs}}{dt} = \tau_{g-f} - \tau_{w-f} \tag{2.24}$$

where u_{fs} : velocity of the film at the surface
τ_{g-f} : shear force of the gas acting on the film
τ_{w-f} : shear force of the wall acting on the film
m_f : mass of the wall film

The two respective shear forces are given by Equation 2.25 and Equation 2.26 [72].

$$\tau_{w-f} = 2\mu_f \frac{u_{fm}}{\delta} \tag{2.25}$$

where μ_f : dynamic viscosity of the film

$$\tau_{g-f} = \frac{1}{2} f \rho_g \left(u_g - u_{fs}\right) \left|u_g - u_{fs}\right| \tag{2.26}$$

where f : Fanning friction coefficient

The fanning friction factor is given by Equations 2.27, 2.28 and 2.29.

$$f = \frac{16}{Re} \qquad \text{when} \qquad Re < 3000 \tag{2.27}$$

$$f = 0.0053333 + 7.0364 \times 10^{-7}(Re - 3000) \qquad \text{when} \qquad 3000 < Re < 4000 \tag{2.28}$$

$$f = \frac{0.0791}{Re^{0.25}} \qquad \text{when} \qquad Re > 4000 \tag{2.29}$$

The entraining of liquid film into the air stream through the stripping of the film off sharp edges and valve seat squeezing can be accounted for through various empirical relations [54, 55]. This was not reviewed however, as it was deemed unnecessary for this work.

2.7.7 Gas Flow Interaction with Fuel Evaporation

Modelling of the gas flow in the manifold and the interaction with the evaporating fuel can once again be dealt with varying levels of comprehensiveness within the constraints of one-dimensional modelling.

Locatelli et al. [63] adopted the simplest possible approach, that of assumed constant air flow throughout the engine cycle with a constant air temperature.

Brown and Ladommatos [53] made use of Lagrangian approach to the droplet spray and a control volume approach to the fuel film flow, but assumed constant pre-calculated properties for the gas flow. These properties were determined from a vessel filling type gas flow model. They argue that the acceptability of constant air temperature as the heat loss of the droplets to the air is small and wall evaporation dominates the fuel evaporation process.

Fuel's with high heats of vapourisation, unlike n-heptane which was used in their study, would result in a larger temperature drop, as well as the possibility of saturation occurring, which renders this assumption less acceptable. This assumption would be even worse for DI application, as they achieve greater charge cooling than PFI applications.

Brown and Ladommatos [53] note that the application of the many empirical heat and mass transfer correlations to an unsteady flow will lead to under prediction of heat and mass transfer rates, as the rapidly changing flow in the manifold will prevent the formation of a boundary layer.

A steady state approach applies conservation of energy, mass and momentum to the gas stream, fuel film and fuel droplets across differential control volumes, but assumes no change in properties with respect to time, thus assuming a process that is steady in nature. This of course is not the case in the inlet manifold of an engine, which has pulsating flow, but it greatly simplifies the model and can still provide valid and useful data. This approach was used in works such as Moran [44], Milton and Behnia [65] and Boam and Finlay [69].

The most comprehensive one-dimensional approach is a full unsteady state gas dynamics model, which is then coupled with a fuel evaporation model. Typically, the gas flow is calculated with a Eulerian frame of reference, where the calculations are based on fixed control volumes and the changes in properties across them. The fuel droplets are typically dealt with in a Lagrangian approach, where packets of droplets are tracked as they travel through these various control volumes. The interaction between the droplets and the gas flow is achieved through a source term in the gas dynamics model. This approach was used by Chen et al. [54].

2.7.8 Validation of models

Tip-In-Tip-Out validation was used by a number of authors [54, 55, 63]. This involves rapidly ramping the throttle position from open to closed to open (or vice versa) and then measuring the AF ratio change. This change is brought about by the change in

evaporation of the fuel film due to the change in air-flow rate. This method tests the model's transient response and the fuel film evaporation behaviour.

Validation through the measurement of a number of flow properties such as pressure, gas and droplet temperature was used by Moran [43]. While able to validate the model, this method is restricted by the difficulty of obtaining accurate temperature measurements in the complex two-phase flow.

Chapter 3

Experimental Investigation

An experimental investigation was conducted to provide calibration data for the modelling study. This chapter details the test methodology employed in the investigation, followed by an overview of the experimental apparatus used. Various difficulties that influenced the final experimental matrix are then detailed.

3.1 Test Methodology

The experimental work, as detailed in the introduction, had the goal of providing data to tune and validate the mathematical model. The work was also aimed at providing some insight itself into the influence of charge cooling and autoignition chemistry.

The experimental investigation was designed to physically separate the charge cooling influence and autoignition chemistry influence. This was to provide experimental data that, while validating and being used to tune the mathematical model, would also provide experimental indication of the separate influences of the two factors under investigation.

Additionally, the experimental investigation was designed to operate in the Beyond RON operating regime.

3.1.1 Separation of Charge Cooling Impact

The separation of the charge cooling from the chemical influence of the fuels was achieved by artificially varying the fuels' charge cooling through pre-evaporation and comparing the fuels' knock performances.

To achieve this as well as allow for the recording of data concerning the evaporation of the fuel, a manifold was designed that allowed for the heating of the inlet air with a number of set-up options to allow for changes in the amount of charge cooling achievable (the inlet manifold set-up is dealt with in Chapter 3.2.2).

There were three manifold options that fuels were subjected to, namely a traditional PFI case, a maximum evaporation case ("MAX") and a pre-evaporation case ("PRE").

PFI Case

The PFI case had the injector set-up in a standard PFI position, with the injected fuel aimed toward the back of the inlet valve. This allowed some cooling of the inlet charge by fuel evaporation, with the rest of the vapourisation energy coming from the manifold walls. This gives an indication of the output of the engine in a conventional PFI mode, with the effects of chemistry and charge cooling both influencing the antiknock index of the fuel.

The inlet air temperature was controlled to 50℃ just before the position of the port-fuel injector at the end of the manifold. This inlet air temperature of 50℃ was chosen as it represented a typical post-intercooler temperature that had been seen previously by the research group as well as values given in a number of informal sources [73, 74].

MAX Case

The maximum evaporation case (MAX) injected the fuel far upstream of the inlet port to allow for as much evaporation as possible, allowing for the greatest influence of the charge cooling on engine performance to be seen.

The inlet air was controlled to 50℃ at the beginning of the manifold just before this upstream injection point for fair comparison with the other inlet manifold cases. This set up also allowed for the validation of the evaporation model, as measurements of the temperature progression as the fuel evaporates could be taken along the manifold.

PRE Case

The fully pre-evaporated case (PRE) had the fuel injected far upstream of the inlet valve (at the same location as the maximum evaporation case), with the inlet air heated to an extent to allow each fuel to be fully evaporated once it reached the inlet valve. The full pre-evaporation case, when compared to the other two cases, gives an indication of the performance of the fuel without its charge cooling ability.

The AF mix was thus controlled to 50℃ at the end of the manifold at the same point that the PFI case was controlled to, allowing for the fuel to be fully evaporated by that time.

3.1.2 Separation of Autoignition Chemistry Influence

The separation of the influence of autoignition chemistry on knock resistance was achieved through the use of different fuels with varying autoignition profiles.

Ethanol and iso-octane were chosen as the two fuels to conduct the full study with, while a 95 RON Unleaded Petrol (ULP 95) was included to be used in the experimental section of the study to allow for a K-analysis.

Ethanol would represent the alcohol fuels, and with its high RON, high sensitivity and high heat of vapourisation it would contrast well with a more traditional fuel.

iso-Octane was chosen as it represents a more traditional two-stage fuel such as petrols. This single component fuel was used instead of a blend to represent traditional petrols to ease modelling and prevent unnecessary complexity, as the crucial aspects under investigation, namely differences in autoignition and charge cooling, would be represented well by iso-octane.

A full boiling range petrol, in this case a ULP 95, was included. This would provide both a benchmark to compare the other fuels against as well as allow for a K analysis, as this analysis requires that the sensitivity and RON of the fuels not be correlated (see Figure 3.1 illustrating the lack of correlation) [16]. The petrol would not be modelled due to its complexity.

Table 3.1 highlights the properties of the fuels chosen.

Table 3.1: Fuel matrix

Fuel	Fuel Type	Autoignition classification	RON	MON	Sensitivity
iso-octane	paraffin	two-stage	100	100	0
ethanol	alcohol oxygenate	single-stage	108.6	89.7	18.9
ULP 95	fuel blend	two-stage	95	85	10

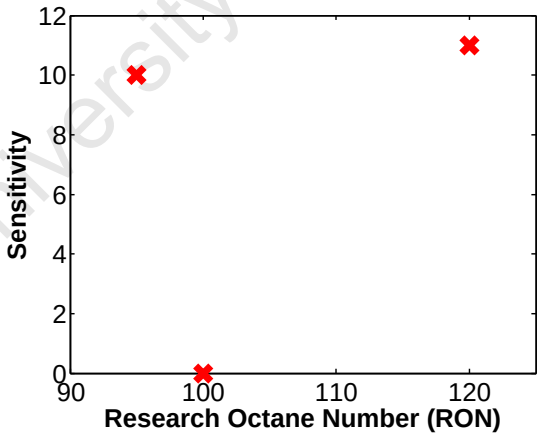

Figure 3.1: Fuel selection : sensitivity versus RON

3.1.3 Comparison of Knock Resistance

A suitable method was required to give an indication of the differing knock resistances of the fuels used under the various engine conditions.

One approach would be to keep the operating conditions the same for all fuels and compare the Knock Amplitude (KA) produced by each fuel. Knock however damages engines and so keeping the knock below a safe limit is desirable.

Another option is to use a similar method to that of the octane tests, namely find a PRF blend that knocks at the same intensity as that of the fuel under investigation. This though is a time consuming approach.

The approach taken in this study was one often adopted in literature [16, 17], whereby a Knock Limit (KL) value was set and the spark timing was advanced until the KA reached the value of the KL. The spark timing once the KA reached the KL was thus the Knock Limited Spark Advance (KLSA). This KLSA thus provided a comparative measure of the knock resistance of the fuel.

3.1.4 Operational Conditions

The operational set points chosen under which the experimental equipment was run are shown in Table 3.2.

Table 3.2: Experimental set points

CR	8.86				
Speeds (RPM)	1200	2000		3000	4000
Manifold Conditions	PFI		PRE		MAX
Fuels	ethanol		iso-octane		ULP 95
Gauge Boost (Bar)	0.1	0.2	0.3	0.4	0.5
Equivalence Ratio	1				
Throttle Condition	WOT				

A range of speeds and boost levels were chosen to span a variety of operating conditions and so allow for the determination of their influence.

Wide Open Throttle (WOT) was chosen for all operating points as knock is most severe at under these conditions [8].

The sweep of boost pressures ensured that for the two fuels operation is knock limited at some point and gives an indication of pressure's influence.

An equivalence ratio of 1 was chosen as maximum knock occurs at AF ratios just rich of stoichiometric [8], and little value would thus be gained from the varying of the equivalence ratio away from this standard value.

The boosted conditions together with the cooling provided in the MAX and PFI case was considered to be sufficient to ensure that operation would be in the negative K regime.

Knock Limit

Borderline knock was required for this investigation, as this would affect the pressure history the least and thus facilitate fitting of the model to the pressure histories. This would also minimise damage to the engine in use, which was a particular concern due to the age of the engine.

The progression of the peak knock value against spark advance was thus plotted for a test run, as shown in Figure 3.2.

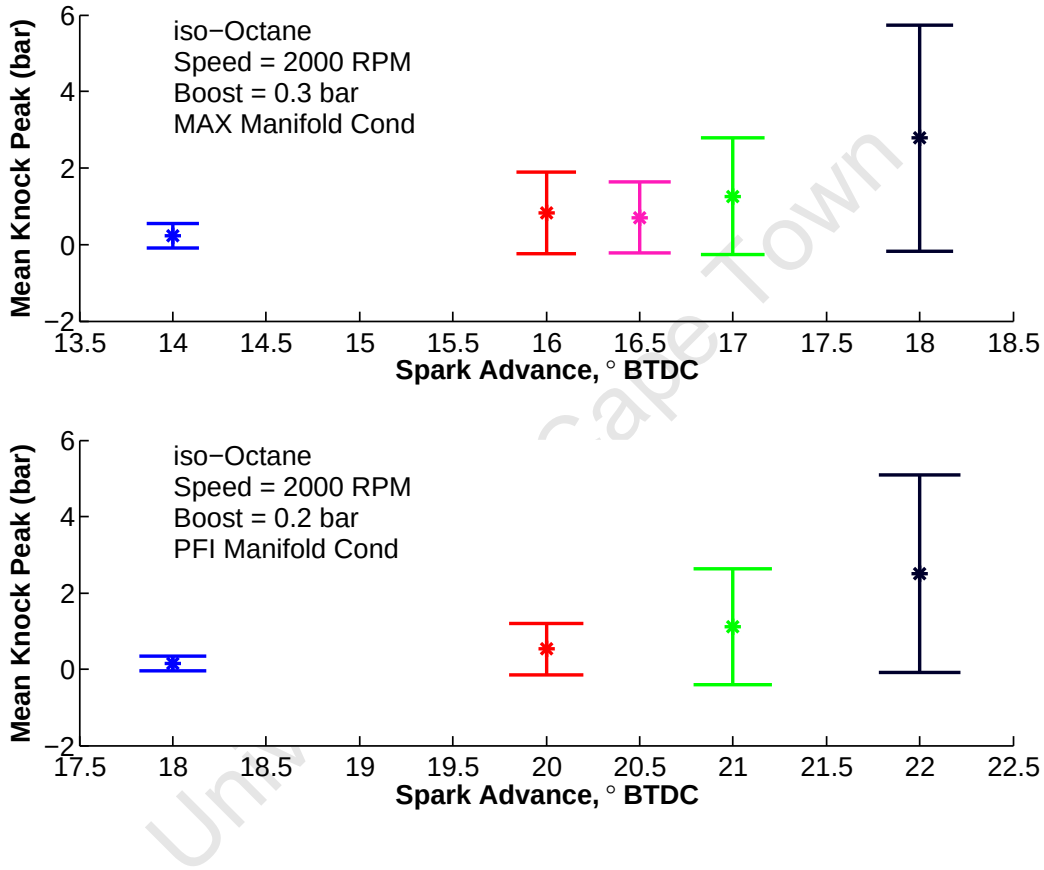

Figure 3.2: Mean knock peak, over 300 cycles, as spark timing is advanced

Figure 3.3 shows the scatter of the knock peaks over the 300 cycles as the timing is advanced, showing the number of cycles knocking over this 300 cycle span, as well as the variation in knock intensity. Figure 3.4 shows the variation of IMEP of the engine at the various spark advances, showing how the knock increases the scatter of measured engine properties.

With these plots and the literature reviewed of Chapter 2.1.5 in mind, a KL was chosen of the average peak pressure of the filtered trace, averaged over 300 cycles, of 1 bar. This was thought to be a fair compromise between ensuring knock occurs for a majority of the cycles while maintaining borderline knocking conditions. Additionally, as can be seen, the peak knock values follow a exponential rise and so a larger peak knock value would make both control difficult and engine damage increasingly likely.

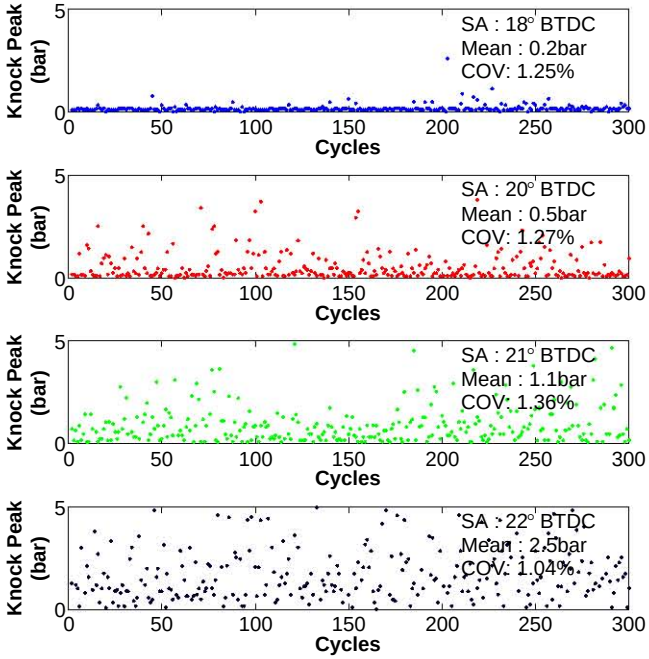

Figure 3.3: Knock peak scatter for 300 cycles as spark timing is advanced

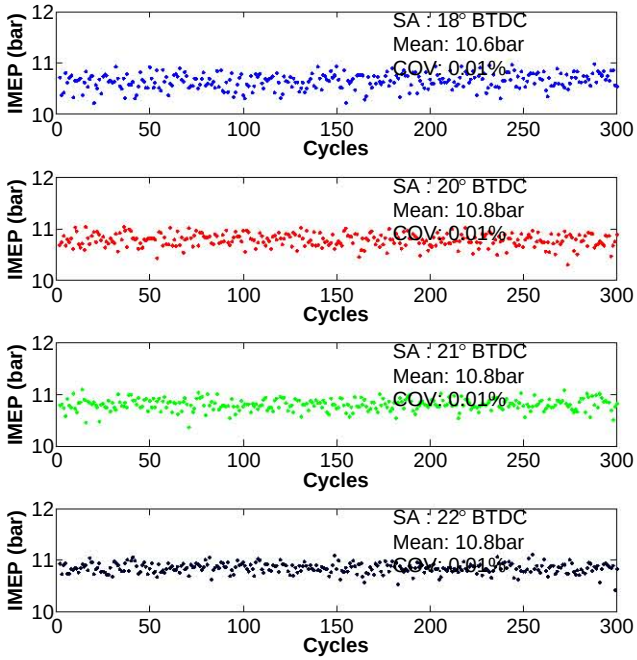

Figure 3.4: IMEP scatter for 300 cycles as spark timing is advanced

3.2 Experimental Set-Up

3.2.1 Engine

The experimental work was performed on a boosted 0.45 ℓ single-cylinder SI Ricardo Hydra engine, shown in Figure 3.5. Relevant details concerning this engine are listed in Table 3.3.

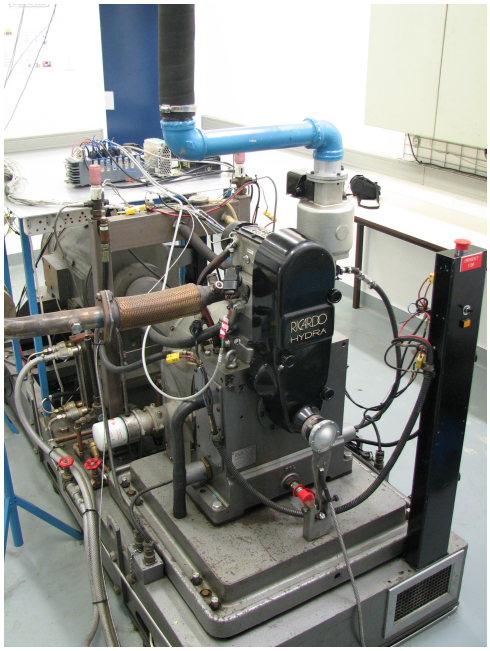

Figure 3.5: Ricardo Hydra test engine

Make	Ricardo Hydra
Compression Ratio	8.86
Bore	80.26mm
Stroke	88.90mm
Swept Volume	445cm^3
Conrod	152mm
IVO	-372 CAD
IVC	-124 CAD
EVO	124 CAD
EVC	372 CAD
Min Speed	1200 RPM
Max Speed	5400 RPM
Valves	2
Combustion Chamber	Bath Tub
Piston Top	Flat
Fueling	PFI

Table 3.3: Engine characteristics

3.2.2 Inlet Manifold and Air preparation

Overview

An experimental investigation into the influence of fuel evaporation on the inlet charge was achieved with an inlet manifold designed to allow for the varying and measuring of the inlet charge conditions.

The manifold was designed to allow for the following:

- Heating of the inlet charge to ensure full vapourisation of the test fuels under chosen operating conditions
- Two fuel injector positions: a standard PFI position and a position upstream of the inlet valve to allow for greater time for evaporation
- The insertion of various probes into the manifold for measurement purposes.
- Inner insulation of the manifold to reduce the heat transfer between the wall film and the piping.

The manifold was insulated through the insertion of a Teflon liner into the main length of piping. This insulation was provided to reduce heat transfer from the piping walls to the fuel wall film and inlet charge. Brown and Ladommatos [53] have shown that fuel evaporation can be dominated by the wall heating of the film, so this insulation was an attempt to minimise this effect along the length of the manifold to maximise heat transfer between the charge and the film. This would increase the charge cooling effect, which was the goal of the long manifold.

This liner was however only present upstream of the PFI injection point. Thus under PFI conditions the fuel was injected onto the normal heated inlet manifold walls and inlet valve.

Figures 3.6 shows the final inlet manifold and Figure 3.7 shows a cross section of the manifold, highlighting the various probes.

Appendix A gives further details concerning this design.

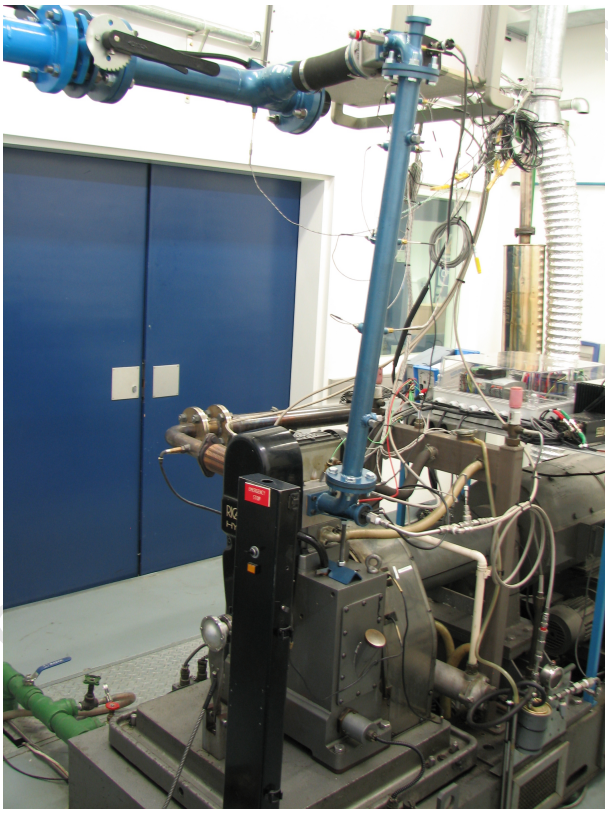

Figure 3.6: Inlet manifold with various probes

Influence on Breathing Dynamics

It was known from the outset that the inlet manifold designed would worsen the breathing dynamics of the engine. This would be caused by both the absence of a plenum volume to dampen inlet manifold oscillations as well as the lack of tuning of the manifold to achieve satisfactory breathing dynamics across the speed range.

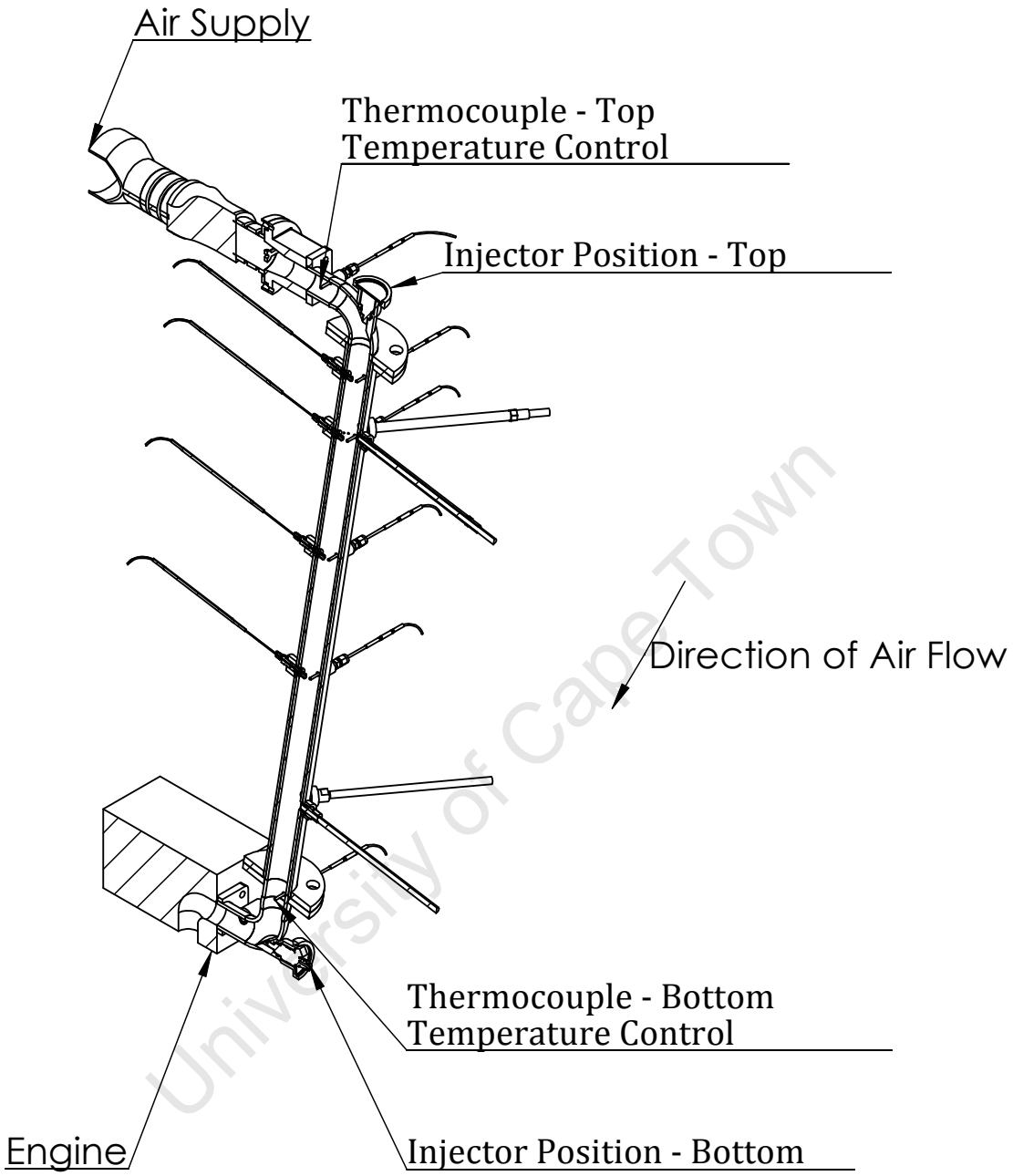

Figure 3.7: Cross-section of inlet manifold, showing position of temperature control points

The plenum volume was omitted as it would have to be placed between the two injection points to provide any realistic chance of dampening the inlet oscillations. This volume would then fall within the region of the inlet manifold being modelled, introducing further complexity to the problem.

The tuning of the manifold was not considered as it would fall outside the scope of this

project.

The use of the untuned manifold sans plenum in order to capture evaporation details at the expense of the breathing dynamics was considered an acceptable compromise, as the absolute engine performance was not of concern but rather the changes in performance between the two fuels.

Air Preparation and Boosting

The inlet air was boosted using a Roots blower. This boosted air was subsequently supplied to an air-to-air intercooler, a laminar flow meter and a buffer tank, from where it was piped past a heating element, a throttle plate and then into the inlet manifold. Figure 3.8 shows the system.

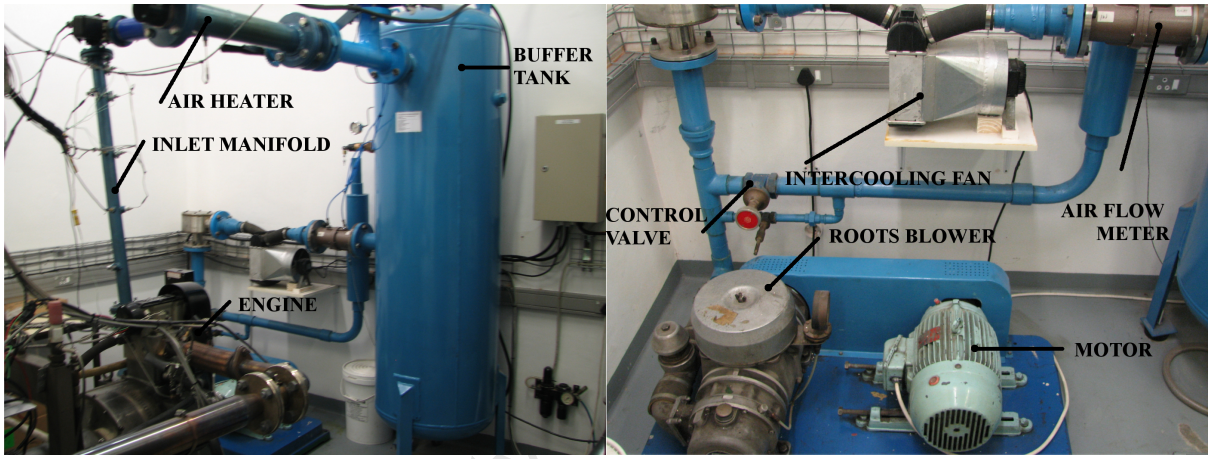

Figure 3.8: Hydra engine boosting system

The boost was set by running the Roots blower at rated capacity and venting a portion of the supplied air to get the level of boost required. The throttle plate was used only for start-up of the engine, while the intercooler fan was left off, as the inlet air was to be heated afterwards. The air heater consisted of a 3-phase 12kW element heater inside a section of the inlet air piping. The purpose of the buffer tank was to dampen the any oscillations from the Roots blower before it reaches the engine.

3.2.3 Engine Instrumentation and Data Acquisition

The engine control unit was a National Instruments CompactRIO Real-Time controller and Field-Programmable Gate Array (FPGA) chassis. This chassis housed a number of plug in modules that allowed for the control of various subsystems on the engine (eg. PFI, throttle). This set-up was communicated with and programmed from a PC running National Instruments Labview and Drivven software. This set-up is explained in further detail in [75].

The dynamometer control and the recording of various miscellaneous measurements was through ETA software (See [76] for more information).

Pressure Indicating

In-cylinder pressure measurement was made using a Kistler 6121 piezoelectric pressure transducer. It is not a water-cooled transducer but was housed in the cylinder head such that it passed through the cooling water jacket. Dynamic inlet manifold pressure measurements were made using a Kistler 4075 piezoresistive fast response transducer. This transducer was also not water-cooled. This data was relayed via the required signal processing equipment to an AVL Indiset data capture system and viewed in real-time on AVL Indicom 1.6 software [77].

The Indicom software also allowed for various real-time calculations, such as the heat release analysis and crucially that of the KL (described in Chapter 3.1.4), as well as various post processing, such as the pressure trace smoothing.

For all set-points, Indicom captured 300 pressure traces at a resolution of 0.1 CAD. This resolution was required for the meaningful identification of knock and the knock limit, as recommended by the Indicom 1.6 user documentation.

The calibration of the in-cylinder pressure transducer and inlet manifold were both checked on a dead-weight tester. Their original calibration values were found to be still satisfactory.

Other Data capture

The various other data sources (such as thermocouple readings, engine set speed, atmospheric pressure and other non-cylinder pressure readings) were recorded by Eta software at 1 second intervals for 30 seconds. This recording was manually activated after the Indicom in-cylinder pressure recording was activated, to ensure both systems recorded under the same conditions.

Temperature Measurement

The inlet manifold was designed to allow for the capturing of temperature measurements along the length of the inlet manifold to allow for validation of the evaporation model. However the capture of temperature data in a two phase flow is a difficult process.

Moran [43] details a number of these difficulties, with varying levels of success achieved, in the use of thermocouples to capture this data. In particular, the capture of droplet temperatures with bare thermocouples was considered reasonably successful while the gas temperatures captured with a covered thermocouple were considered poor.

Despite the difficulties associated with the use of thermocouples to capture temperature data, more advanced techniques were considered prohibitive considering the scope of the study. Additionally the data captured by the thermocouples together with the tested nature of the evaporation model that was used was felt sufficient to provide insight into the evaporation process.

The measurement was thus conducted with two sets of thermocouples placed inside the manifold. Bare thermocouples were placed to measure the droplet temperature. The thermocouples placed at the beginning and end of the manifold that were used for the controlling of the charge temperatures for the various manifold cases were also bare thermocouples.

Shielded thermocouples were placed as well, despite their proven lack of accuracy in measuring gas temperatures. However they do provide a measurement that is a combination of both gas and droplet temperatures, so if their readings approached those of the bare 'droplet' thermocouples along the length of the manifold, they would give an indication of complete evaporation having taken place. Figure 3.9 shows the two rows of thermocouples down the length of the manifold. Details concerning the thermocouples are found in Appendix A.

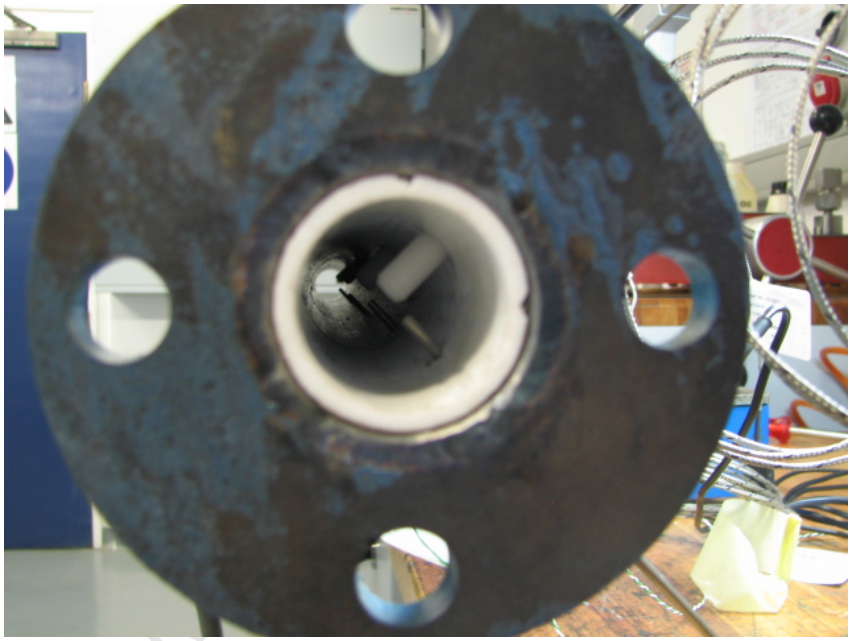

Figure 3.9: Shielded and bare thermocouples down the length of the manifold

Measurement of the wall film with the use of thermocouples is difficult. Moran [43, 44] measured the temperature of the wall film using a recessed thermocouple so that the wall film would gather in the recess. Wall films have however been shown to have thicknesses in the order of 50 to 100 μm. . Brown and Ladommatos [53] showed that after a initial heat up period, we can expect the wall film to heat up to the manifold surface temperature. Thus two recessed wire thermocouples were placed in the inner Teflon liner of the manifold to provide a wall temperature that would be used in the manifold model. Thus no direct wall film temperature measurements were made.

The thermocouple measuring system, into which the thermocouples were plugged, was calibrated using a Fluke Digital multimeter to supply the required fixed charge.

Combustion Data Processing

A number of algorithms were required to post process the data captured by the Indicom software. A description of these processing algorithms can be found in Appendix B.

3.3 Experimental Investigation Difficulties

A number of experimental difficulties were encountered during the investigation. These difficulties limited the final number of experimental set points that were satisfactory.

A brief summary of the most critical issues follow here, with a more detailed description of all the issues to be found in Appendix C.

Noise Influence on Knock Limit Detection

The knock intensity seen while operating at certain set points, chiefly 4000 RPM, was noted to not progress in the exponential manner as seen on other runs.

This was determined to be noise influence on the signal. While under certain set points this was corrected for by advancing the spark timing beyond the KL and using the progression of the knock intensity as a measure of when true knock was occurring, certain signals did not allow for this as the noise influence was too great. The data from these set points was consequently ignored.

Wetting of Manifold Temperature Control Thermocouple

It was found that the bare thermocouple at the top of the manifold suffered from fuel wetting at high engine speeds, despite being approximately 100 mm upstream of the fuel injection point. This thermocouple was used to control the inlet air temperature for the MAX case and as such high speed MAX runs suffered from incorrect inlet air temperature control.

This phenomenon was detected during experimentation and subsequently corrected for through the use of a thermocouple even further upstream of the fuel injection point to control the air temperature to. However, as the dyno failure halted testing prematurely, some data sets had to be discarded as they could not be rerun.

Thermal Shock

The in-cylinder pressure transducer was found to have suffered from severe thermal shock while operating at certain of the experimental set-points. This shock was to an extent that readings could not be taken and so runs at these set-points were abandoned.

Less severe thermal shock was found to have effected all runs after the experimental runs were completed. The result of this thermal shock was a lowered pressure reading from approximately the point of peak pressure to around the end of the exhaust stroke.

This influence on the peak pressure reading and exhaust pressure reading was not deemed prohibitive to the studies progress, as comparison of the engine model to the combustion data could still be achieved while keeping these distortions of the data in mind.

The influence of the thermal shock on the high frequency pressure oscillations and so the subsequent KL detection is difficult to determine. This must be kept in mind when comparing data across speeds and boost, as this may influence the thermal shock and the subsequent knock limits detected.

Dyno Failure

The experimental work was cut short due to a dyno speed control issue. The control system lost the ability to maintain the engine at a fixed speed, oscillating at speeds near the set-point given.

This failure was too late in the testing phases to allow time for repair and as such the full experimental matrix initially planned for was not completed.

Final Experimental Matrix

The initial experimental matrix covered a wide range of set points to ensure that knock limited operating conditions would be achieved for the fuels. As expected, due to the differences in octane numbers of the fuels and broad range of operating conditions, certain fuels could not achieve the KL at some of the set points.

Furthermore the described experimental difficulties resulted in a number of set points where data could not be captured.

Tables 3.4, 3.5 and 3.6 show the final experimental matrices for iso-octane, ethanol and ULP 95 respectively with indications of where data was successfully captured. ”NEN” indicates where knock could not be captured as the KL was not reached by the fuel. ”Noise” indicates that the KL was reached but the data ignored as the true KL could not be distinguished due to noise interference on the signal. ”Heat” indicates those traces where severe thermal shock prevented data capture, while ”wet” indicates those traces that were influenced by wetting of the top control thermocouple and thus discarded.

Table 3.4: Final experimental matrix of runs captured for iso-octane

		PFI				MAX				PRE			
	SPEED	1200	2000	3000	4000	1200	2000	3000	4000	1200	2000	3000	4000
BOOST	0.1	✓	✓	✓	NEN	✓	✓	✓	wet	✓	✓	✓	NEN
	0.2	✓	✓	✓	✓	✓	✓	wet	wet	✓	✓	✓	✓
	0.3	✓	✓	✓	✓	✓	✓	wet	wet	✓	✓	✓	✓
	0.4	✓	✓	✓	✓	✓	✓	wet	wet	✓	✓	✓	✓
	0.5	✓	✓	✓	✓	✓	✓	wet	wet	✓	✓	✓	✓

NEN - not enough knock
wet - thermocouple wetting

Table 3.5: Final experimental matrix of runs captured for ethanol

		PFI				MAX				PRE			
	SPEED	1200	2000	3000	4000	1200	2000	3000	4000	1200	2000	3000	4000
BOOST	0.1	NEN	✓	NEN		NEN	NEN			NEN	✓	✓	
	0.2	NEN	✓	✓	noise	NEN	✓			NEN	✓		
	0.3	NEN	✓	✓	noise	NEN	✓	heat		✓	✓		
	0.4	NEN	✓	✓		NEN	✓	heat		✓	✓		
	0.5	✓	✓	✓		NEN	✓			✓	✓		

NEN - not enough knock
noise - transducer noise, no knock detected
heat - severe thermal shock

Table 3.6: Final experimental matrix of runs captured for ULP 95

		PFI				MAX				PRE			
	SPEED	1200	2000	3000	4000	1200	2000	3000	4000	1200	2000	3000	4000
BOOST	0.1	✓	✓	✓	NEN	✓	✓	✓	✓	✓	✓	✓	NEN
	0.2	✓	✓	✓	✓	✓	✓	✓	✓	✓	✓	✓	✓
	0.3	✓	✓	✓	✓					✓			
	0.4	✓	✓	✓	✓								
	0.5	✓	✓										

NEN - not enough knock

Chapter 4

Modelling

This chapter captures the fundamental theory employed in the modelling studies. It details the inlet manifold model, which consists of a steady state model consisting of a number of zones that interact through classic transport phenomena. The combustion model that follows is a two zone zero dimensional model with knock prediction capability. The thermodynamic properties used throughout the modelling are then detailed.

4.1 Overview

The mathematical models employed were required to capture the influence of a fuel's charge cooling and its autoignition chemistry. The modelling was also required to be able to be verified by experimental data that could be captured.

Each model section would serve a particular purpose in capturing and predicting certain aspects of the process:

- The inlet manifold model would capture the required evaporation and fluid flow characteristics taking place in the inlet manifold, where a significant portion of the fuel evaporation and temperature drop was expected to occur.
- The combustion model would capture the compression, combustion and expansion sections of the 4-stroke cycle. This would also be linked to the autoignition model, predicting knock.
- The autoignition model would predict if and when knock would occur in the combustion process and would reside within the combustion model.

A simple model simulating the breathing process, namely the inlet and exhaust strokes of the engine cycle, was also developed to give insight into this process. The details of this can be seen in Appendix F.

The calculation of the various thermodynamic properties used throughout is detailed in Appendix G.

4.2 Inlet Manifold Modelling

4.2.1 Overview

The mathematical model describing the inlet manifold evaporation was required to predict the associated temperature drop of the inlet charge.

The process within the inlet manifold is a highly dynamic process, with rapidly fluctuating pressures occurring throughout the manifold with two-phase flow occurring. However, it was decided that a well thought out one-dimensional model would be able to provide sufficient prediction of the bulk processes at hand. This approach has been used before for this type of modelling [43, 65, 69].

A one-dimensional steady state model was thus chosen. The model is a multiphase model consisting of three zones, namely a film, gas and droplet zone. This is illustrated in Figure 4.1, where the interactions that cause a rate of change of mass ($\dot{m}$), heat ($\dot{Q}$) and momentum ($\dot{m}v$) are shown.

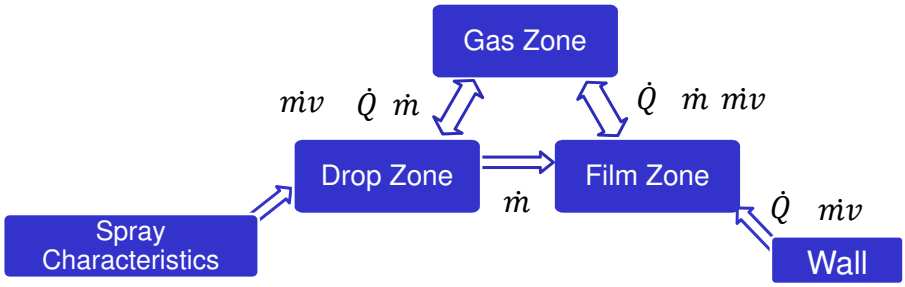

Figure 4.1: Schematic of inlet manifold model

Mass, heat and momentum are transferred between all three zones through classic transport equations. The model includes interactions between the manifold wall and the film and gas zone.

The starting conditions of the gas zone were determined from measurement. The droplet zone starting conditions are determined by the characterisation of the injector spray (detailed in Appendix D.2), while the film condition starting conditions were estimated.

The method used to model the evaporation process, as reviewed in Chapter 2.7.3, was the film theory model, while heat transfer was modelled using the infinite conductivity model. This is the same manner as the previous modelling studies referenced earlier [43, 65, 69]. Wall film motion was accounted for through momentum interactions between the gas and film zone. Droplet deposition was also accounted for and made use of the Friedlander and Johnstone relation as described in Chapter 2.7.5.

This model consisted of a so called initial value problem, which consists of a set of ordinary differential equations with the initial values of the functions specified. This was solved through the use of the Runge-Kutta method.

4.2.2 Governing Equations

The equations were derived through a zonal balance of energy, mass and momentum for the steady state flow of the fluids through the manifold, thus ignoring time. This was done in line with previous models, which can be referenced for further information [43, 53, 54, 61, 65, 69].

A fuller description of the equations can be found in Appendix E, where the relations for the various heat, mass and momentum transfer relations can be found.

Conservation of Energy

This details the effects of the energy transferred on the internal energies of each zone through heating and enthalpy changes due to mass transfer (The influence of the kinetic energy of the mass transferred between zones was ignored, as it was assumed to be of minor significance.)

The conservation of energy equations allow for the prediction of the change in temperature of each zone.

Droplet Zone

$$\dot{m}_d c_{p,d} \frac{dT_d}{dx} = \frac{dQ_{g2d}}{dx} - \frac{d\dot{m}_{d2g}}{dx} h_{fg,d} \tag{4.1}$$

Gas Zone

$$\dot{m}_g c_{p,g} \frac{dT_g}{dx} = -\frac{dQ_{g2w}}{dx} - \frac{dQ_{g2f}}{dx} - \frac{dQ_{g2d}}{dx} \tag{4.2}$$

Film Zone

$$\dot{m}_f c_{p,f} \frac{dT_f}{dx} = \frac{d\dot{m}_{d2f}}{dx} c_f (T_d - T_f) - \frac{dQ_{w2f}}{dx} - \frac{dQ_{f2g}}{dx} - \frac{d\dot{m}_{f2g}}{dx} h_{fg,f} \tag{4.3}$$

where	T	:	temperature
	$\dot{m}$	:	rate of mass transfer
	Q	:	rate of heat transfer
	c_p	:	constant pressure specific heat
	x	:	distance
	h_{fg}	:	enthalpy of vapourisation
subscripts:	f	:	film zone
	g	:	gas zone
	d	:	droplet zone
	w	:	wall zone
	$g2d$	:	transport from gas to droplet zone etc

Conservation of Mass

This details the effects of the mass transferred between zones, through evaporation of the film and droplets and impingement of the droplets onto the film.

This allows for the prediction of the change of the droplet diameter, film thickness and gas density.

Droplet Zone

$$(\frac{1}{2}\rho\pi nD^2)\frac{dD}{dx} = -\frac{d\dot{m}_{d2g}}{dx} \tag{4.4}$$

Gas Zone

$$\rho_g\frac{d\rho_g}{dx} = (\frac{1}{A_g v_g \rho_g}\left(\frac{d\dot{m}_{d2g}}{dx} + \frac{d\dot{m}_{f2g}}{dx}\right) - \frac{A_g}{dx}\frac{1}{A_g} - \frac{dv_g}{dx}\frac{1}{v_g} \tag{4.5}$$

Film Zone

$$(v_f\pi d_m)\frac{dt_f}{dx} = \frac{1}{\rho_f}\left(\frac{d\dot{m}_{d2f}}{dx} - \frac{d\dot{m}_{f2g}}{dx}\right) - \frac{dv_f}{dx}\pi d_m t_f \tag{4.6}$$

where	D	:	diameter of droplet
	n	:	number of droplets passing per second
	t_f	:	thickness of film
	$\dot{m}$	:	mass transfer
	x	:	distance
	v	:	speed
	ρ	:	density
	A	:	cross sectional area
	d_m	:	diameter of manifold pipe
subscripts:	f	:	film zone
	g	:	gas zone
	d	:	droplet zone
	w	:	wall zone
	$g2d$	:	transport from gas to droplet zone etc

Conservation of Momentum

This section details the effects of the momentum influences between the zones, where interaction occurs through friction and drag forces between the gas and the film and droplet zones respectively, as well as the influence of the momentum transfer when mass is transferred.

This allows for the prediction of the velocities of the various zones.

Droplet Zone

$$(\frac{1}{6}n\pi D^3\rho)\frac{dv_d}{dx} = \tau_{gd}\frac{n}{v_d} \tag{4.7}$$

Gas Zone

$$\rho_g A_g v_g \frac{dv_g}{dx} = A_g\frac{dp_g}{dx} - \tau_{gf}s_g - \tau_{gw}s_w - \dot{m}_d\frac{dv_d}{dx} + v_d\left(-\frac{dm\dot{}_{d2g}}{dx} - \frac{dm\dot{}_{d2f}}{dx}\right) - v_g\left(\frac{dm\dot{}_{d2g}}{dx} - \frac{dm\dot{}_{f2g}}{dx}\right) \tag{4.8}$$

Film Zone

$$\dot{m}_f\frac{dv_f}{dx} = \tau_{gf}s_f - \tau_{wf}s_f - v_f\left(\frac{dm\dot{}_{d2g}}{dx} - \frac{dm\dot{}_{f2g}}{dx}\right) \tag{4.9}$$

where	D	:	diameter of droplet
	n	:	number of droplets passing per second
	$\dot{m}$	:	mass transfer
	τ	:	shear force
	s	:	perimeter
	x	:	distance
	v	:	speed
	p	:	pressure
	ρ	:	density
	A	:	cross sectional area
subscripts:	f	:	film zone
	g	:	gas zone
	d	:	droplet zone
	w	:	wall zone
	$g2d$	:	transport from gas to droplet zone etc

Ideal Gas Law

A derivative form of the ideal gas law was required to determine the change in pressure of the gas from the change in gas temperature and density.

$$\frac{1}{p_g}\frac{dp_g}{dx} = \frac{1}{\rho_g}\frac{d\rho_g}{dx} + \frac{1}{T_g}\frac{dT_g}{dx} \tag{4.10}$$

where	T	:	temperature
	x	:	distance
	v	:	speed
	p	:	pressure
	ρ	:	density
subscripts:	f	:	film zone
	g	:	gas zone
	d	:	droplet zone
	w	:	wall zone
	$g2d$	:	transport from gas to droplet zone etc

4.2.3 Model Validation

Single Droplet Vapourisation

The evaporation of a single n-heptane droplet was compared with literature results for forced convection evaporation, provided by Diaf et al. [78].

The results can be seen in Figure 4.2, and show good correlation.

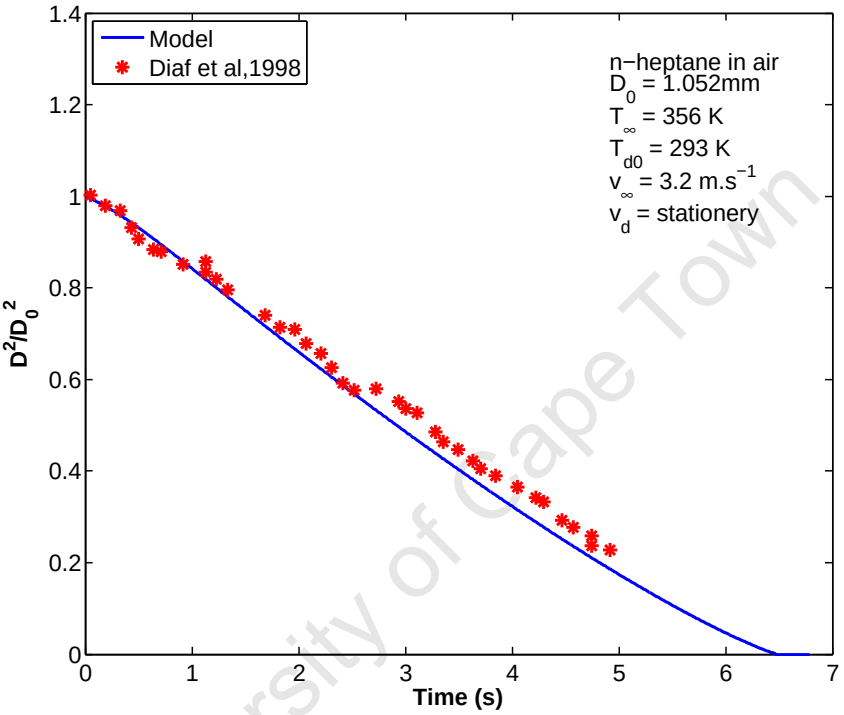

Figure 4.2: Single n-heptane droplet evaporation, compared to results from Daif et. al. [78]

Inlet Manifold Modelling

The implementation of the model was compared to that of Moran's implementation of essentially the same model [43]. Figure 4.3 shows the comparison for the evaporation of ethanol in the inlet manifold.

Larger differences between the model were seen initially. However after going through the sample code provided by Moran, differences in fuel property values were seen in those calculations that were shown. Changing the models property calculation to match that of Moran's then produced the fit seen. Only a small portion of the property calculation was shown. It is felt that the use of all of his property calculations would further improve the correlation between the two models.

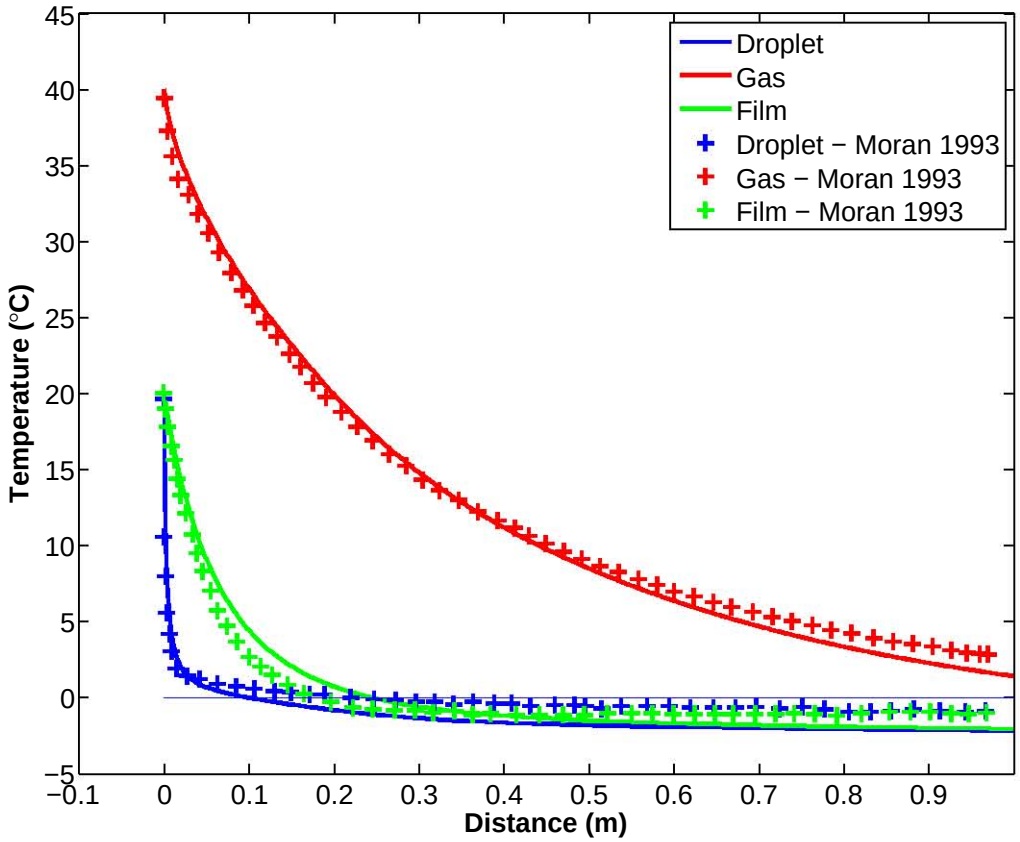

Figure 4.3: Evaporation of ethanol in a manifold, compared to results from Moran [43]

4.3 Combustion and Knock Model

4.3.1 Overview

A combustion and knock model was developed to simulate the engine processes of compression, combustion and exhaust with knock prediction capabilities. A two-zone model was employed, consisting of an unburnt and burnt zone, with the combustion process transferring mass between the zones and an energy balance applied to each zone to account for the changes in internal energy as a result of the various heat and enthalpy exchanges.

A two-zone model was chosen as it is the simplest model that still provides accurate enough knock prediction capabilities, as shown in previous work [10,40]. A single zone model would produce a zone temperature that would be between the burnt and unburnt zone temperatures of a two zone model. A knock model thus using this single zone temperature would be using a higher temperature than reality and thus over predict knock.

This model required the solution of a set of non-linear equations. The Newton-Rhapson method was employed to solve this system directly.

The engine model implemented was taken in large from the content of the course Engine Thermodynamics and Combustion [79].

4.3.2 Governing Equations

Conservation of Energy

An energy balance was applied to both zones, treating them as open control volumes for each time step:

$$m_{z,i}u_{z,i} - m_{z,i}u_{z,i} + 0.5(p_i + p_{i-1})(V_{z,i} - V_{z,i-1}) - h_{out}\delta m_{out} + h_{in}\delta m_{in} - \Delta Q_i = 0 \quad (4.11)$$

where	m	:	mass
	u	:	internal energy
	p	:	pressure
	V	:	volume
	h	:	enthalpy
	Q	:	heat
subscripts:	z	:	refers to the relevant zone, either burnt or unburnt
	u	:	unburnt zone
	b	:	burnt zone
	i	:	time step

Ideal Gas Law

The Ideal gas law was applied to the zone constituents:

$$\frac{TR_z m_{z,i}}{M_{z,i}} - p_i V_{z,i} = 0 \quad (4.12)$$

where	m	:	mass
	p	:	pressure
	V	:	volume
	T	:	temperature
	M	:	molar mass
subscripts:	z	:	refers to the relevant zone, either burnt or unburnt
	i	:	time step

Conservation of Volume

A volume balance was applied to the zones:

$$V_{cyl,i} - V_{b,i} - V_{u,i} = 0 \tag{4.13}$$

where	V	:	volume
subscripts:	cyl	:	entire cylinder
	u	:	unburnt zone
	b	:	burnt zone
	i	:	time step

Combustion Mass Transfer

The Wiebe function was used to describe the transfer of mass from the unburnt to the burnt zone. This function is a statistical fit to the heat release profile and is a commonly used empirical fit [8].

The function has the form of

$$x_b(\theta) = 1 - e^{\left[-b\left(\frac{\theta-\theta_0}{\Delta\theta}\right)^{m+1}\right]} \tag{4.14}$$

where	x_b	:	fraction of fuel burnt
	θ	:	crank angle
	$\Delta\theta$	:	burn duration
	b	:	fitting coefficient
	m	:	fitting coefficient
subscripts:	b	:	burnt zone
	0	:	start of combustion

The energy release associated with combustion is subsequently accounted for through the increase in mass of the burnt zone consisting of burnt products, thus simulating combustion. Due to their lower state enthalpy, the burnt zone must be at a higher temperature to contain the same amount of energy as the unburnt reactants that have been transferred to the burnt zone.

The Wiebe function parameters m and b are determined by fitting to the experimental heat release.

Borg and Alkidas [80] illustrate the use of two approaches to Weibe parameter fitting. The first involves relaxing the constraints on the various parameters, as this allows for a better fit of the cumulative and net heat releases. The second involves restricting those parameters that have some physical significance. Thus the start of combustion is set to the spark timing and the b fitting coefficient is set to 6.90, which thus sets the end of combustion at 99%.

The approach that was found to work well was the setting of the Wiebe function to start at spark timing while the rest of the parameters were relaxed and allowed to fit the data supplied.

Additionally, the occurrence of knock complicated the fitting. The heat release profile could not be fit as a whole, as the knock produces a second distinct peak in the heat release. Figures 4.4 shows this second knock peak.

The two peaks were thus split, using the knock point detected at the valley between the two peaks (described in Appendix B.3). A Wiebe function was fit to the front non-knocking section of the heat release up until the knock point.

The fitting was done by minimising the error between the actual and fitted Wiebe function at the 0 , 5 , 10 , 50 , 60 and 80 % of the mass fraction burnt, normalised to the non-knocking section of the heat release profile. This method of using data points to fit was drawn from Yeliana et al. [81] and with the points modified to suit.

Figure 4.4 shows a sample fit. The fit after the knock point plays no role in the analysis, but a fast Wiebe burn was included and thus plotted for completeness sake.

Dissociation

The burnt zones chemical composition will be influenced by dissociation of the combustion products due to the zones high temperature. The carbon dioxide dissociation and the water-gas shift reaction were used to represent dissociation. The full details of the dissociation influence on the product composition can be seen in Appendix G.

Heat Loss

The rate of heat transfer to the combustion walls of an engine is described by

$$\frac{\Delta Q_i}{dt} = A h_c (T - T_w) \Delta t \tag{4.15}$$

During combustion, when two zones were present, the cylinder wall area was proportionally split between the two zones based on their respective volume fraction of the total cylinder [82].

A common method of determining the heat transfer coefficient h is the Woschni correlation [68]. Apon determination of the heat release profiles of motored pressure traces (sans fuel injection) using the same method as that used for the burn rate heat release described in Appendix B.4, it was found that the Woschni correlation was found to under predict the heat loss of the motored runs. This can be seen in Figure 4.5. Another correlation was thus used, namely that of Annand, and was found to fit the data far better.

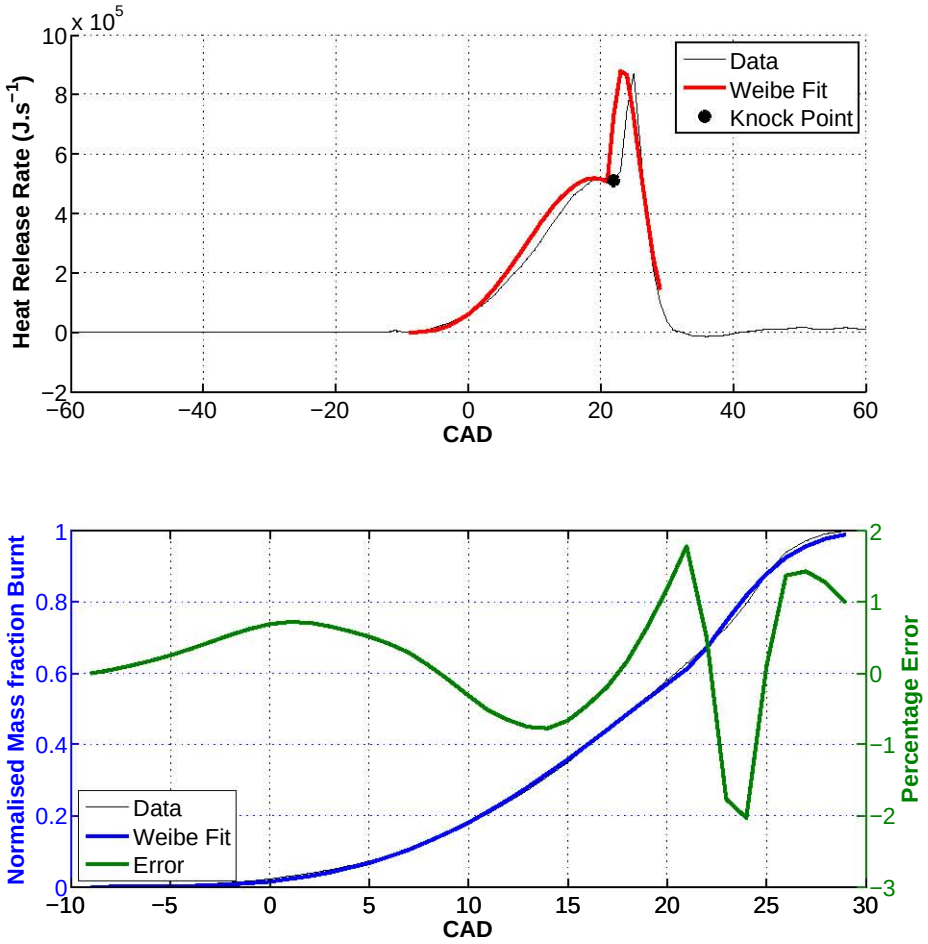

Figure 4.4: Fit of Wiebe function to heat release (iso-octane Max 1200 RPM 0.3bar boost)

The Annand correlation determines the heat transfer coefficient through the relation [8]

$$h_c = a\frac{k}{B}(\frac{\rho S_p B}{\mu})^b \tag{4.16}$$

where
h_c : averaged heat transfer coefficient of the combustion walls
ρ : density
B : bore
k : thermal conductivity
S_p : piston speed
μ : dynamic viscosity
a : fitting coefficient
b : fitting coefficient

The properties are all calculated at the average instantaneous cylinder temperature.

The comparison of the two correlations can be seen in Figure 4.5, where the Annand heat loss correlation better predicts the heat lost by the engine while being motored.

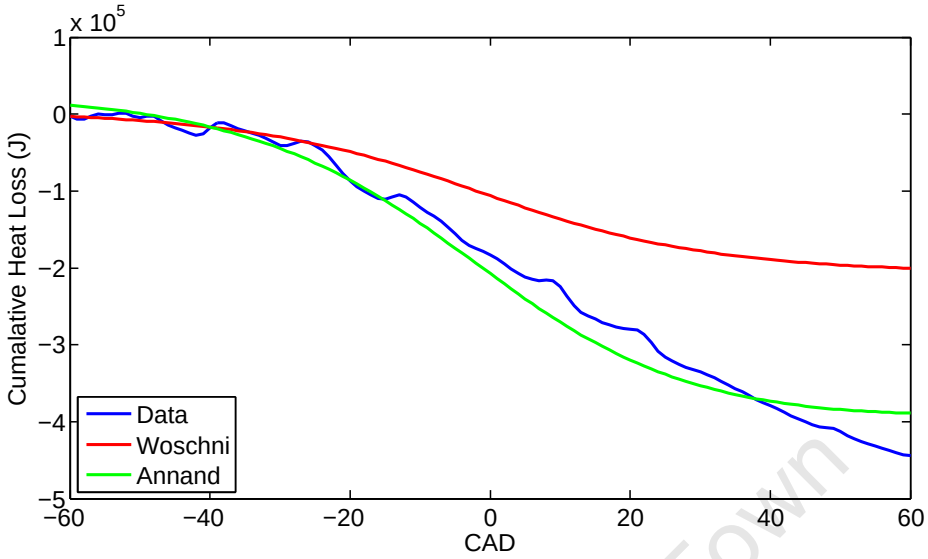

Figure 4.5: Comparisons of heat loss correlations for motored traces

Knock

The knock model was employed through the use of the Livengood and Wu integral [46] and the Yates et al. [10] autoignition time prediction, as described in Chapter 2.6.

Figure 4.6 illustrates the implementation for iso-octane, showing good fits between data from a detailed kinetic study of the autoignition delay of iso-octane from Yates et al.'s 2005 paper [37], the original Yates et al. 2005 model [37], the Yates and Viljoen 2008 model [40] and the currently employed Yates et al. 2010 model [10].

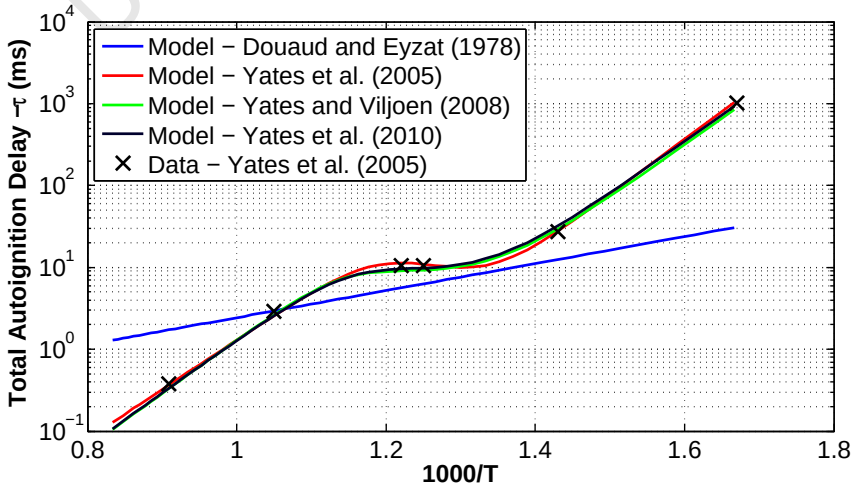

Figure 4.6: Comparison of empirical models reviewed, for iso-octane at 30 bar

Chapter 5

Inlet Manifold Results and Discussion

This chapter firstly reviews the inlet manifold temperature profiles recorded and then details the comparison of the profiles with the modelled results. This allows for conclusions regarding the evaporation process that occurred within the manifold and the charge cooling influence of the fuels.

5.1 Inlet Manifold Data

5.1.1 Motored Conditions

The inlet manifold temperature profiles with the engine motoring on air only are shown in Figures 5.1 and 5.2. Figure 5.1 shows the MAX manifold conditions, which has the air inlet temperature at the top of the manifold controlled to 50℃. Figure 5.2 shows the PRE manifold condition, which has the air inlet temperature controlled at the bottom of the manifold to 50℃.

Speed was shown to have an unexpected influence on the temperature profile seen along the manifold. Under all boost conditions, at low speeds 1200 RPM) the temperature was seen to decrease along the manifold, while at high speeds (4000 RPM) the temperature was seen to increase along the manifold and at the intermediate speeds the temperature profile stays approximately constant.

Boost was shown to have little effect on the temperature gradients.

Results from the thermocouples on the inside of the manifold, between the manifold and the Teflon liner and on the outside of the manifold, showed that heat was being lost by the manifold to the atmosphere at all speeds.

The reason for these gradients were unknown. All future temperature measurements were compared to these motored conditions with these profiles used as a baseline. The temperature profiles that follow will thus show the 'Temperature Difference', which is the difference between the temperature readings and the baseline readings obtained from these motored runs.

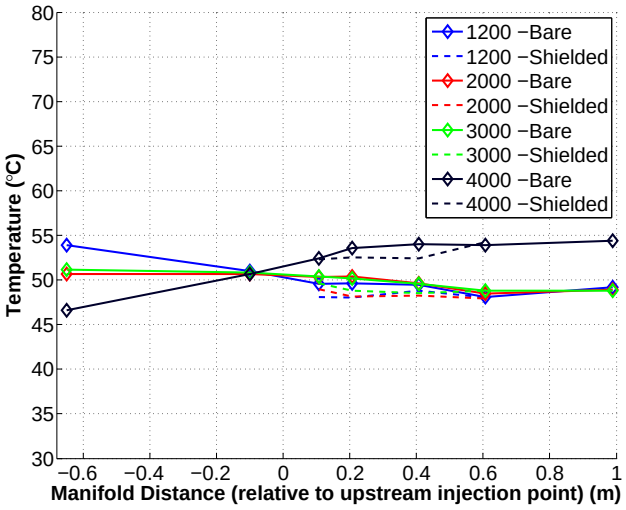

Figure 5.1: Inlet manifold temperature profile - motored MAX conditions, 10 kPa

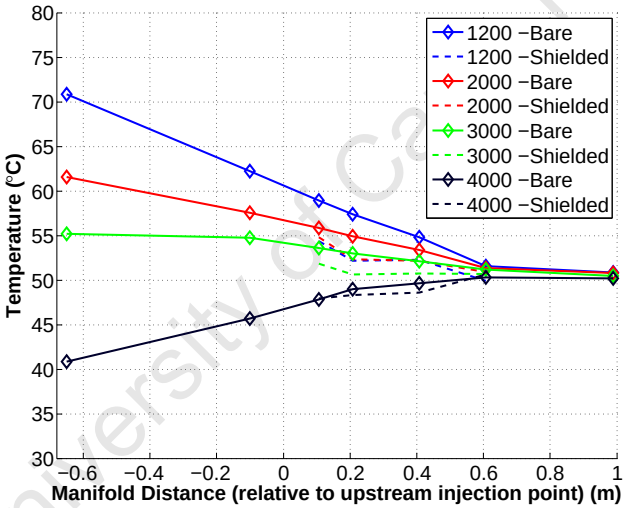

Figure 5.2: Inlet manifold temperature profile - motored PRE conditions, 10 kPa

5.1.2 iso-Octane

A temperature profile along the length of the manifold while running on iso-octane under the PRE control condition can be seen in Figure 5.3 while the MAX condition can be seen in Figure 5.4.

The temperature drop of a stoichiometric AF mixture if the fuel fully evaporates and draws all its energy from the air would be 21 ℃ for iso-octane [83].

The overall temperature drop experienced within the manifold for both the MAX and PRE manifold conditions from the thermocouple (at the -0.1m mark) just before the injection of the fuel to the final thermocouple is approximately 20 ℃ and this is thus in line with the temperature drop expected if iso-octane fully evaporates.

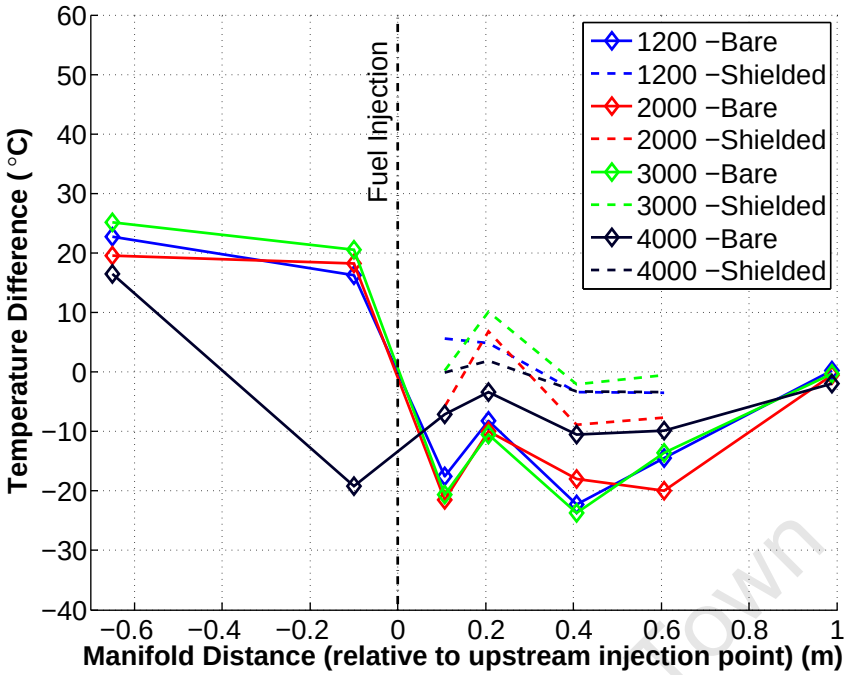

Figure 5.3: Inlet manifold temperature profile - iso-octane PRE Conditions, 10 kPa

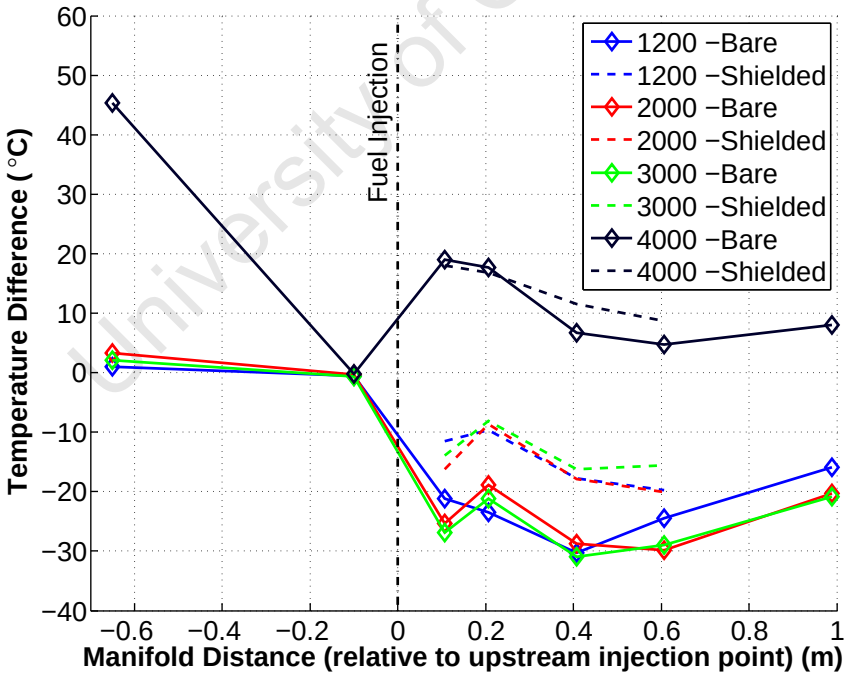

Figure 5.4: Inlet manifold temperature profile - iso-octane MAX conditions, 10 kPa

However, in the iso-octane case, the temperature rises for the MAX and PRE cases from the 0.6m mark to the 1m mark. This results in the bare thermocouple reading at the 1m mark registering higher temperatures than the shielded thermocouples

upstream of it. This is thought to be caused by the combination of the shielded thermocouples not reading a true gas temperature due to wetting by liquid fuel and the diminished quantity of fuel at the 1m mark. Thus the bare thermocouple at the end of the manifold would be reading a greater proportion of the gas temperature and thus register a higher temperature than the upstream shielded thermocouple.

All manifold cases, both for iso-octane and as will be seen shortly for ethanol and ULP 95, exhibit an unexpected deviation in temperature at the 0.2m mark. A justifiable cause for this puzzling bump, identified early on in the experimental work, has not been suggested. Perhaps a strange flow phenomenon such as a high turbulence zone that prevents the deposition of fuel droplets on the thermocouples, thus allowing the thermocouple to register gas temperatures. A faulty thermocouple reading may have been the cause, but the thermocouples were rechecked and swapped repeatedly with no change and thus this is not considered a viable cause.

The temperature drop at higher speeds before the injection point at the 0 m mark, caused by wetting of the thermocouple by the fuel, has been described briefly in Chapter 3.3. This wetting phenomenon ties up with the explanation of the odd temperature bump at the 0.2m mark, as both could be caused by unusual turbulence, which is plausible considering the dynamic nature of the engine flow processes and the lack of tuning of the inlet manifold. Those MAX runs that experience this wetting problem, primarily at the higher boosts, have been excluded from the analysis.

The shielded thermocouples register higher temperatures than the bare thermocouples, which follows the original reasoning that they would measure more of the gas temperature. They do not, as was hoped, show any signs of converging with the bare thermocouples, which would have given an indication of the fuel being fully evaporated.

The influence of speed on the cooling cannot be distinguished, as the highest speed runs suffer from the thermocouple wetting. There is no significant difference seen for the non-wetted speeds.

5.1.3 Ethanol

A sample of the temperature profile of ethanol running under MAX conditions can be seen in Figure 5.5 while under PRE conditions can be seen in Figure 5.6.

The temperature drop of a stoichiometric AF mixture if the fuel fully evaporates and draws all its energy from the air would be 85℃ for ethanol [83].

Both manifold conditions show the influence of the high heat of vapourisation of ethanol. The MAX case has a temperature profile that is completely flat with a temperature drop of approximately 30℃. This is thought to be the fuel droplet temperature that is being recorded, as the amount of liquid fuel present in the manifold should overwhelm any chance of measuring the gas temperature. This temperature drop falls well short of the theoretical maximum of 85℃ and highlights how the full charge cooling potential of ethanol cannot be fully realised.

The PRE case shows a temperature drop of approximately 200℃ along the manifold. This is due to the high temperature that the inlet air had to be heated to force the

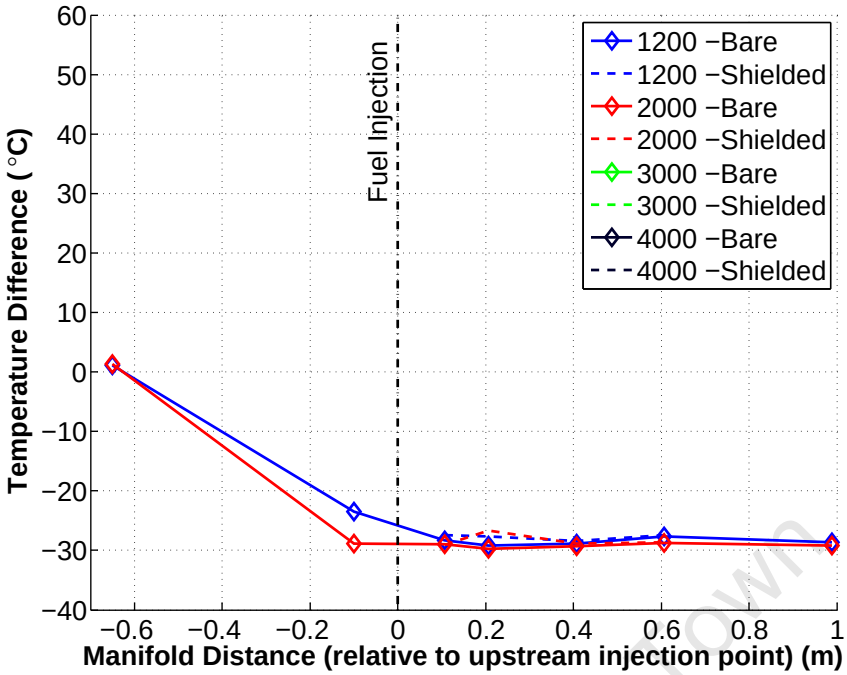

Figure 5.5: Inlet manifold temperature profile - ethanol MAX conditions, 10 kPa

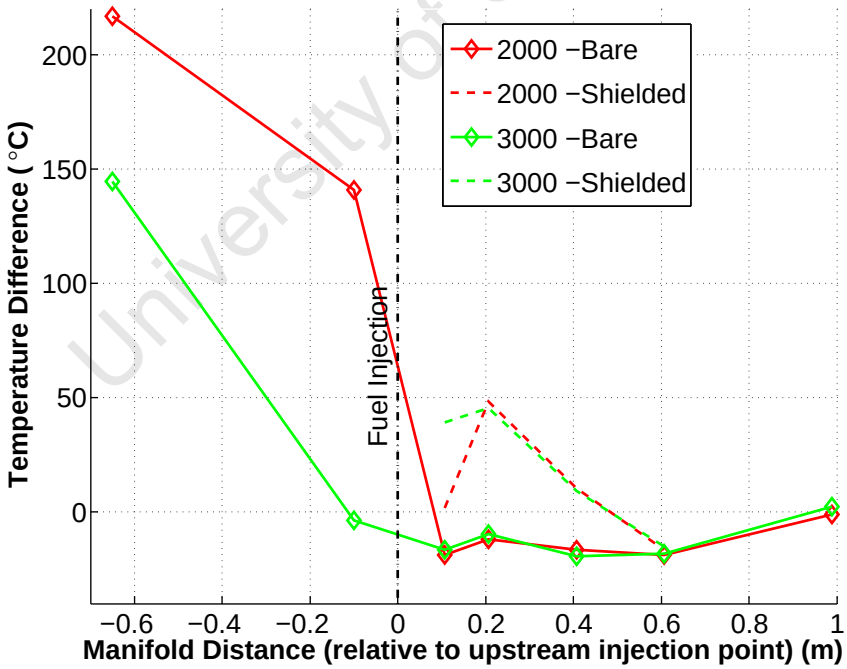

Figure 5.6: Inlet manifold temperature profile - ethanol PRE conditions, 10 kPa

bottom control thermocouple to a temperature of 50℃. It is suggested that this high temperature was required to not fully evaporate the fuel but rather heat the gas and fuel droplets to an extent that a 50℃ temperature could be registered. This phenomenon

is discussed further in the following chapter.

Both figures show signs of thermocouple wetting. However the MAX profiles were corrected for the top control thermocouple wetting and so they were controlled to the heater temperature, as discussed in Chapter 3.3, and are thus valid runs.

The odd temperature bump at the 0.2 m mark is present in the ethanol PRE runs, as it was in the iso-octane runs.

5.1.4 ULP 95

Figure 5.7 shows a ULP 95 PRE run while Figure 5.8 shows a temperature profile for a MAX run.

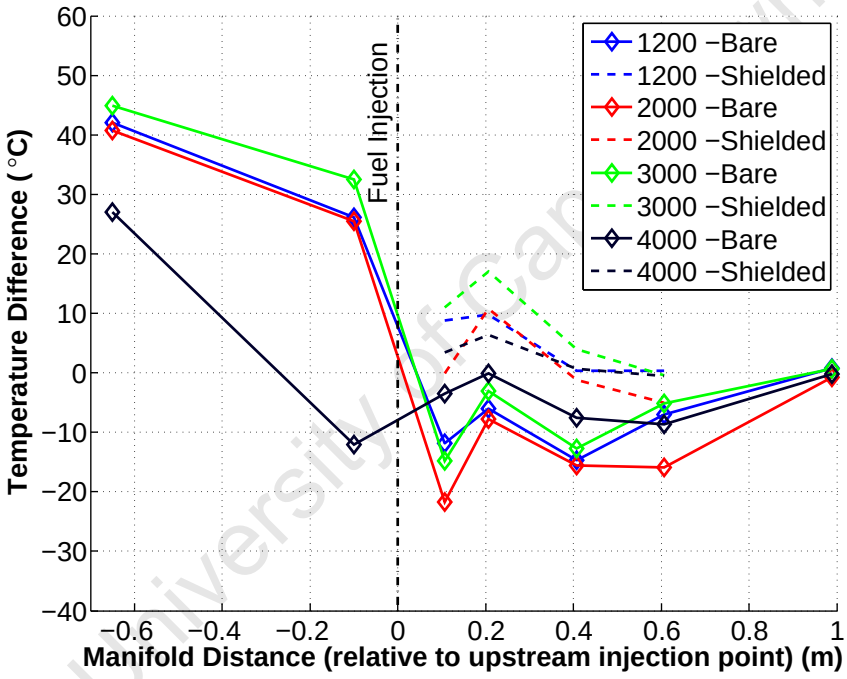

Figure 5.7: Inlet manifold temperature profile - ULP 95 PRE conditions, 10 kPa

The ULP 95 temperature profiles matched closely with the iso-octane profiles. Both fuels have similar heats of vapourisation but with ULP 95 consisting of a blend of components with a range of vapour pressures. This difference was not seen to have any discernible effect on the temperature profiles.

ULP 95 followed the same trends as iso-octane, such as the approximately 20℃ temperature drop, the increase in temperature from the 0.6 m to 1m mark, the shielded thermocouples registering higher temperatures and the odd bump in temperature at the 0.2 m mark. It should be noted that ULP 95 MAX runs were was corrected for the thermocouple wetting control issue.

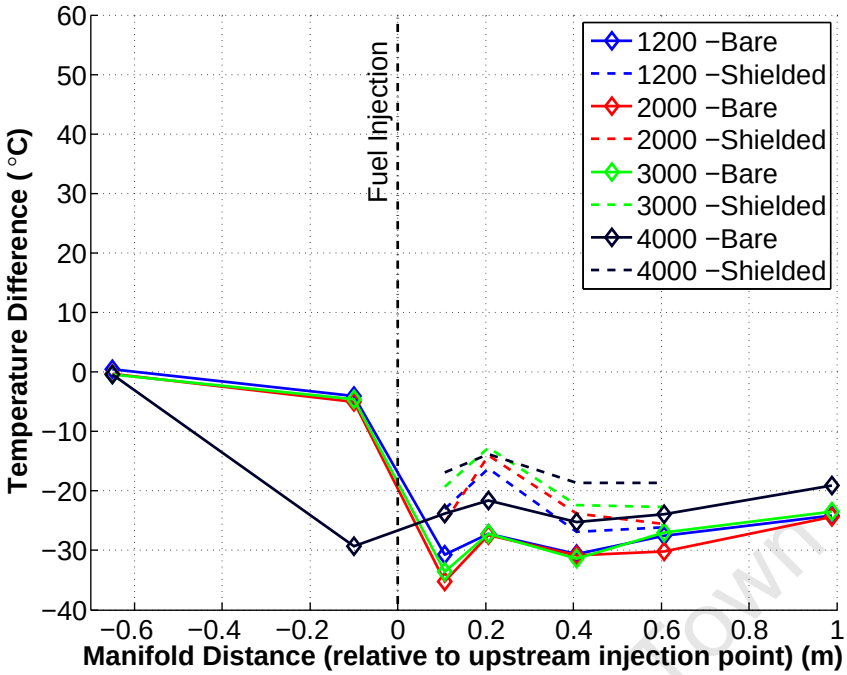

Figure 5.8: Inlet manifold temperature profile - ULP 95 MAX conditions, 10 kPa

5.2 Inlet Manifold Modelling

5.2.1 Input Parameters of Model

The input parameters for the inlet manifold evaporation modelling are shown in Table 5.1.

Table 5.1: Inlet manifold modelling inputs

Initial ethanol droplet diameter D_0	μm	120
Initial iso-octane droplet diameter D_0	μm	100
Initial film fraction		0.5
Initial droplet velocity $V_{d,0}$	$m.s^{-1}$	20
Pipe diameter D_{pipe}	mm	34
Initial pressure $p_{g,0}$	bar	1+ boost
Film area		constant

The initial droplet sizes were derived from the Injector Characterisation, which is detailed in Appendix D. The remainder of the parameters were chosen based on those used by Moran [43] in a similar study. The initial film area and film fraction in particular were impossible to determine due to the construction of the inlet manifold and so approximates based on Moran's insights were used.

5.2.2 iso-Octane

MAX

A sample of the results of the modelling study of the iso-octane evaporation occurring under MAX conditions are shown in Figure 5.9. The bare thermocouple readings, which were meant to capture the droplet temperatures, align with the modelled droplet temperatures at the 0.1, 0.4 and 0.6 m mark.

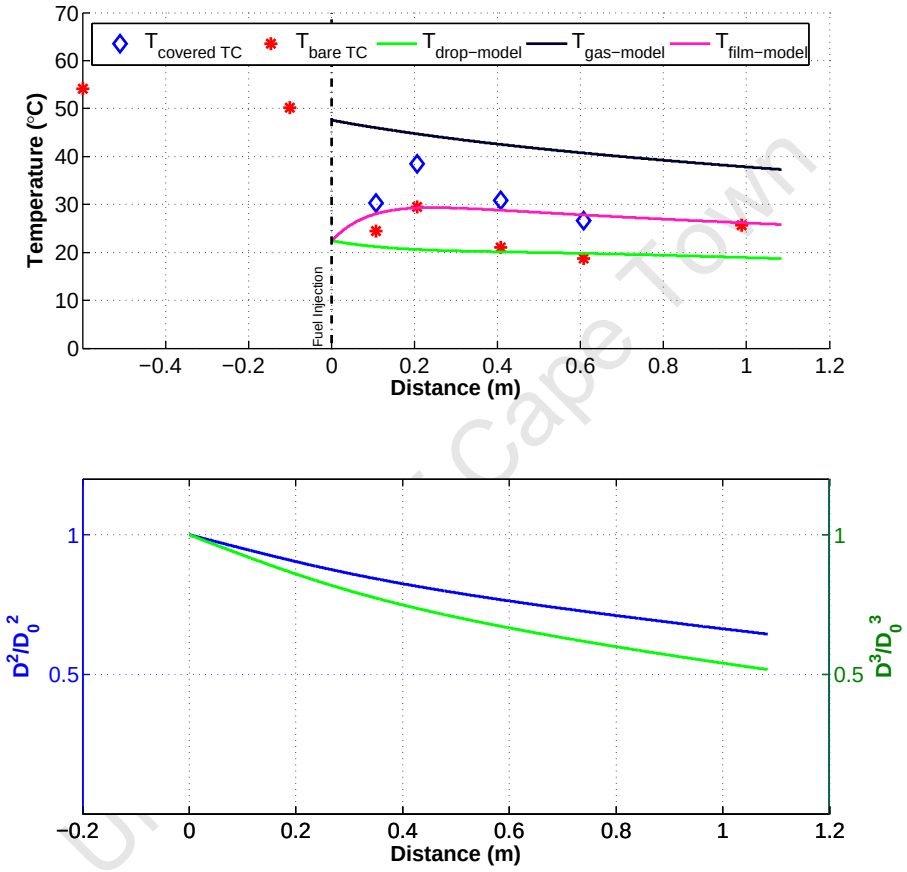

Figure 5.9: Modelling of inlet manifold evaporation - iso-octane MAX 20 kPa 2000 RPM

The end temperature at the 1m mark is however between the modelled droplet and gas temperatures. This indicates either a failure of the model to predict the droplet temperatures at this point or that the temperatures measured by the bare thermocouples are not always a true reflection of the droplet temperatures. It is felt that it is the latter option, as the model has been used with success and experimentally validated previously, as detailed in Chapter 2.7, and the assumption that the bare thermocouple will only ever measure pure droplet temperatures is an unsupported one.

The temperature bump seen in the experimental data at the 0.2 m mark is not captured by the model. However, if this is a turbulence phenomenon, it is then beyond the capabilities of this model.

The covered thermocouples are shown in Figure 5.9 to not be correlated to the gas or droplet temperatures, but fall somewhere in between the two. These thermocouples were an optimistic attempt at capturing whether complete evaporation had taken place by their convergence with the bare thermocouples and so this lack of correlation is not a major concern.

The gas temperature cools as the droplets evaporate, and by the end of the manifold it has decreased by approximately 10℃. This is only about half of the maximum temperature drop that iso-octane can theoretically cause, and as the lower plot of Figure 5.9 shows this is because only 50 % of the mass of the droplet has evaporated by the end of the manifold.

This plot highlights how the full evaporation potential of iso-octane is not utilised in decreasing the temperature of the gas in this extended inlet manifold under the MAX conditions, a finding that mirrors that of Moran's [43].

PRE

The model of iso-octane PRE evaporation in the inlet manifold can be seen in Figure 5.10.

The modelling of the PRE runs was hampered by the wetting of the top control thermocouple as a starting temperature of the gas was thus not known. Using the non wetted runs as a baseline, the modelling was done with the starting gas temperature for iso-octane equal to 0.98 of the heater temperature in Kelvin (the measurement at the -0.6. m mark) and for ethanol to 0.9 of the heater temperature in Kelvin.

The model indicates that the purpose of the PRE manifold case was not met, as full evaporation of the iso-octane was not achieved at the end of the manifold nor was the end gas temperature 50℃.

The gas temperature drop is shown to be approximately 20℃, which indicates the majority of the cooling potential of the iso-octane has been used none the less.

The difference in end gas temperature between the MAX and PRE cases, namely 60℃ in the PRE case and 40℃ in the MAX case, does still allow for comparison between the two cases to see the influence of the cooling on the knock resistance. However this difference of 20℃ between the two cases is greater than would be expected had the control strategies been correct.

5.2.3 Ethanol

MAX

A sample of the ethanol MAX evaporation modelling is shown in Figure 5.11. This plot shows fair correlation between the modelled droplet temperatures and the bare

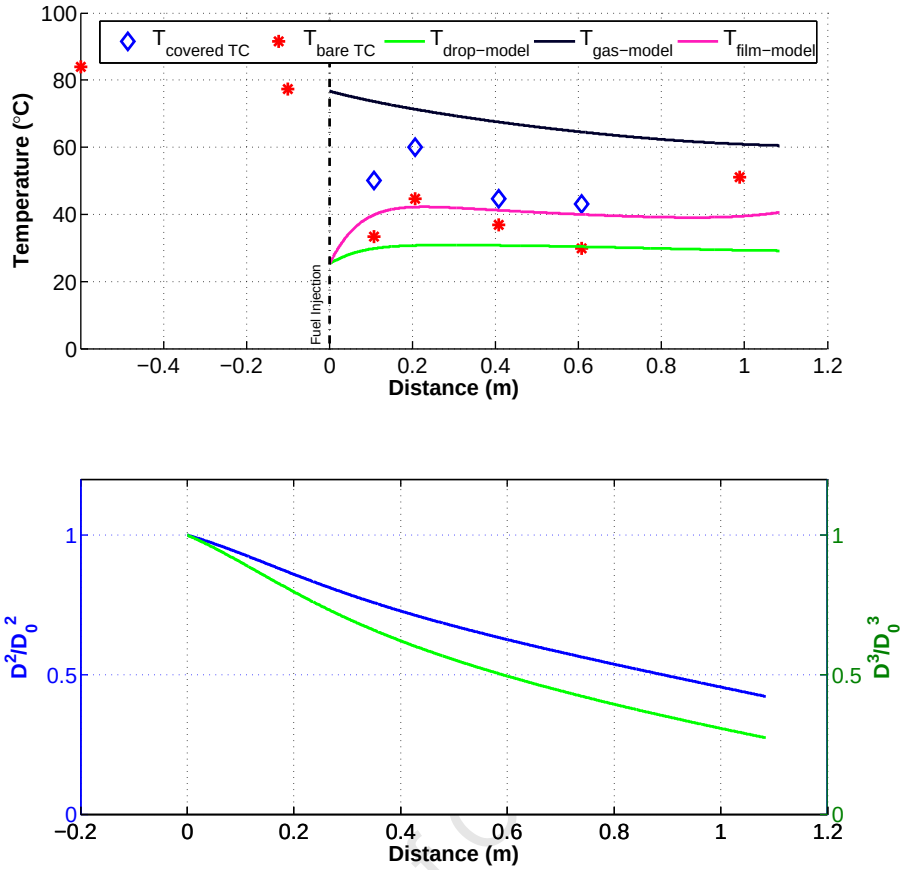

Figure 5.10: Modelling of inlet manifold evaporation - iso-octane PRE 20 kPa 2000 RPM

thermocouple readings at the beginning of the manifold and then the model predicts greater cooling of the droplets than that shown by the bare thermocouple readings.

Once again the modelled droplet temperature is significantly lower than the temperature registered by the bare thermocouple at the 1m mark. As with iso-octane, this could be caused by the thermocouple not registering a true droplet temperature. The large proportion of the fuel still in liquid form, especially compared to the iso-octane case, would suggest that the thermocouple should still register the droplet temperature. It is thus difficult to say whether this is a modelling inaccuracy or a measurement inaccuracy.

The covered thermocouples registered the same temperatures as the bare thermocouples with ethanol, which may be an indication of the overpowering influence of the large amount of liquid fuel present along the length of the manifold.

The lower plot in Figure 5.11 indicates that 80 % of the droplet mass will still be present at the end of the manifold. Thus most of the fuel is still in liquid form and only a small portion of the possible cooling influence of ethanol has been realised, approximately 20℃ in this case. This agrees with Moran's findings on a similar study conducted

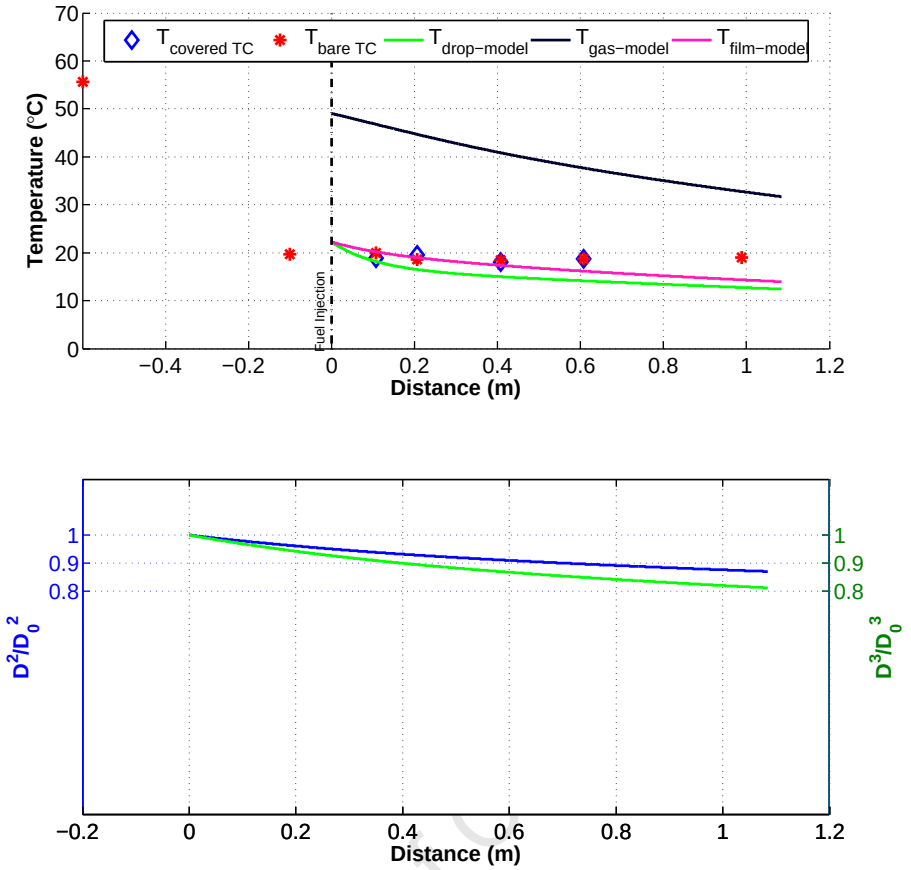

Figure 5.11: Modelling of inlet manifold evaporation - ethanol MAX 20 kPa 2000 RPM

with methanol, which also has a high heat of vapourisation. This study found that only a small portion of the fuel's large theoretical charge cooling capacity could be realised [43].

PRE

An example of the ethanol PRE evaporation modelling can be seen in Figure 5.12. The high initial temperature that was required to register a 50 ℃ reading at the bottom thermocouple is reflected in the large initial gas temperatures that are required, with the final gas temperature above 100 ℃ at the end of the manifold. Additionally, a 70 ℃ temperature drop occurs along the manifold by the gas, indicating that a large proportion of ethanol's cooling power is consumed by the heated gas.

However, just as with iso-octane PRE runs the end gas temperature is well above the 50 ℃ mark that the control strategy planned to obtain. Furthermore the full evaporation is not achieved, with 40% of the droplet mass still remaining in the manifold.

This seems to indicate that the ethanol PRE runs were in fact conducted at far higher initial gas temperatures than iso-octane due to the excessive heating required to

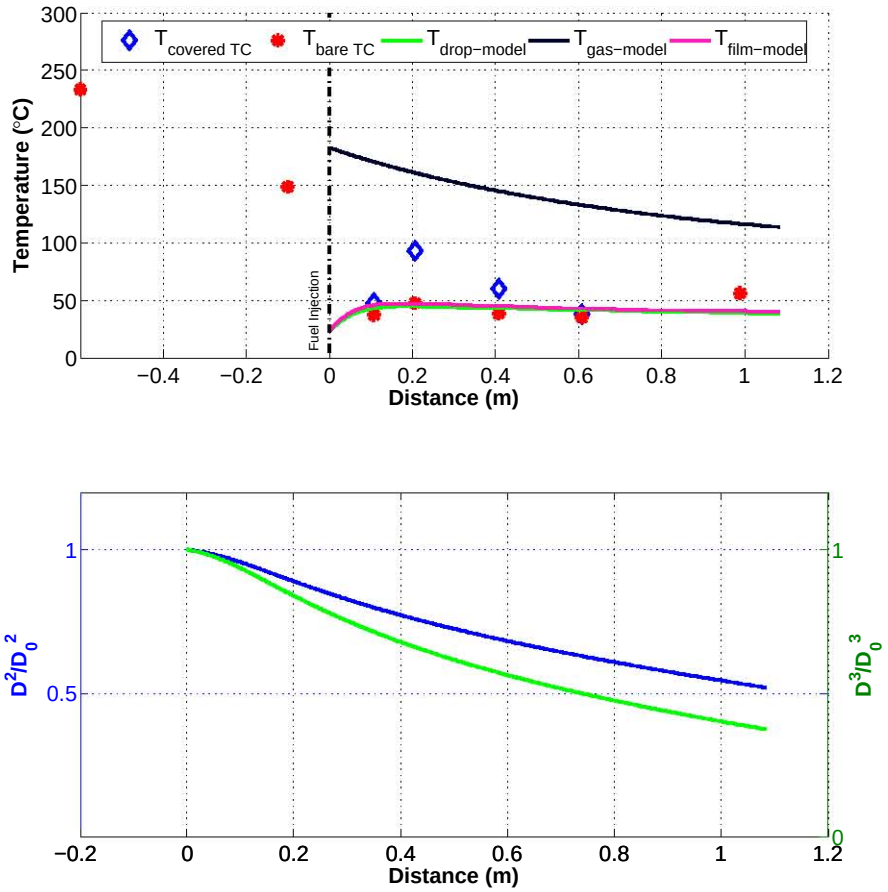

Figure 5.12: Modelling of inlet manifold evaporation - ethanol PRE 20 kPa 2000 RPM

register the 50 ℃ temperature at the bottom thermocouple.

5.2.4 Simulated Speed Influence

The influence of speed on the cooling of the gas under idealised conditions is investigated in Figure 5.13. Here the model was run with a starting temperature of 50 ℃ to see the influence of speed on the temperature drop along the manifold length.

These runs show that iso-octane provides approximately between 8 to 13 ℃ charge cooling, while ethanol provides approximately 11 to 17 ℃ charge cooling. This highlights how, despite ethanol's far greater heat of vapourisation, the cooling between the two fuels is very similar with a difference of only about 4 ℃. Thus the majority of ethanol's charge cooling capacity is not met.

Furthermore this difference of about 4 ℃ in final temperatures between the two fuels is approximately constant across the speed range.

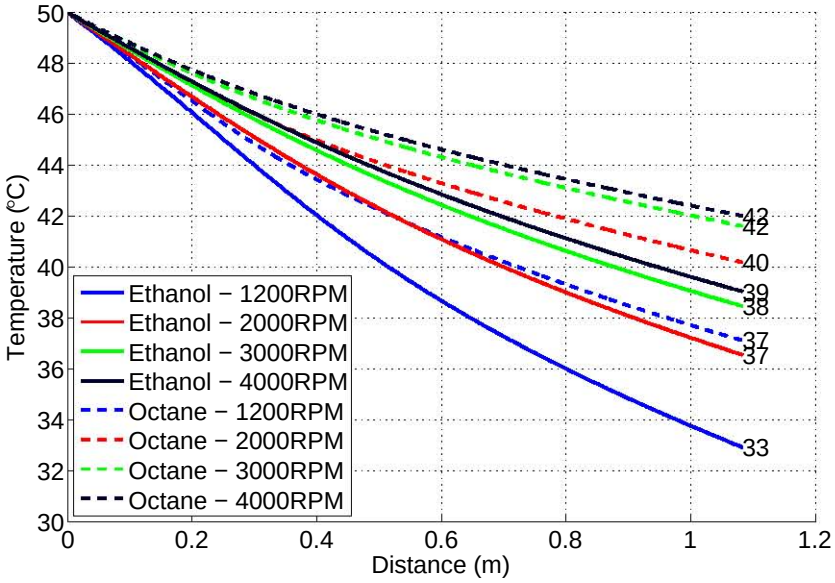

Figure 5.13: Modelled gas temperature profile in manifold with the same fixed start temperature

5.2.5 Chapter Review

Insight into Experimental Work

The modelling of the simulated runs highlighted a number of differences between the original experimental goals for the inlet manifold control strategies for the MAX and PRE cases and the achieved experimental conditions.

The model fits of the data shows that for the PRE manifold case the full evaporation of the fuels along the length of the manifold did not occur, nor was the inlet air temperature at the end of the manifold the goal temperature of 50℃. The model fits of the data also show that the PRE case had large differences in the end gas temperature, which was not the initial aim of the control strategy.

The model shows the MAX manifold condition did not make use of all of the cooling potential of the fuels.

Figure 5.14 compares the start and end gas temperatures of the MAX manifold case. As can be seen, iso-octane provides about on average 13℃ of cooling while ethanol provides about 17℃ cooling.

This, combined with the problems associated with controlling the gas temperatures, resulted in ethanol's end temperature being around 8℃ cooler than iso-octane's for the MAX manifold runs.

Figure 5.15 shows the comparison of the modelled gas temperatures between ethanol and iso-octane for the PRE case. Here the cooling provided by each of the two fuels does differ greatly, with ethanol cooling the gas by up to 80 ℃ while iso-octane cools the gas by around only 20 ℃.

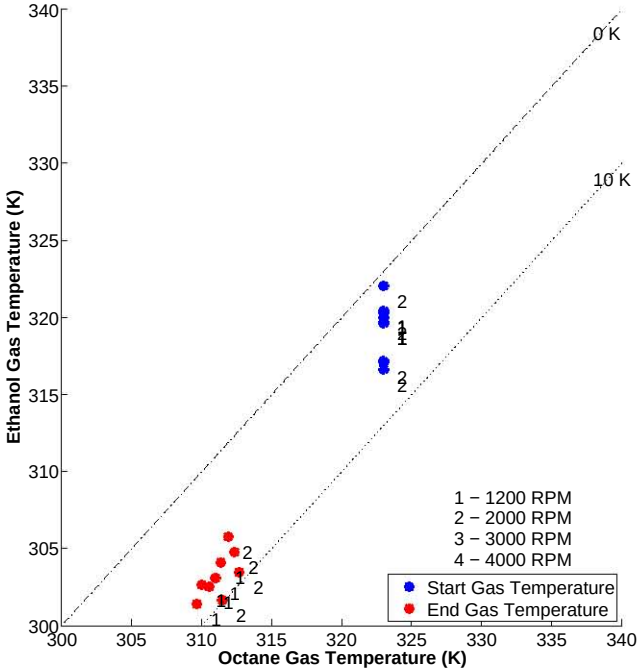

Figure 5.14: Ethanol versus iso-octane- MAX manifold modelled gas temperatures

It is evident that ethanol's end gas temperature is greater than iso-octane's by approximately 50 ℃ for the PRE manifold condition. This was caused by the difficulties in measuring the true gas temperature, as stated previously.

Insight into Charge Cooling

The modelling study highlighted the nature of charge cooling within a manifold and the difference of it between fuels.

Under the MAX conditions which were meant to promote evaporation, iso-octane was able to achieve a temperature drop of about 13℃ which is only about half of its 20℃ theoretical charge cooling capacity. Ethanol was only able to achieve cooling of about 17℃, which is a quarter of its theoretical charge cooling capacity.

Thus ethanol's much larger heat of vapourisation compared to iso-octane's was not taken full advantage of.

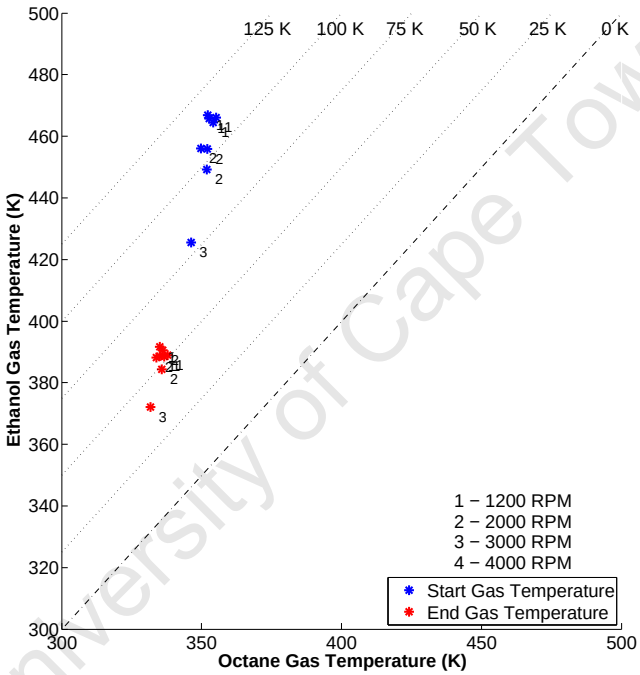

Figure 5.15: Ethanol versus iso-octane- PRE manifold modelled gas temperatures

Chapter 6

Engine Results and Discussion

The combustion data in terms of the Knock Limited Spark Advance (KLSA) and a K analysis are captured in this chapter. Following this are the results of the combustion and knock model, where the model is compared to the experimental data and its effectiveness in simulating this data in this regard is detailed.

6.1 Combustion Data

6.1.1 KLSA

The KLSA is used throughout this study as the indication of the knock resistance of the fuels, with a larger KLSA indicating a greater knock resistance.

It should be noted that the metric of KLSA is used to plot data against. In this study it is simply the spark timing with the sign inverted. That means that a spark timing of -20 CAD (or 20°BTDC) is thus represented as 20 CAD of KLSA. This was done as it was felt that the concept of knock resistance is best represented by a metric that increases with it.

Figure 6.1 immediately highlights the strong knock resistance of ethanol under the PFI conditions when compared to iso-octane and ULP 95. This figure shows two expected trends that were discussed in Chapter 2.1.2, namely that of greater overall knock resistance of all fuels at higher speeds and lower boosts, indicated by higher KLSAs.

There is a trend where the greater the octane sensitivity of the fuel, the flatter the plots. Thus the KLSA of ethanol, having the largest octane sensitivity, changes the least across the speeds while iso-octane, with the smallest sensitivity, changes the most. Thus the knock resistance of the sensitive fuels does not increase as much as the knock resistance of the non-sensitive fuels as speed increases. This can be attributed to the higher speed conditions operating in a region where the K value is more positive thus favouring low sensitivity fuels. This is as predicted by literature, as discussed in Chapter 2.3.

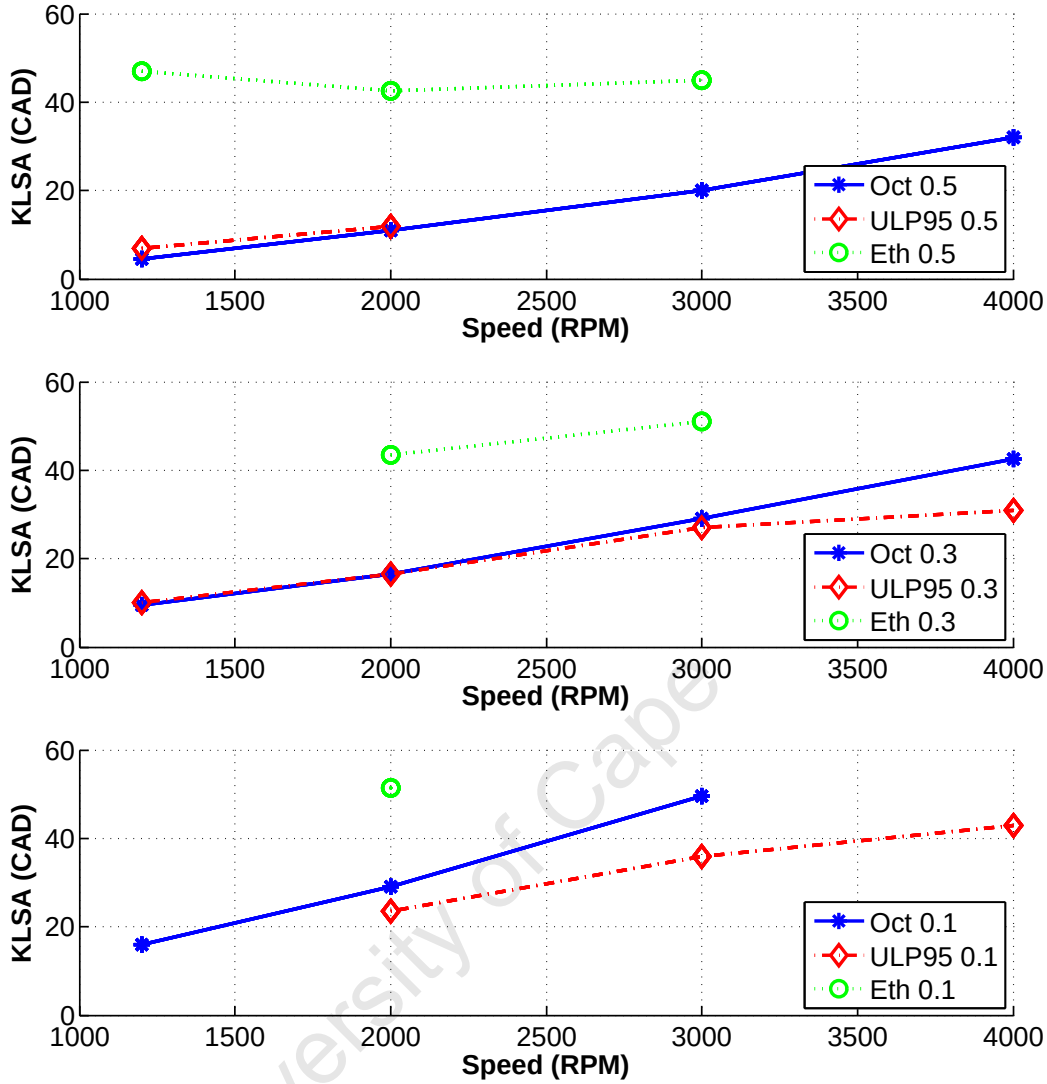

Figure 6.1: KLSA comparing fuels across boosts - PFI conditions (top figure - 0.5 bar boost, middle figure - 0.3 bar boost, bottom figure - 0.1 bar boost)

iso-Octane is seen to have superior KLSA compared with ULP 95 at the low boost of 0.1 bar. However at high boosts this superiority decreases, with the ULP 95 in fact marginally outperforming iso-octane under the 0.5 bar boost conditions. This is despite iso-octane having both higher RON and MON numbers than ULP 95 (iso-octane has a RON and MON of 100 compared to ULP 95 with a RON and MON of 95 and 85 respectively). This is in line with the previous discussion where higher sensitivity fuels such as ULP 95 will have improved relative knock resistance compared to low sensitivity fuels, such as iso-octane, under operating conditions that have more negative K values, such as higher boost conditions.

The data from the PFI case thus follows the trend of the high sensitivity fuels benefiting from operating conditions that are towards the negative K range whereas the low

sensitivity fuels prefer more positive K type conditions.

Comparison of the KLSA under the different manifold conditions can be seen in Figure 6.2 and 6.3 .

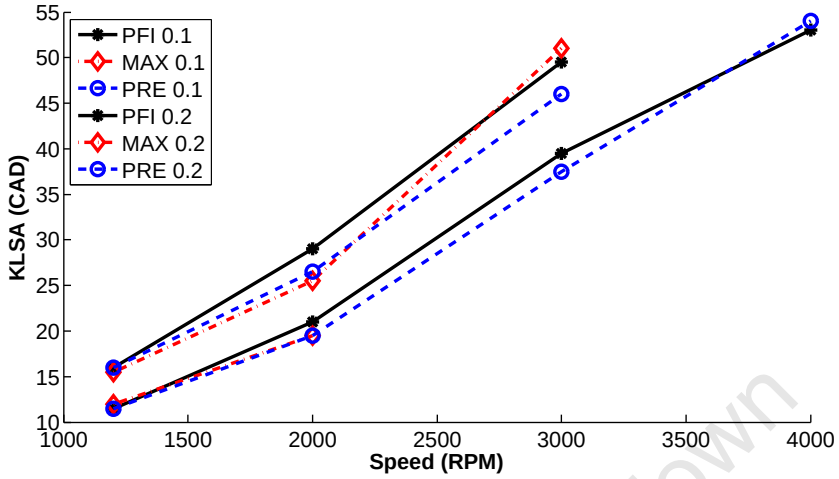

Figure 6.2: Comparison of KLSA for different manifold conditions for iso-octane

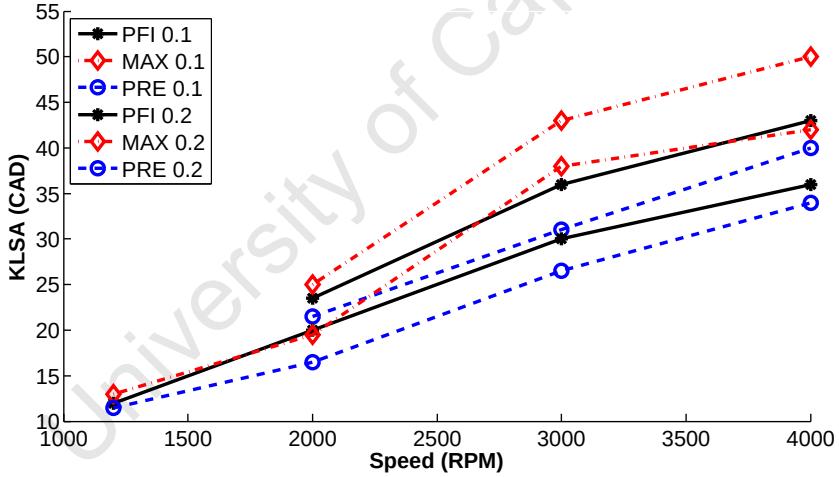

Figure 6.3: Comparison of KLSA for different manifold conditions for ULP 95

The ULP 95 runs produce the best KLSA under the MAX condition, then the PFI and then the PRE. This is expected, as the MAX condition allows for the greatest amount of cooling through evaporation, while the PRE case is heated, with PFI expected to be intermediate between the two cases.

iso-Octane however shows all three manifold cases to be very closely spaced, with PFI in fact having a small advantage, although too small for any overall inferences. It does indicate that iso-octane is less sensitive to temperature changes than ULP 95, which is in line with our knowledge of non-sensitive fuels such as iso-octane.

Figure 6.4 is a comparison plot to highlight the differences between ethanol and iso-octane's KLSAs and so their knock resistances. The plotted points are the KLSAs

at the various manifold conditions. The dotted lines indicate the difference in CAD between the points plotted on them. That is, the 20 CAD line indicates a difference of 20 CAD in KLSA between the two fuels. The numbers plotted next to the points indicate the engine speed of that point, that is 1 for 1200 RPM, 2 for 2000 RPM and so forth.

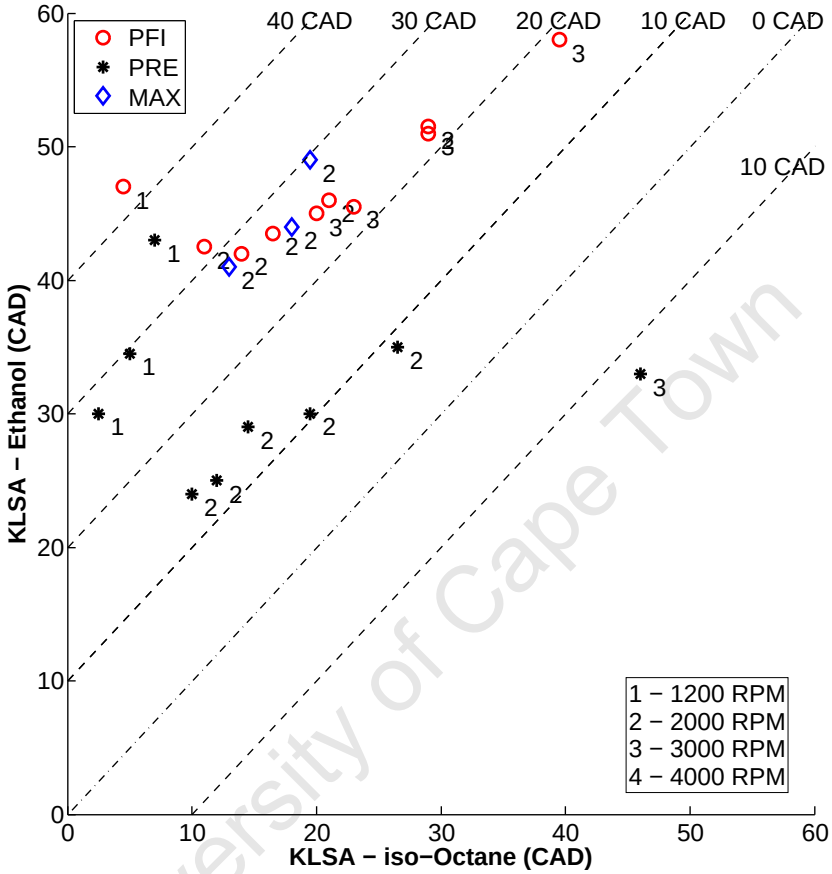

Figure 6.4: Comparison of ethanol versus iso-octane KLSA under equivalent conditions

The ethanol KLSA shows an advantage over the iso-octane runs of approximately 25 CAD at 2000 RPM and 20 CAD at 3000 RPM for the MAX and PFI runs, while showing for the PRE runs an approximately 30 CAD advantage at 1000 RPM and 10 CAD advantage at 2000 RPM.

The influence of the difference in starting temperature between the MAX and PRE cases should be noted. Ethanol has a high KLSA of approximately 25 CAD for the MAX but only 10 CAD for the PRE. This is both due to the differences in charge cooling and autoignition effects as well as the difference in inlet charge temperature by approximately 60℃, as discussed in the previous chapter.

The errant 3000 RPM PRE case is not considered as it appears to be an outlier and as mentioned previously is most likely a result of the noise issue with regards to the KL detection.

6.1.2 K Analysis

An analysis to determine the K value of the runs was conducted using the KLSA as the measure of knock resistance. The details of this type of analysis are described in Appendix B.6. The K analysis requires at least three data points and as such the sparse data prevented a K analysis being done for a number of the operating points.

Figures 6.5 and 6.6 show the results for the analyses. All manifold conditions show that the K value is seen to increase with an increase in speed as well as increase with a decrease in boost. These trends are as expected and follow the known theory, as discussed in Chapter 2.3.2.

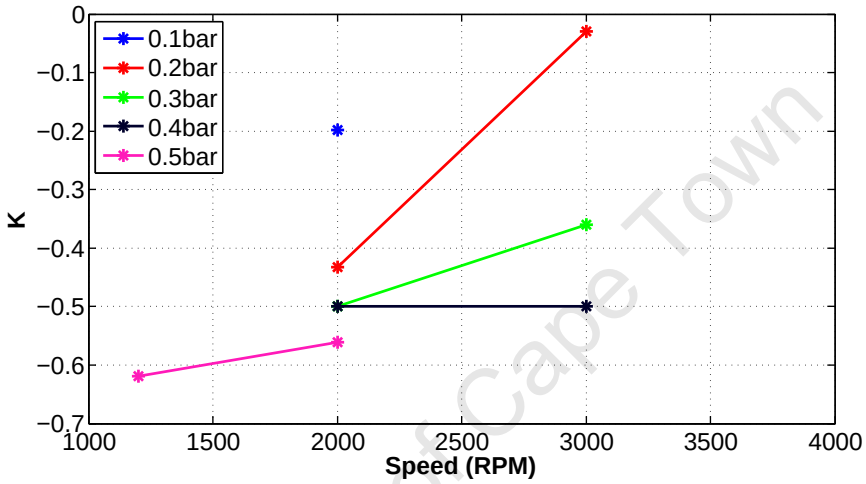

Figure 6.5: K values for PFI

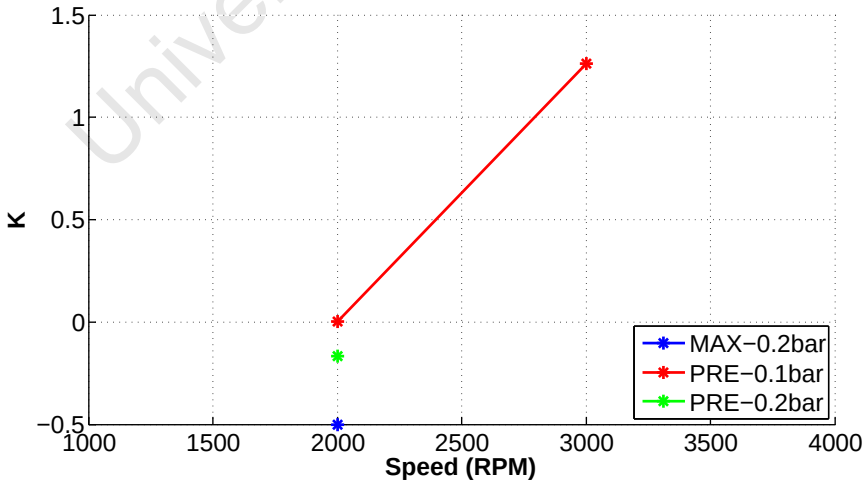

Figure 6.6: K values for MAX and PRE

The PFI cases are seen to operate in the negative K range. The MAX condition where a K analysis was able to be done also operates in the negative K range. The PRE case of 0.1 bar boost operates in the positive K range while the 0.2 bar boost case

is in the negative K range. This more positive K range is as a result of the increased starting temperature of the PRE manifold cases and follows the expected theory.

The analysis shows however that the experimental runs were operated almost entirely in the negative K regime as intended.

Figure 6.7 illustrates clearly the influence of the speed and boost on the K value under the PFI case, with K increasing with higher speed and lower boost.

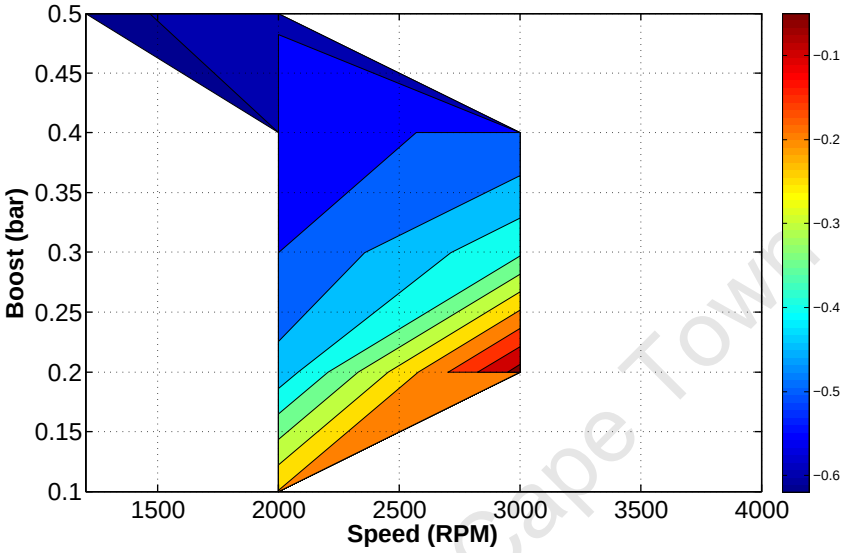

Figure 6.7: Contour plot to illustrate K value for PFI

6.2 Combustion Modelling

6.2.1 Input parameters of Model

The modelling of the engine data follows in this Chapter and is shown as a completed unit. However an iterative process was conducted to find the correct inputs required to effectively simulate the data. Table 6.1 and 6.2 details these inputs, which are discussed further below.

Table 6.1: Model characteristics for combustion data simulation

T_{wall}	solved from data
Wiebe Coefficients	solved from data
T_{IVC}	solved for model
Cool Flame Set point	0.95
Main Flame Set point	0.95

The wall temperature T_{wall}, from Equation 4.15, which serves as the representative heat transfer sink temperature for the modelled runs, was solved for using the method

Table 6.2: REG values used for combustion modelling

Speed (RPM)	1200	2000	3000	4000
REG (%)	0	5	20	20

noted in Swarts and Yates [84], where the temperature is taken as the cylinder temperature at the point where the polytropic coefficient curve and the specific heat ratio curve of the compression cycle cross over. Up until this point heat was being added to the system, thus the polytropic coefficient is larger than the specific heat ratio, while after this point heat is removed from the system.

The initial temperature at inlet valve closure, T_{IVC}, was solved for so that the model pressure at a reference point was equal to that of the data. The cylinder pressure 5 CAD prior to the knock point of the data was used as the reference point for solving.

The Livengood and Wu integral, Equation 2.3, was set to indicate knock at 0.95 rather than 1. This was felt justified as the model is unable to account for temperature gradients within the unburnt end gas and as such local hot spots would initiate knock sooner than predicted by the model. Yates et al. [10], using the same autoignition modelling approach as in this study, make use of a local temperature ”tuning” factor to account for temperature gradients within the CFR engine. The change of the Livengood and Wu integral set point was felt to achieve the same thing in an easier manner. This did prove to provide a slightly better Knock Onset (KO) fit.

The Wiebe coefficients, seen in Equation 4.14, were solved through the fitting of the Wiebe equation to the heat release profile. This was calculated from the pressure trace as described in Chapter B.4.

The Residual Exhaust Gas (REG) value, which determines the amount of REG at Inlet Valve Closure (IVC), was varied based on insight given by the breathing model (See Appendix F). While the breathing model struggled to simulate the dynamic nature of the breathing across the speed range, it did suggest that the REG value would increase with an increase in speed. The resulting REG values that were used, especially the 3000 and 4000 RPM values, were not linked though to the magnitudes suggested by the model due to this deficiency. The large difference between the REG values used across the speeds may indicate a shortcoming of the combustion and knock model. However, as the final simulated results, as detailed in the next chapter, were conducted on a comparison basis, it was felt that the final outcome of the study was not compromised as a result.

6.2.2 Non-knocking Combustion

A few non-knocking runs were captured to test the capabilities of the combustion model. Figure 6.8 shows an example of the fit achieved. The T_{IVC} was solved to get the same peak pressure in this instance.

The model reproduces the combustion event satisfactorily, except for the exhaust stroke. The exhaust stroke is modelled hotter than recorded. This is a result of the

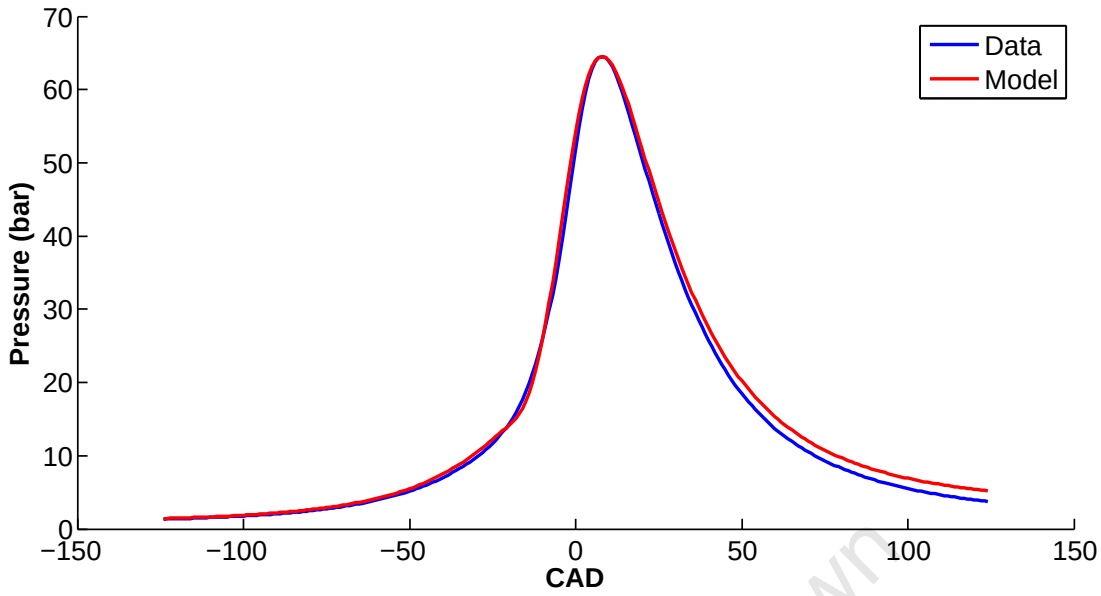

Figure 6.8: Combustion fit of non-knocking cycle, 2000 RPM, no boost, PFI

thermal shock experienced by the transducer, as discussed earlier, that lowers the pressure recorded during the exhaust stroke.

This poor exhaust stroke performance is not considered crucial, as the prediction of knock does not rely on the exhaust stroke data nor was the exhaust stroke used to infer the starting conditions of the model.

6.2.3 Knocking combustion

iso-Octane

Samples of the modelling of the knocking combustion of iso-octane under PFI conditions can be seen in Figure 6.9 and 6.10. The timing of the autoignition model's cool flame and main flame are also indicated on the plots.

The areas of interest are the compression and combustion process up until the knock point and the prediction of the knock point. At the point of knock all the remaining unburnt components were converted to burnt, thus causing the sharp pressure spike in the model at the knock point.

The model matches the data well up until the point of knock. Both figures show the knock being predicted to occur a few degrees ahead of the actual knock experienced in the engine, with the higher speed example performing better than the lower speed.

The data and model matching after the knock event is of no value to this work, especially considering the thermal shock that was found and would affect the exhaust pressure signal.

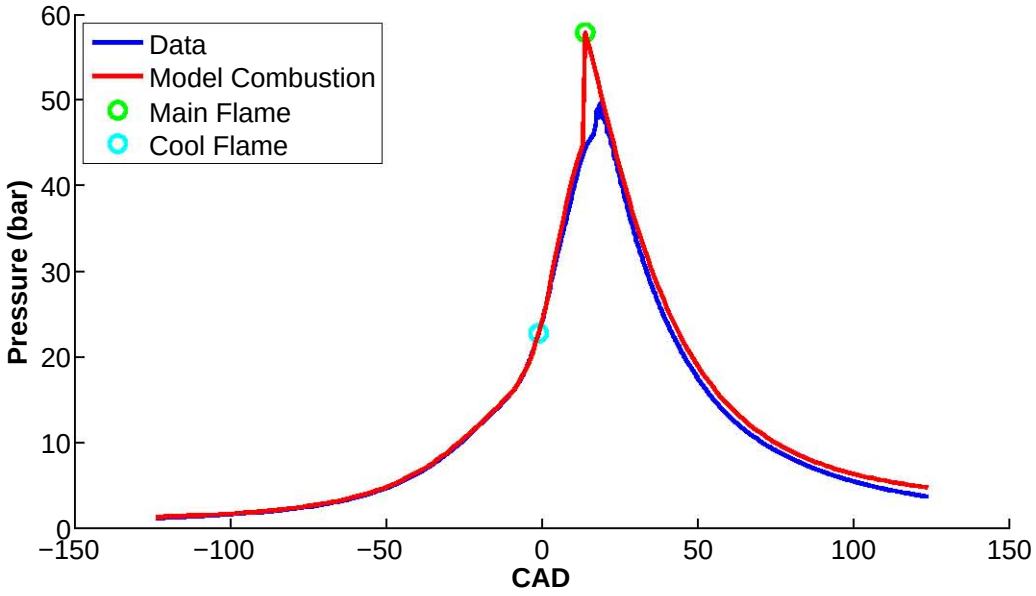

Figure 6.9: Model fit for single combustion event, 1200 RPM, 10 kPa, iso-octane PFI

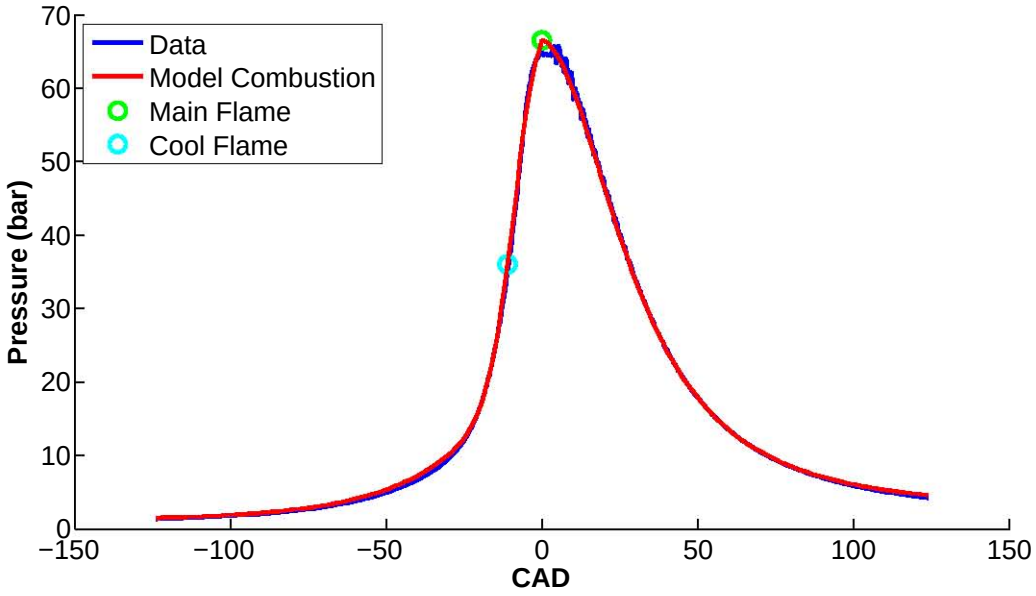

Figure 6.10: Model fit for single combustion event, 3000 RPM, 10 kPa, iso-octane PFI

Figure 6.11 shows the model when simulating an 'average' combustion event compared with the numerous engine cycles that make up a data point. This combustion model uses the average Wiebe coefficients and is compared to the averaged knock point CAD. The modelled combustion is shown to predict knock earlier than the data determined knock point.

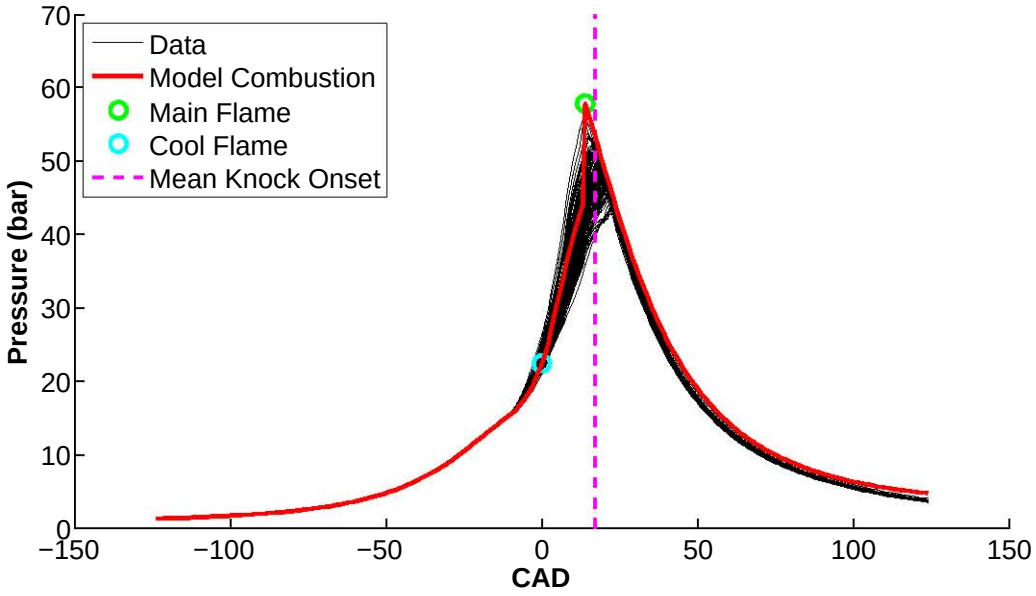

Figure 6.11: Model fit for averaged combustion event, 1200 RPM, 10 kPa, iso-octane PFI

Ethanol

Figures 6.12 and 6.13 show the comparisons of the modelled knocking combustion for ethanol in the PFI condition for a single combustion event and the averaged combustion event, as was done for iso-octane.

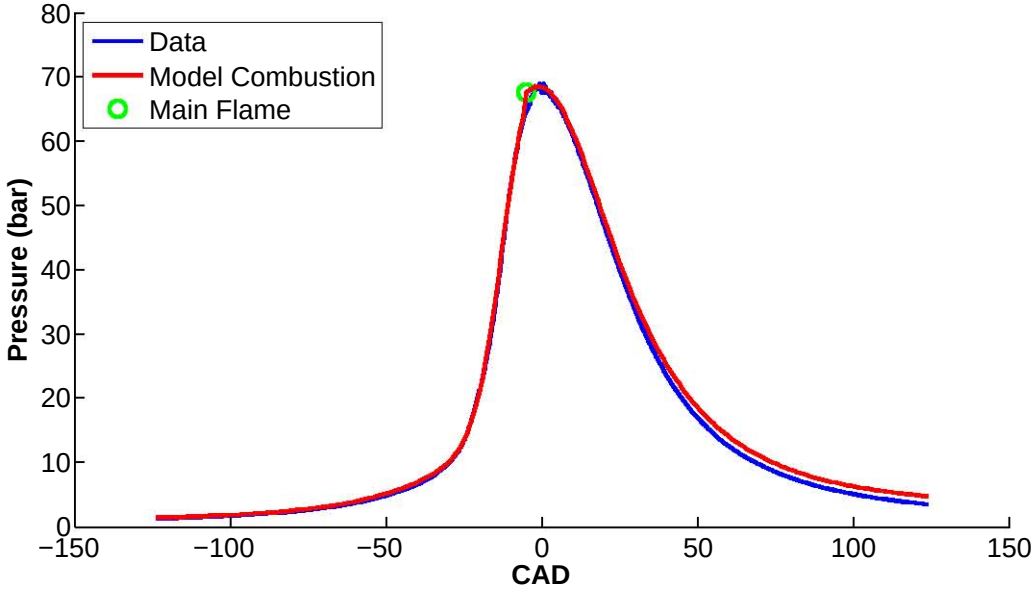

Figure 6.12: Model fit for single combustion event, ethanol 2000 RPM, 20 kPa , PFI

Once again the model matches well to the data up to the point of knock, with the knock

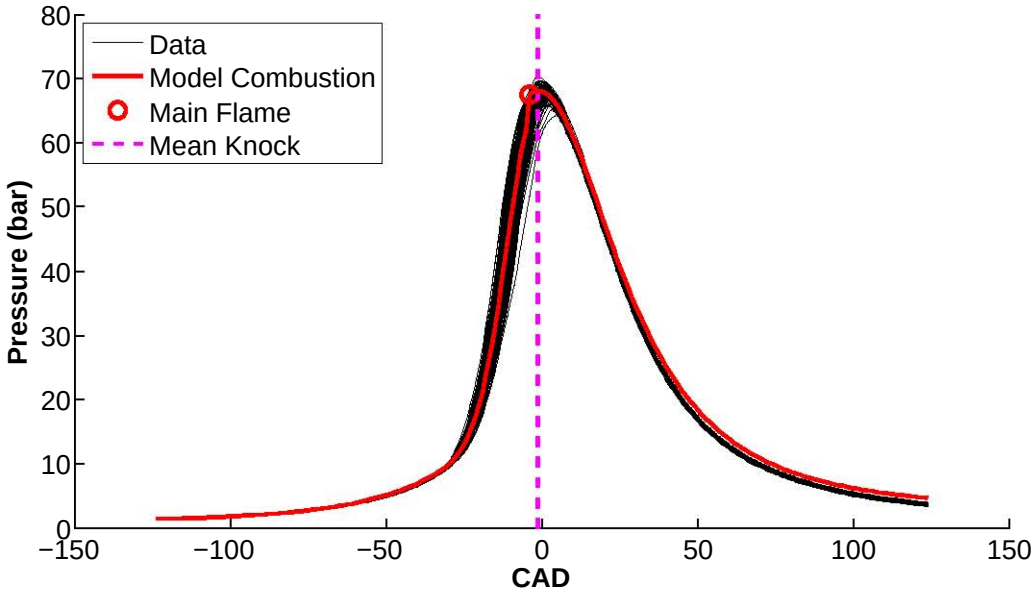

Figure 6.13: Model fit for averaged combustion event, 2000 RPM, 20 kPa, ethanol PFI

predicted to occur slightly earlier than expected.

Figure 6.14 shows a fit where the model fails to predict the knock event. The model's pressure trace matches the data trace well and ends with the tau integral on a value of 0.46 in this case. The model failed to predict knock on 4 of the successful ethanol runs, namely at 3000 RPM for 0.2, 0.3 and 0.4 bar boost for the PFI case and 3000 RPM 0.1 bar boost for the PRE case. All iso-octane runs had knock predicted.

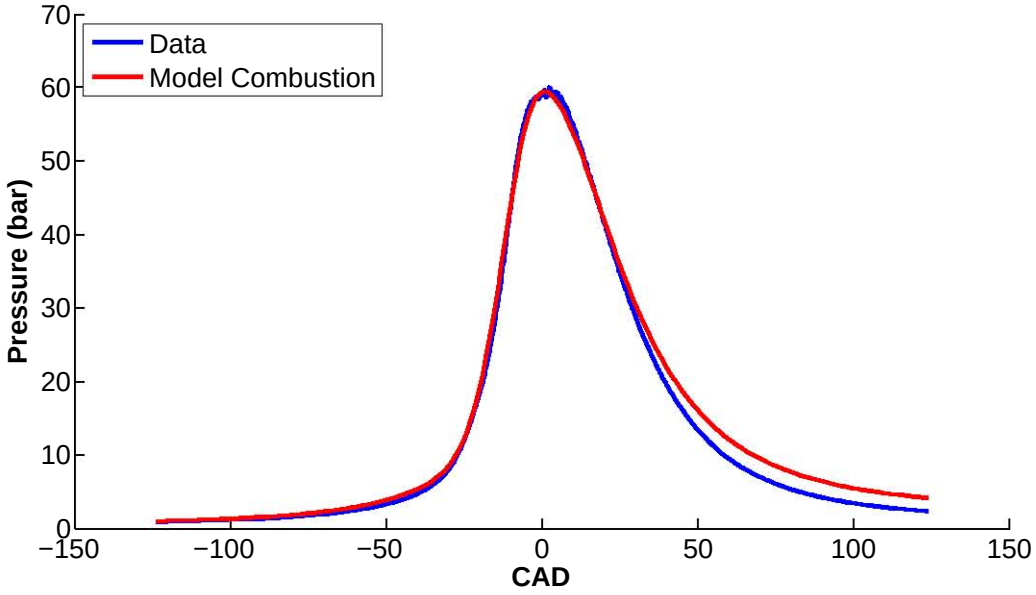

Figure 6.14: Model fit for single combustion ethanol, 3000 RPM, 20 kPa, PFI

These are the higher speed ethanol runs and as mentioned previously, noise on the

transducer signal was shown to influence the KL measurement. The knock detected experimentally may then be simply the noise present on the transducer. However, the magnitude of this influence is unknown and whether it occurs here is difficult to tell. This may also be caused by the model being tuned to more lower speed data, as there is sparse high speed ethanol data. While it coped satisfactorily with the iso-octane higher speed data, this though does not rule out the possibility that the model is particularly poor at high speed ethanol knock modelling.

Overall Data Fit

Figure 6.15 shows the comparison between the predicted and actual knock onset for the iso-octane runs. The majority of the runs have the model predicting the knock onset to within 5 CAD. The worst performing model runs are those with relatively early knock onsets (around the 5 CAD ATDC mark).

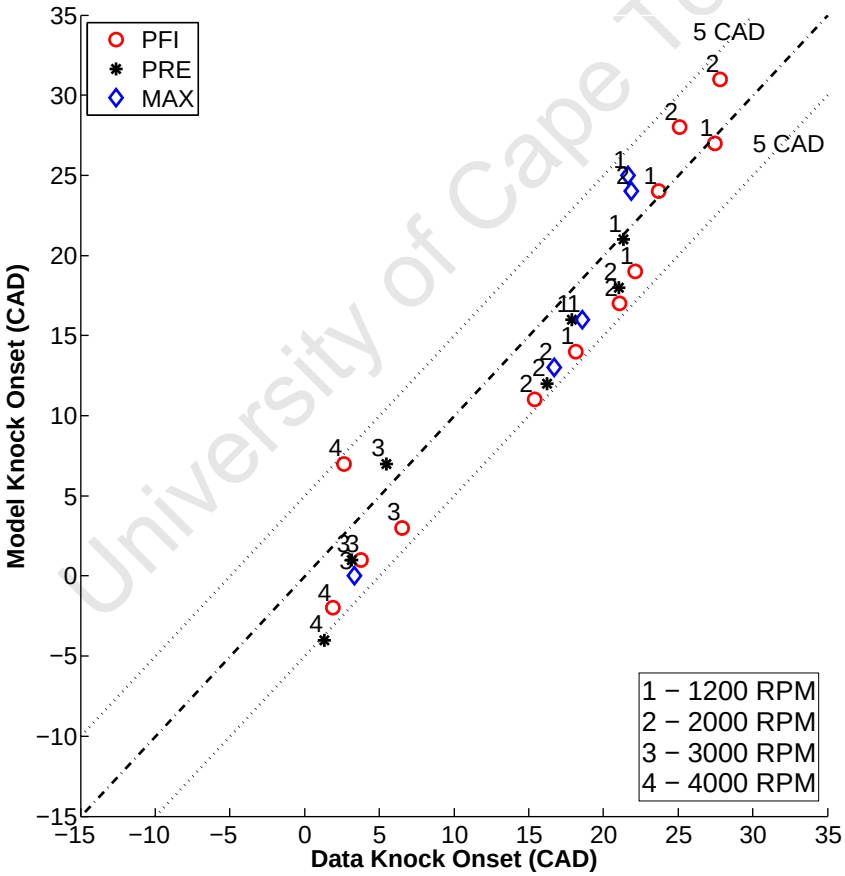

Figure 6.15: Comparison of predicted and measured knock onset - iso-octane

Figure 6.16 shows the comparison of the predicted and actual knock onset for the ethanol runs. Once again, the majority of the runs match to within 5 CAD, with the poorest performing prediction occurring again at the earlier knock onsets.

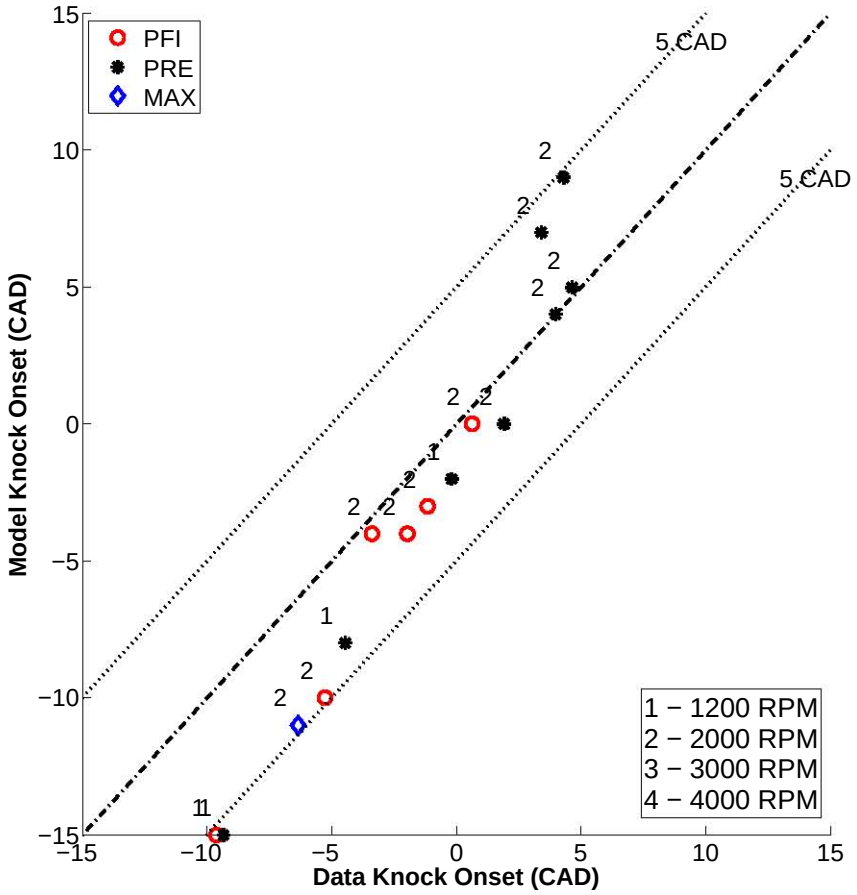

Figure 6.16: Comparison of predicted and measured knock onset - ethanol

These fits are considered to be satisfactory and will allow sufficient insight when conducting the simulated runs. This is especially so in light of the various setbacks the experimental data suffered, such as thermal shock and noise influences for the higher speeds.

Chapter 7

Simulated Results and Discussion

This chapter captures the results of the simulated runs, where an investigation into a number of influences that contribute to the knock resistance of iso-octane and ethanol is conducted. These fuels are used to represent the alcohol and traditional petrol fuels, with the goal to further understand the reason behind the improved performance of the alcohol fuels in Beyond RON conditions. The investigation focusses particularly on the charge cooling and autoignition chemistry influences, the two properties considered to have the greatest impact.

7.1 Overview

The greater knock resistance of ethanol compared to iso-octane under the Beyond RON conditions that the fuel was subjected to in the experimental runs was evident from the previous KLSA plots.

In order to determine the influence of autoignition chemistry and charge cooling in ethanol's greater knock resistance over iso-octane, the combustion and autoignition model was run under a number of configurations to gauge the influence of a number of factors.

The modelling was set up to mirror the experimental method used to quantify knock resistance through the use of KLSA.

7.2 Input Parameters of Model

The default input parameters used for the simulation are highlighted in Table 7.1 with the Wiebe coefficients given in Tables 7.2 and 7.3.

The wall temperature, T_{wall} and Wiebe coefficients were chosen from the fitting of the experimental data to provide representative conditions. The T_{IVC} was 500 K by default and varied in later studies. This value was chosen as it was in the range of the T_{IVC}'s

Table 7.1: Input parameters for simulated runs

T_{wall}	400 K
REG	5%
T_{IVC}	500 K
p_{IVC}	1.2 bar + boost
Knock Limit	2 bar

Table 7.2: Ethanol Wiebe coefficients for simulated runs

Speed (RPM)	1200	2000	3000	4000
$\Delta\theta$	40	53	56	56
b	6	9	13	13
m	3.5	4	5	5

Table 7.3: iso-Octane Wiebe coefficients for simulated runs

Speed (RPM)	1200	2000	3000	4000
$\Delta\theta$	47	55	60	62
b	5	7	12	13.5
m	2.5	3	5	5.5

that were solved for in the experimental modelling to match the pressure histories (discussed in Chapter 6.2.1).

The criteria for the KL to determine the KLSA was when the peak overpressure caused by the knock reached a limit of 2 bar. This is further discussed in the next section.

7.3 Knock Limit Determination

A method of determining the KL so that the KLSA could be solved for in these simulated runs was required. The method used in the modelling of the experimental runs was to set the spark advance to that of the run, solve for the temperature at inlet valve closure to ensure the pressure histories matched and then compare the resulting knock onsets of the model and experimental data.

The simulated runs however had a set input temperature and solved rather for the spark advance to a set KL, thus determining the KLSA.

Two choices for the model's KL criteria was thus investigated.

The first method was the use of the Livengood and Wu integral of the autoignition time, with the set point the same as that of the experimental runs, namely 0.95 (as described in Chapter 6.2.1).

The second method made use of the peak overpressure caused by the knock, directly imitating the KL used during experimentation. As the knock heat release is released

all in a space of a single CAD in the model, the limit would not be the same as that on the experimental runs. This limit was set to 2 bar after some inspection of the model's response. This method was not used in the experimental simulation due to the difficulty in determine the cylinder temperature at inlet valve closure accurately across a range of speeds.

To determine the suitability of these KLs, the iso-octane and ethanol models were both set up so that the only difference between them was the unburnt and burnt gas composition. Thus they had the same default initial conditions, REG value and cylinder wall temperature given in Table 7.1. Furthermore they were given the burn rates (i.e. Wiebe coefficients) and autoignition coefficients of ethanol.

The KLSA of these two models was then solved for, using each of the KL methods described in turn. Figure 7.1 shows the results of this.

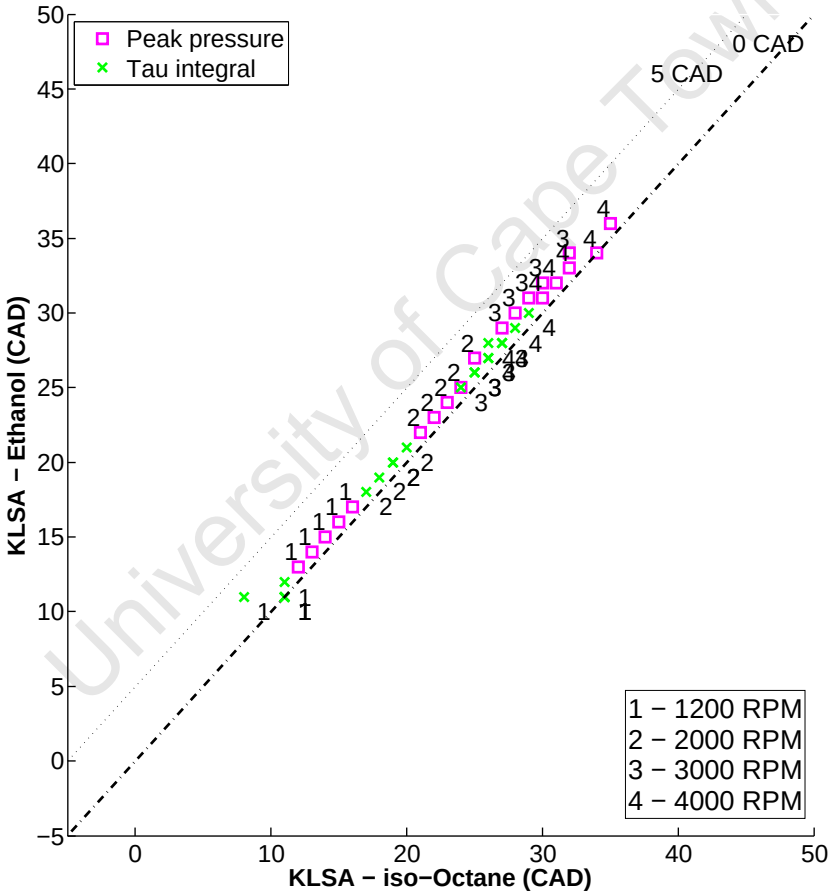

Figure 7.1: Comparison of influence of knock limit criteria on KLSA, with both models using ethanol autoignition chemistries and burn rates as well as the same initial conditions, REG values and wall temperature

As can be seen, the methods both produce KSLAs with only a slight advantage towards ethanol. However this was due to combustion temperature effects, which is investigated further in the next section.

As both KL criteria produced satisfactory results for the purpose of this study, namely that of comparing KLSAs between the fuels, the peak overpressure method was chosen. As the tau integral method would determine the KLSA at the very onset of knock, the peak overpressure method would allow for some advancement after that to reach the overpressure limit set. This better mirrored reality and produced KLSAs that were closer to those seen in experimentation.

7.4 Combustion Temperature

Ethanol has lower end gas temperatures than iso-octane, as discussed in Chapter 2.4. This is due to two contributing factors. Firstly, the composition of the combustion products of ethanol have a higher heat capacity and so produce lower burnt gas temperatures. Secondly, a stoichiometric mixture of ethanol and air has a 2% lower calorific value than that for iso-octane.

These cooler burnt gas temperature of ethanol result in lower unburnt gas temperatures through less compression of the unburnt end gas and less heat transfer into the unburnt end gas from the cylinder walls and burnt zone.

The influence of this was investigated through a comparison of knock resistance between two models were the only difference was the composition of the unburnt charge and burnt end products. This can be seen in Figure 7.1 using the peak pressure method (while both KL methods in Figure 7.1 illustrate the influence of the combustion temperature, the peak pressure method will be used further in this study and so only its results are discussed here).

Figure 7.1 shows that the cooler temperature of ethanol's end gas has minimal effect, resulting in a difference in the KLSA of about 1 CAD at the lower speeds and about 2 CAD at the higher speeds.

The difference in temperatures of the burnt zone and unburnt zone of ethanol and iso-octane can be seen in Figure 7.2. These runs were conducted with the same configurations as those discussed above, but with the spark timing not solved for. Rather they were both had the same spark timing and the autoignition models turned off. The difference in the maximum burnt zone temperatures is approximately 50 K, caused by the difference in the burnt product composition. However this only translates into a difference of approximately 8 K in the unburnt gas and so only a small difference in knock resistance and thus KLSA.

It should be noted for these runs where higher burnt gas temperatures are produced for iso-octane, the model heats the unburnt end gas through greater compression by the hotter burnt gas and the increased heat transfer to the unburnt end gas due to the higher average cylinder temperature (see Equation 4.15). The model does not account for interzonal heat transfer between the burnt and unburnt zone and may thus under predict the unburnt end gas temperature and so the full effect of the higher combustion temperatures of iso-octane.

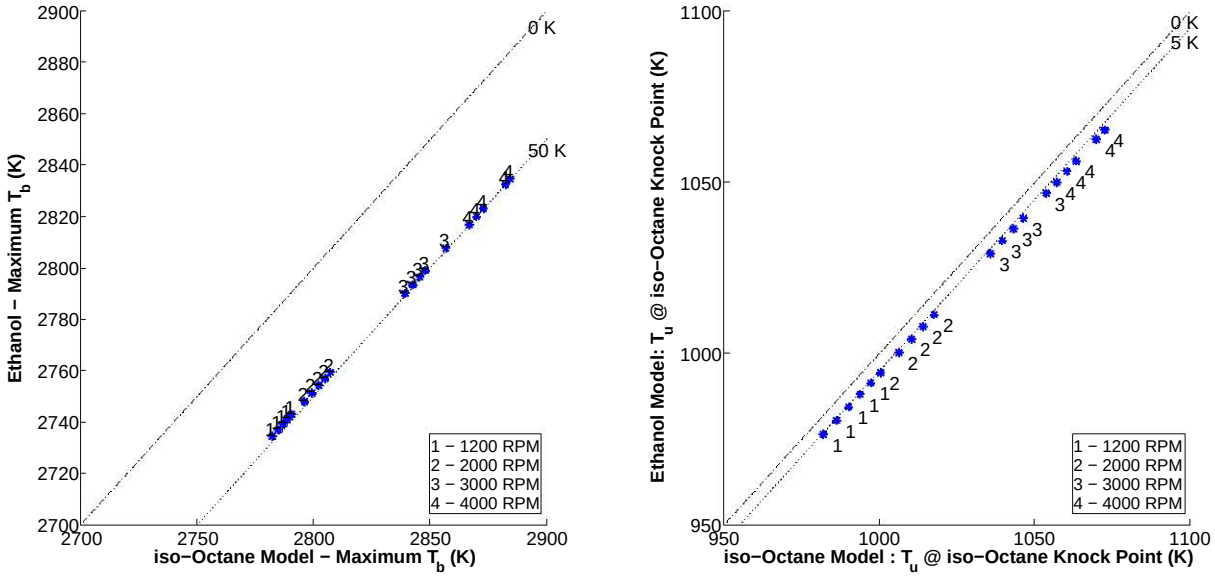

(a) Maximum burnt temperatures

(b) Unburnt charge temperature at knock point

Figure 7.2: Illustration of differences between ethanol's and iso-octane's maximum burnt and unburnt charge temperatures

7.5 Burn Rate

The influence of the differences in burn rate between the two fuels was investigated through the comparison of the Wiebe coefficients influence. Ethanol has a faster burn rate than iso-octane, with a smaller burn duration ($\Delta\theta$) of approximately 5 CAD.

The two models were set-up with all variables except the gas compositions the same, as in Chapter 7.4, but now with the Wiebe coefficients also different for each fuel.

Figure 7.3 shows the influence that the difference in Wiebe coefficients has on the KLSA between ethanol and iso-octane. The Wiebe coefficients used are given in Table 7.2 and 7.3 and are determined from the experimental work with the method described in Chapter 4.3.2.

Looking at the KLSA determined with constant Wiebe values from Figure 7.3 and comparing it to KLSA difference of Figure 7.1, the 2000 RPM KLSA can be seen to have been increased in ethanol's favour by approximately 2 CAD while the rest of the speeds are increased in iso-octane's favour by approximately 2 CAD.

The slower burn rate of iso-octane would be expected to give it some advantage in the KLSA as it naturally retards the peak pressure. The counter performance of the 2000 RPM is most probably a modelling influence, caused by the Wiebe coefficients determined by the fitting of the data. The difference between the 2000 RPM $\Delta\theta$'s is the smallest of the speeds, while the difference in the b coefficients is the largest of the speeds, as seen in Tables 7.2 and 7.3.

In an attempt to capture the changing nature of the Wiebe coefficients, functions that related the value of the specific coefficient to the KLSA were investigated. Figure

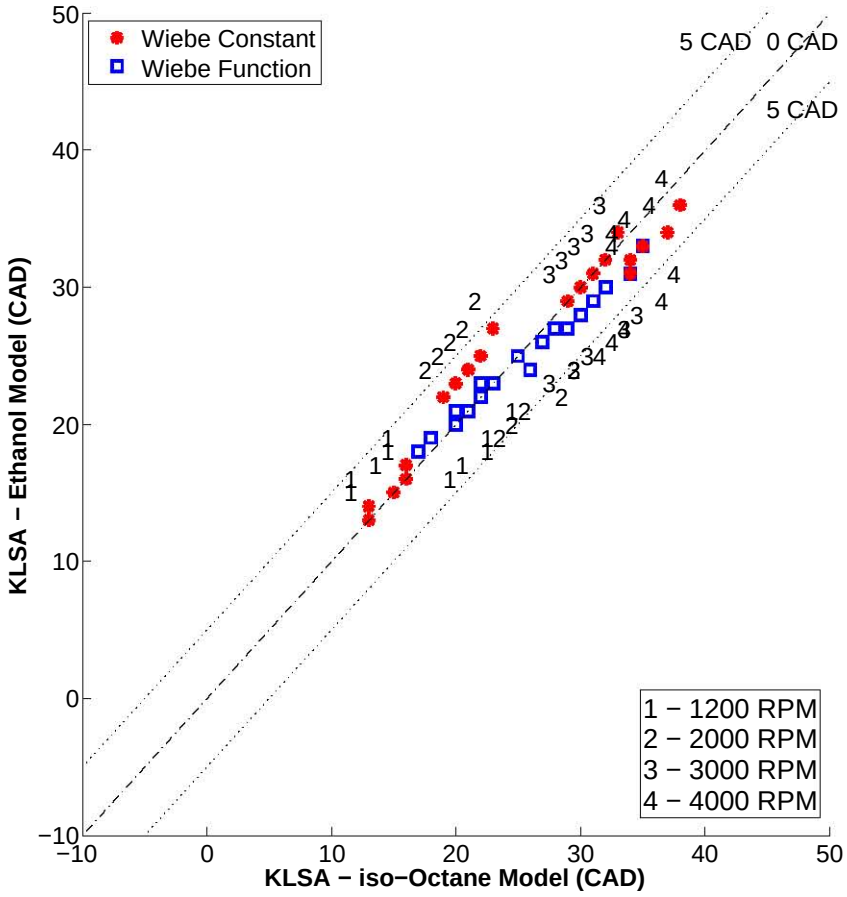

Figure 7.3: Ethanol vs iso-octane KLSA - comparison of burn rate influence

7.3 shows that the functions resulted in no change in difference between the fuels, but did compact the KLSA's together. It was decided though to continue using the constant Wiebe values, as this would then maintain a constant difference between the two fuels and their burn rates, which would thus ease the complexity of studying the differences between the KLSA's as the cooling and autoignition chemistry influence was the priority.

7.6 Varied REG

The influence of the Residual Exhaust Gas (REG) values that were used in the modelling study of the experimental runs was investigated. These values vary with speed and are shown in Table 7.4. Thus, while in the previous investigations of combustion and burn rate influences (Chapter 7.4 and 7.5 respectively) a constant REG value of 5% was used for both fuel models, the models were now both run with the REG values different across the speeds, just as they were in the modelling of the experimental runs.

Table 7.4: REG values used for combustion modelling

Speed (RPM)	1200	2000	3000	4000
REG (%)	0	5	20	20

This thus compared the reaction of KLSA of the two models to each other when the REG value varies across the speeds for both models.

These runs were conducted with the same inputs as those in Section 7.4, but with the REG values varying across the engine speeds. Thus they both have the autoignition chemistry and burn rates of ethanol.

Figure 7.4 shows the results of the runs, which show that there was no comparative change in the KLSA of the two fuels after giving both fuels the REG values of Table 7.4. That little difference that is visible in the KLSA is caused by the difference in end gas temperatures, as Figure 7.1 shows the same differences.

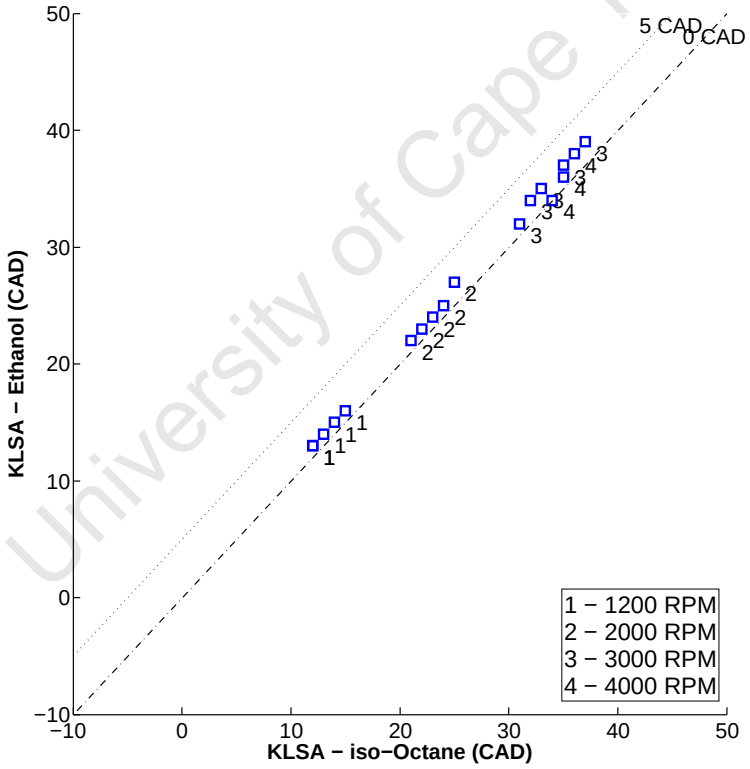

Figure 7.4: Ethanol vs iso-octane KLSA - Comparison of the models comparative KLSA reaction to a varied REG value across speeds, with both models using the same REG values

It should be noted that the autoignition model used, that of Yates et al. [10], does not make provision for the direct influence of REG on autoignition delay. Thus the influence seen of REG on the absolute values of the KLSA is through the lowering of the peak

combustion pressures and temperatures. However this influence is seen to be simliar for both fuels and thus has little influence on the comparative KLSAs of the fuels.

The constant value of 5% across the speeds was thus kept.

7.7 Autoignition Chemistry

Figure 7.5 illustrates the effect that the autoignition chemistry of the two fuels has on their knock resistance and how this influence changes at different starting temperatures. The two models were run with the same starting conditions and wall temperature. The models have their own burn rates, gas compositions and autoignition chemistry.

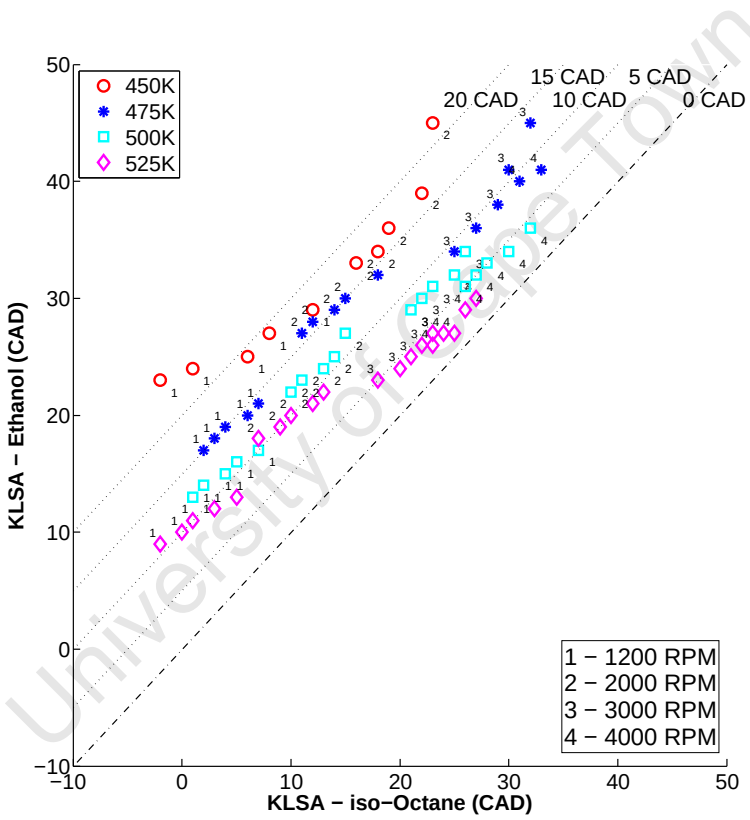

Figure 7.5: Ethanol vs iso-octane KLSA - comparison of autoignition chemistry influence

Ethanol's autoignition chemistry gives it a greater KLSA of approximately 15 CAD at a T_{IVC} of 475 K, approximately 10 CAD at 500 K and approximately 7 CAD at 525 K. This advantage is much larger than the previously mentioned differences that were investigated and discussed. This illustrates the large advantage that ethanol's autoignition chemistry gives it over iso-octane under these conditions.

The advantage ethanol has over iso-octane is shown to be reduced at higher starting temperatures. This agrees with the already discussed improved performance of

non-sensitive fuels like iso-octane under more positive K conditions, which a higher T_{IVC} represents.

However no improvement in performance of iso-octane relative to ethanol is seen with an increase in speed, which also represents more positive K conditions. This is because the model uses the same p_{IVC} and T_{IVC} across the speeds. This eliminates the influence that differences in starting conditions across the speeds would have.

Particularly we would expect the higher speeds to have higher temperatures due to less time for charge cooling, as seen in the inlet manifold modelling in Figure 5.13. This would improves iso-octane's performance relative to ethanol, as discussed above.

The reason for the improved performance of iso-octane at higher temperatures is due to the diminishing influence of the cool flame as temperatures increase. Figure 7.6 shows the comparison of ethanol and iso-octane KLSA with a T_{IVC} of 500 K with the cool flame on and off. This was achieved by only using the $\tau_{h,i}$ of the iso-octane autoignition model. See Chapter 2.6 and [40] for details on the autoignition model. iso-Octane has a far more comparable KLSA compared to ethanol without the cool flame. This also shows that the engine operating regime is within the influence of iso-octane's cool flame.

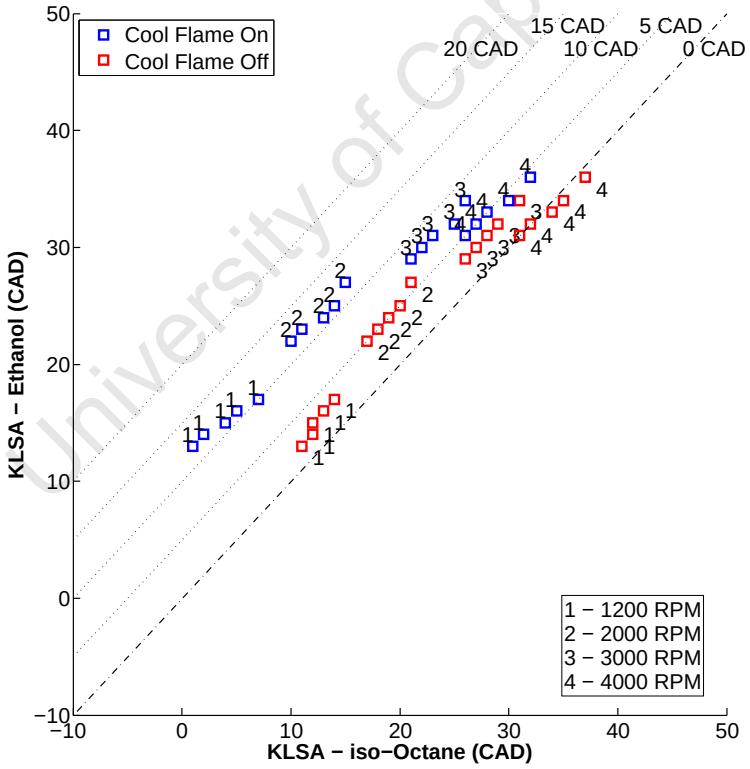

Figure 7.6: Ethanol vs iso-octane KLSA - comparison of cool flame's influence

Figure 7.7 further illustrates the influence of the cool flame on the knock resistance of the two fuels. The upper plot shows a pressure-temperature plot of the combustion

history up until knock with the T_{IVC} of 475 K, showing that ethanol knocks at a far higher pressure and temperature than iso-octane.

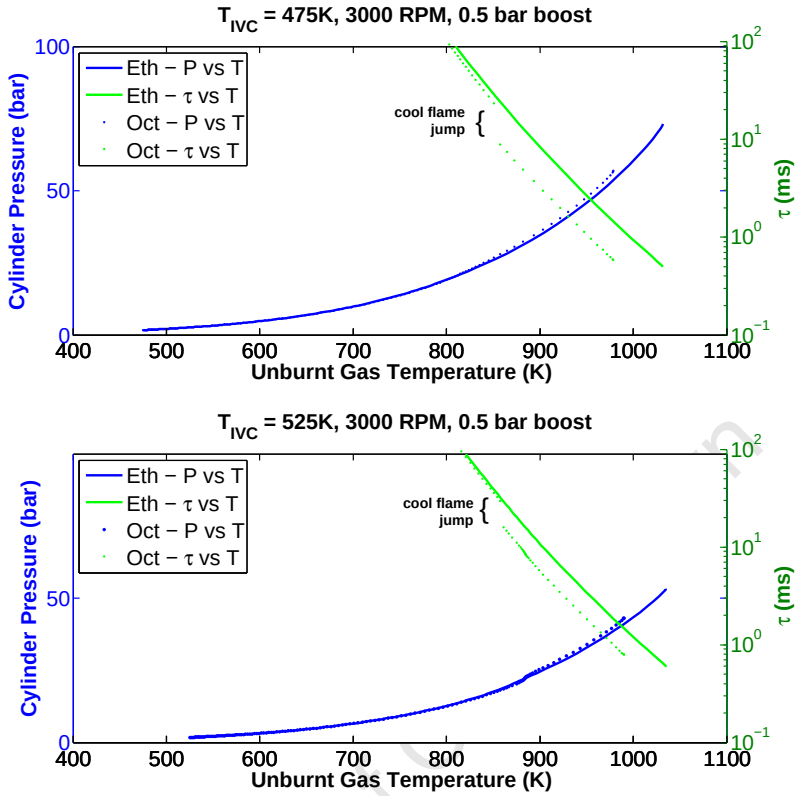

Figure 7.7: Illustration of cool flame influence on autoignition chemistry

The absolute value of the autoignition time at each point as predicted by the autoignition model is plotted against the temperature on the second axis. This value must not be confused with the integral used to predict knock when it reaches a cumulative value of 1, which sums the inverse of this autoignition time that is plotted here. Instead it is the absolute autoignition time in milliseconds at that specific temperature and pressure. It clearly shows that at the same temperature, ethanol has a far higher autoignition time, which allows it to reach the higher temperature and pressure and thus have the greater KLSA.

The iso-octane autoignition time is shown to experience a sudden drop. This is the cool flame of the model activating, which significantly lowers the autoignition time. This drop in autoignition time thus significantly accelerates the autoignition process. This is particularly apparent when comparing the plot of the iso-octane autoignition time and the ethanol autoignition time and how close the two plots are until the cool flame makes the iso-octane autoignition time jump to a much smaller value than the ethanol plot, especially considering the autoignition time scale shown in Figure 7.7 is a log scale.

The lower plot shows the same details but for a run with a T_{IVC} of 525 K. Here the iso-octane is able to have a KLSA and an end pressure and temperature that is closer

to that of the ethanol. This can be attributed to the lower influence of the cool flame caused by higher initial temperatures.

This influence of cool flame dynamics can thus be extended to the comparison of other single stage fuels and two stage fuels. The two stage fuels would thus always be expected to improve their knock resistance compared to single stage fuels when operating under hotter conditions.

7.8 Differential Cooling

The influence of differences in cooling of the inlet charge between the fuels was investigated. To illustrate the potential increase in knock resistance that could be brought about by making greater use of ethanol's charge cooling capacity, the KLSA of iso-octane was compared to ethanol's with ethanol having a lower T_{IVC}. A difference in T_{IVC} of 25 K was chosen for illustrative purposes. This value in particular allowed for the use of the data from the previous section for this comparison.

The results of this comparison are shown in Figure 7.8, with ethanol having a lower T_{IVC} of 25 K in each case.

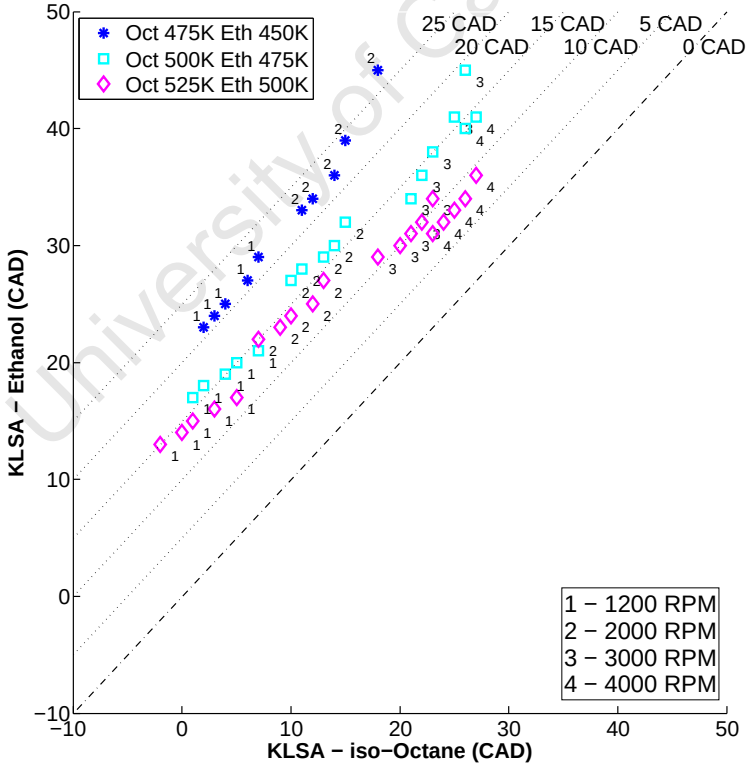

Figure 7.8: Ethanol vs iso-octane KLSA - comparison of differential cooling influence

By comparing Figure 7.5 and 7.8 is can be seen that when the T_{IVC} of ethanol is less than iso-octane's by 25 K, ethanol's KLSA improves relative to iso-octane's

by approximately 5 CAD compared to the KLSA for equal T_{IVC}. This is thus an improvement above that which autoignition chemistry already afforded ethanol.

However it was shown that a difference in starting temperature of 25 K was not achieved in this study through evaporation. While ethanol's heat of vapourisation is sufficiently larger than iso-octane's to allow for this magnitude of difference in starting temperatures, it was not practically achievable. The difference in temperatures between the fuels was instead in the range of 5 K, as discussed in Chapter 5.2.5.

This highlights thus that the differential cooling played a small role in ethanol's knock resistance advantage over iso-octane.

Ethanol however has a theoretical capacity to cool the charge by 85℃ while iso-octane has a capacity to cool it by 21℃ [83]. In an engine where more of ethanol's charge cooling capacity can be realised, this difference of 64℃ could provide ethanol with a knock resistance advantage over iso-octane that is comparable with its autoignition chemistry advantage.

Additionally, this would result in cooler operating temperatures, which is where ethanol's autoignition chemistry has the largest advantage over iso-octane due to iso-octane's reduced knock resistance caused by the increased influence of the cool flame under these operating conditions.

DI engines may allow for this greater cooling difference. This thus highlights DIs ability compared to PFI in taking advantage of all of ethanol's knock resistance potential, as already extensively documented in literature.

The simulated results show how the greater amount of charge cooling that could be achieved through the use of DI engine technology would improve ethanol's knock resistance over iso-octane's, above the advantage its autoignition chemistry already provides it.

Firstly the greater charge cooling that ethanol would be able to achieve compared to iso-octane would result in lower operating temperatures and thus greater knock resistance.

Secondly, the cooler operating temperatures due to the greater charge cooling would further advantage ethanol as its autoignition chemistry has a greater advantage over iso-octane at lower operating temperatures. This is, as already discusses, due to the cool flame influence for iso-octane at lower temperatures accelerating autoignition.

7.9 Simulated Results Review

The modelling study conducted shows the weak influence of burn rate, residual exhaust gas fractions and combustion temperature differences on the relative difference in knock resistances between ethanol and iso-octane.

The autoignition chemistry plays the largest role in the difference in knock resistance between the two fuels. The advantage was shown to be, in terms of KLSA, in the range of 7 to 15 CAD, depending on the starting temperature.

This advantage over iso-octane varies due to iso-octane's cool flame influence. At lower temperatures, the cool flame accelerates the autoignition process of iso-octane, giving ethanol a larger advantage. At higher temperatures the cool flame influence diminishes, reducing ethanol's advantage over iso-octane.

The influence of charge cooling was investigated and it was shown that if ethanol has a temperature less than iso-octane's at inlet valve closure of 25 K this translates into a KLSA advantage of approximately 5 CAD, over and above the advantage already gained through autoignition chemistry.

However this large a temperature difference was not realised in this study, with a difference in the range of 5 K only obtained through evaporation. Thus the influence of the differential cooling is small compared to the autoignition chemistry.

The autoignition chemistry thus dominated the charge cooling influence in ethanol's larger knock resistance.

Ethanol does however have the theoretical capacity to cool the charge by up to 85℃ compared to iso-octane's 21℃. This difference of 64℃ could give ethanol a further advantage over iso-octane that is of similar magnitude to that of its autoignition chemistry. It would further also cause cooler operating conditions, which is where ethanol has the greatest autoignition chemistry advantage over iso-octane. Engine technology such as DI may be able make use of this potential advantage.

Chapter 8

Conclusions

Following the discussion of the results of this study, a number of conclusion can be drawn:

- The use of the thermocouples to measure temperature in two phase flow is fraught with difficulty and at best provides order of magnitude readings.
- The measurement of knock under Beyond RON conditions requires engine systems specifically designed to handle the stresses that this type of investigation puts the engine and its instrumentation under.
- The inlet manifold modelling showed that ethanol only achieved a small portion of its full charge air cooling capacity. The modelling showed that ethanol cooled the inlet charge along the manifold by only about 4℃ more than iso-octane, despite the large differences in latent heat of vapourisation. This ineffective evaporation highlights the potential that exists for increasing ethanol's knock resistance through greater charge air cooling. Technologies such as Direct Injection (DI) may be able to take fuller advantage of the cooling potential ethanol offers.
- In an engine that can cause a larger differential in cooling between the fuels, such as DI, the simulated runs showed that when ethanol is 25 ℃ cooler than iso-octane, an improvement of 5 Crank Angle Degrees (CAD) is seen in the Knock Limited Spark Advance (KLSA), above that advantage that autoignition chemistry already gives ethanol.
- The overall contribution to the difference in knock resistances of ethanol compared to iso-octane was shown to be dominated by the differences in autoignition chemistry of the fuels. The magnitude of this difference is influenced by the overall operating temperatures, as cooler temperatures increase the advantage ethanol has.
- Cooler operating conditions result in a larger advantage for ethanol over iso-octane. These colder conditions are typical of Beyond RON conditions and this improved ethanol performance has been widely documented in literature. The model showed that this improved performance relative to iso-octane is

because of the increased influence of the cool flame phenomenon of iso-octane under cooler conditions, where the cool flame speeds up autoignition.

- Ethanol far outperforms iso-octane under Beyond RON conditions in terms of KLSA and thus knock resistance. This offers significant advantage for future engines that operate on ethanol under these conditions. Furthermore, there is the additional advantage to be gained from engine designs that are specifically configured to maximise the charge cooling advantage that ethanol can provide.

Chapter 9

Recommendations

The study conducted has raised a number of points to consider when conducting further research in this field:

- The measurement of the temperatures along the inlet manifold experienced was far from conclusive. Other methods will have to be investigated and implemented if more accurate measurements or further research on this matter is required.
- This study focused on Port Fuel Injected (PFI) and made use of the MAX inlet manifold case to provide readings comparable to Direct Injection (DI). However the cooling of the inlet charge between the fuels was very similar. This study conducted on a actual DI engine is recommended to more accurately capture the influence of the charge cooling and autoignition chemistry on the knock resistance of the fuels. Particularly the influence of injecting the fuel into a higher temperature conditions which would allow for the expected greater cooling that ethanol can provide.
- The effects of Residual Exhaust Gas (REG) and volumetric efficiency were not investigated in this study and as such their influence still requires quantification. This is both in terms of their influence on the operating environment as well as REG's direct influence on the autoignition chemistry. A different autoignition model may be better suited to an investigation of this type.
- A more conclusive study on speed's influence is required. This study's lack of data across the speeds hindered the insight that could be gained concerning these conditions.

References

[1] M. Chernoby, D. Hermance, J. Moulton, M. Oge, J. Smyth, and J. Botti, "Hybrids vs. diesel vs. modified gasoline, the near term : Is it time for a reality check?," in *Panel Discussion, SAE World Congress*, 2005.

[2] W. Attard, S. Konidaris, E. Toulson, and H. Watson, "The feasibility of downsizing a 1.25-liter normally aspirated engine to an 0.43-liter highly turbocharged engine," *SAE 2007-24-0083*, 2007.

[3] J. Turner, R. Pearson, B. Holland, and R. Peck, "Alcohol-based fuels in high performance engines," *SAE 2007-01-0056*, 2007.

[4] K. Nakata, S. Utsumi, A. Ota, K. Kawatake, T. Kawai, and T. Tsunooka, "The effect of ethanol fuel on a spark ignition engine," *SAE 2006-01-3380*, 2006.

[5] P. Kapus, A. Fuerhapter, H. Fuchs, and G. Fraidl, "Ethanol direct injection on turbocharged SI engines - potential and challenges," *SAE 2007-01-1408*, 2007.

[6] M. J. Brusstar and C. L. Gray, "High efficiency with future alcohol fuels in a stoichiometric medium duty spark ignition engine," *SAE 2007-01-3993*, 2007.

[7] S. Brewster, "Initial development of a turbo-charged direct injection E100 combustion system," *SAE 2007-01-3625*, 2007.

[8] J. B. Heywood, *Internal Combustion Engine Fundamentals*. McGraw-Hill, 1988.

[9] R. J. Nates and A. D. B. Yates, "Knock damage mechanisms in spark-ignition engines," *SAE 942064*, 1994.

[10] A. D. B. Yates, A. Bell, and A. Swarts, "Insights relating to the autoignition characteristics of alcohol fuels," *Fuel*, vol. 89, pp. 83–93, 2010.

[11] A. Swarts, *Insight Relating to Octane Rating and the Underlying Role of Autoignition*. PhD thesis, University of Cape Town, 2006.

[12] ASTM, "Standard test method for Research Octane Number of a spark-ignition engine fuel.ASTM Designation (D 2699-01a)," October 2001.

[13] ASTM, "Standard test method for Motor Octane Number of a spark-ignition engine fuel. ASTM designation (D 2700-01a);," October 2001.

[14] A. Thiart, G. Floweday, and C. Meyer, "A CFD study of fuel evaporation and related thermo-fluid dynamics in the inlet manifold, port and cylinder of the CFR octane engine," *SAE 2012-01-1715*, 2012.

[15] M. Rothe, T. Heidenreich, U. Spicher, and A. Schubert, “Knock behavior of SI engines: Thermodynamic analysis of knock onset locations and knock intensities,” *SAE 2006-01-0225*, 2006.

[16] G. T. Kalghatgi, “Fuel anti-knock quality - part I: Engine studies,” *SAE 2001-01-3584*, 2001.

[17] V. Mittal and J. B. Heywood, “The relevance of fuel RON and MON to knock onset in modern SI engines,” *SAE 2008-01-2414*, 2008.

[18] W. Attard, *Small engine performance limits-turbocharging, combustion or design*. PhD thesis, University of Melbourne, Department of Mechanical and Manufacturing Engineering, 2007.

[19] H. Hiereth and P. Prenninger, *Charging the internal combustion engine*. Springer Verlag, 2007.

[20] Y. Ohyama, T. Nogi, and M. Ohsuga, “Effects of fuel/air mixture preparation on fuel consumption and exhaust emission in a spark ignition engine,” *IMechE Paper*, pp. 59–64, 1992.

[21] F. Zhao, M. Lai, and D. Harrington, “A review of mixture preparation and combustion control strategies for spark-ignited direct-injection gasoline engines,” *SAE 970627*, 1997.

[22] F. Zhao, D. Harrington, and M. Lai, “The spray characteristics of automotive port fuel injection: a critical review,” *SAE 950506*, 1995.

[23] F. Zhao, M. Lai, and D. Harrington, “Automotive spark-ignited direct-injection gasoline engines,” *Progress in energy and combustion science*, vol. 25, no. 5, pp. 437–562, 1999.

[24] C. Marriott, M. Wiles, and B. Rouse, “Development, implementation, and validation of a fuel impingement model for direct injected fuels with high enthalpy of vaporization,” *SAE 2009-01-0306*, 2009.

[25] R. Anderson, J. Yang, D. Brehob, J. Vallance, and R. Whiteaker, “Understanding the thermodynamics of direct-injection spark-ignition (DISI) combustion systems: an analytical and experimental investigation,” *SAE 962018*, 1996.

[26] L. Wyszynski, C. Stone, and G. Kalghatgi, “The volumetric efficiency of direct and port injection gasoline engines with different fuels,” *SAE 2002-01-0839*, 2002.

[27] J. Szybist, M. Foster, W. Moore, K. Confer, A. Youngquist, and R. Wagner, “Investigation of Knock Limited Compression Ratio of Ethanol Gasoline Blends,” *SAE 2010-01-0619*, 2010.

[28] G. T. Kalghatgi, K. Nakata, and K. Mogi, “Octane appetite studies in direct injection spark ignition (DISI) engines,” *SAE 2005-01-0244*, 2005.

[29] G. Kalghatgi, “Auto-ignition quality of practical fuels and implication for fuel requirements of future SI and HCCI engines,” *SAE 2005-01-0239*, 2005.

[30] G. Kalghatgi, “Fuel anti-knock quality-part II: Vehicle studies-how relevant is Motor Octane Number (MON) in modern engines?,” *SAE 2001-01-3585*, 2001.

[31] T. Beer, T. Grant, H. Watson, and D. Olaru, “Life-cycle emissions analysis of fuels for light vehicles,” *Atmospheric Research Report HA93A-C837/1 F*, vol. 5, 2004.

[32] D. Petitjean, L. Bernardini, C. Middlemass, and S. Shahed, “Advanced gasoline engine turbocharging technology for fuel economy improvements,” *SAE 2004-01-0988*, 2004.

[33] R. Wicker, F. Jasso, F. Medina, and G. Villa, “Practical considerations for an E85 fueled vehicle conversion,” *SAE 1999-01-3517*, 1999.

[34] I. Pielecha, D. Maslennikov, and K. Wislocki, “Optical research of spray development of E85 fuel in high pressure gasoline direct injection system,” *SAE 2010-01-2285*, 2010.

[35] I. Hunwartzen, “Modification of CFR test engine unit to determine octane numbers of pure alcohols and gasoline-alcohol blends,” *SAE 820002*, 1982.

[36] A. Boretti, “Advanced design of pure ethanol engines,” *SAE 2010-01-1453*, 2010.

[37] A. D. B. Yates, A. Swarts, and C. L. Viljoen, “Correlating auto-ignition delays and knock limited spark advance data for different types of fuel,” *SAE 2005-01-2083*, 2005.

[38] W. Leppard, “The chemical origin of fuel octane sensitivity,” *SAE 902137*, 1990.

[39] A. Cavaliere and M. de Joannon, “Mild combustion,” *Progress in Energy and Combustion Science*, vol. 30, no. 4, pp. 329–366, 2004.

[40] A. D. B. Yates and C. L. Viljoen, “An improved empirical model for describing auto-ignition,” *SAE 2008-01-1629*, 2008.

[41] V. Mittal, J. Heywood, and W. Green, “The underlying physics and chemistry behind fuel sensitivity,” *SAE 2010-01-0617*, 2010.

[42] D. P. Moran and A. Taylor, “An evaporative and engine-cycle model for fuel octane sensitivity prediction,” *SAE 952524*, 1995.

[43] D. Moran, “The effects of fuel evaporation on engine knock,” Master’s thesis, Master’s Thesis , University of Cape Town, 1993.

[44] D. Moran, “A numerical and experimental study of intake system fuel evaporation of methanol-gasoline blended fuels,” *SAE 941879*, 1994.

[45] J. Milpied, N. Jeuland, G. Plassat, S. Guichaous, N. Dioc, A. Marchal, and P. Schmelzle, “Impact of fuel properties on the performances and knock behaviour of a downsized turbocharged DI SI engine - focus on octane numbers and latent heat of vaporization,” *SAE 2009-01-0324*, 2009.

[46] J. C. Livengood and P. C. Wu, "Correlation of autoignition phenomena in internal combustion engines and rapid compression machines," in *Symposium Int. On combustion (8th)*, p. 347, 1955.

[47] A. Douaud, P. Eyzat, and S. of Automotive Engineers, *Four-octane-number method for predicting the anti-knock behavior of fuels and engines*. Society of Automotive Engineers, 1978.

[48] G. Floweday, "A new functional global auto-ignition model for hydrocarbon fuels-part 2 of 2: Model formulation, development and performance assessment," *SAE 2010-01-2169*, 2010.

[49] Y. Cengel and M. Boles, *Thermodynamics: an engineering approach*. McGraw-Hill Higher Education New York, 2006.

[50] Faculty of Science: The Chinese University of Hong Kong, "Microscopic interpretation of evaporation." [Online]. Available: http://www.phy.cuhk.edu.hk/contextual/heat/cha/evapo/evaporation_e.gif [Accessed July 21, 2011] .

[51] W. Sirignano and C. Edwards, *Fluid dynamics and transport of droplets and sprays*, vol. 122. Cambridge University Press, 2000.

[52] L. Bayvel and Z. Orzechowski, *Liquid atomization*. CRC, 1993.

[53] C. Brown and N. Ladommatos, "A numerical study of fuel evaporation and transportation in the intake manifold of a port-injected spark-ignition engine," *ARCHIVE: Proceedings of the Institution of Mechanical Engineers, Part D: Journal of Automobile Engineering 1989-1996 (vols 203-210)*, vol. 205, no. 34, pp. 161–175, 1991.

[54] C. Chen, D. Amlee, R. Johns, and Y. Zeng, "Detailed modeling of liquid fuel sprays in one-dimensional gas flow simulation," *SAE 2004-01-3000*, vol. 113, no. 3, p. 1604, 2004.

[55] E. Curtis, C. Aquino, D. Trumpy, and G. Davis, "A new port and cylinder wall wetting model to predict transient air/fuel excursions in a port fuel injected engine," *SAE 961186*, 1996.

[56] P. Rosin and E. Rammler, "The laws governing the fineness of powdered coal," *J. Inst. Fuel*, vol. 7, no. 31, pp. 29–36, 1933.

[57] D. Trayser, U. S. E. P. A. O. of Air Programs, and B. M. I. C. Laboratories, *A Study of the Influence of fuel Atomization, Vaporization, and Mixing Processes on Pollutant Emissions from Motor-Vehicle Powerplants*. Battelle, Columbus Laboratories, 1972.

[58] H. Baehr and K. Stephan, *Heat and Mass Transfer*. Berlin: Springer, 1998.

[59] J. Welty, C. Wicks, G. Rorrer, and R. Wilson, *Fundamentals of momentum, heat, and mass transfer*. John Wiley & Sons, Inc, 2001.

[60] R. S. Miller, K. Harstad, and J. Bellan, "Evaluation of equilibrium and non-equilibrium evaporation models for many-droplet gas-liquid flow simulations," *International Journal of Multiphase Flow*, vol. 24, no. 6, pp. 1025 – 1055, 1998.

[61] D. Spalding, *Combustion and mass transfer*. Pergamon, 1979.

[62] W. Ranz and W. Marshall, "Evaporation from drops," *Chem. Eng. Prog*, vol. 48, no. 3, pp. 141–146, 1952.

[63] M. Locatelli, C. Onder, and H. Geering, "An easily tunable wall-wetting model for PFI engines," *SAE 2001-01-1461*, 2004.

[64] G. D' Errico and A. Onorati, "An integrated simulation model for the prediction of GDI engine cylinder emissions and exhaust after-treatment system performance," *SAE 2004-01-0043*, 2004.

[65] B. Milton and M. Behnia, "A numerical study of the interchanging vapour, droplet and film flows in IC engine manifolds," *Heat and Mass Transfer in Engines, Hemisphere Publications*, pp. 245–258, 1989.

[66] C. Crowe, M. Sommerfeld, and Y. Tsuji, *Multiphase flows with droplets and particles*. CRC, 1998.

[67] B. Abramzon and W. Sirignano, "Droplet vaporization model for spray combustion calculations," *International journal of heat and mass transfer*, vol. 32, no. 9, pp. 1605–1618, 1989.

[68] G. Woschni, "A universally applicable equation for the instantaneous heat transfer coefficient in the internal combustion engine," *SAE 670931*, 1967.

[69] D. Boam and I. Finlay, "A computer model of fuel evaporation in the intake system of a carburetted petrol engine," in *I. Mech. E. Conf. on the Fuel Economy and Emissions of Lean Burn Engines*, vol. 89, p. 79, National Engineering Laboratory, Glasgow, 1979.

[70] K. Choi and H. Lee, "Experimental studies on the dynamics and evaporation of tandem liquid droplets in a hot gas flow," *International journal of heat and mass transfer*, vol. 35, no. 11, pp. 2921–2929, 1992.

[71] S. Friedlander and H. Johnstone, "Deposition of suspended particles from turbulent gas streams," *Industrial & Engineering Chemistry*, vol. 49, no. 7, pp. 1151–1156, 1957.

[72] R. Bird, W. Stewart, and E. Lightfoot, *Transport Phenomena*. New York: Wiley, 2nd ed., 2002.

[73] www.tdiclub.com, "Air temp after intercooler," 2002. [Online]. Available: http://forums.tdiclub.com/showthread.php?p=71317 [Accessed February 10, 2011] .

[74] evolutionm.net, "Ambient - post-intercooler temps," 2007. [Online]. Available: http://forums.evolutionm.net/evo-engine-turbo-drivetrain/260689-ambient-post-intercooler-temps.html [Accessed February 10, 2011].

[75] S. Jaffa, “Implementation of a fully variable valve actuation valvetrain,” Master’s thesis, University of Cape Town, 2011.

[76] Cape Advanced Engineering. [Online]. Available: http://www.cae.co.za/engineering/automation_cae_overview.html [Accessed March 20, 2011] .

[77] [Online]. Available: https://www.avl.com/indicom-indicating-software [Accessed Feb 26, 2013].

[78] A. Daif, M. Bouaziz, X. Chesneau, and A. A. Cherif, “Comparison of multicomponent fuel droplet vaporization experiments in forced convection with the sirignano model,” *Experimental Thermal and Fluid Science*, vol. 18, no. 4, pp. 282 – 290, 1998.

[79] Course Slides, “MEC 5082Z :Engine thermodynamics and combustion,” 2010.

[80] J. Borg and A. Alkidas, “On the application of Wiebe functions to simulate normal and knocking spark-ignition combustion,” *International Journal of Vehicle Design*, vol. 49, no. 1, pp. 52–69, 2009.

[81] Y. Yeliana, C. Cooney, J. Worm, D. Michalek, and J. Naber, “Estimation of double-wiebe function parameters using least square method for burn durations of ethanol-gasoline blends in spark ignition engine over variable compression ratios and egr levels,” *Applied Thermal Engineering*, vol. In Press, Corrected Proof, pp. –, 2011.

[82] M. Perumal, “A multi-zone model of the CFR engine: Investigating cascading autoignition and octane rating,” Master’s thesis, University of Cape Town, 2011.

[83] C. Taylor, *Internal Combustion Engine in Theory and Practice: Combustion, Fuels, Materials, Design*, vol. 2. MIT press, 1985.

[84] A. Swarts and A. Yates, “In-cylinder fuel evaporation and heat transfer information inferred from the polytropic character of the compression stroke in a spark-ignition engine,” *SAE 2004-01-1856*, 2004.

[85] D. Lancaster, R. Kireger, and J. Lienesch, “Measurement and analysis of engine pressure data,” *SAE 750026*, 1975.

[86] AVL List GmBH, “Engine indicating user handbook.” Graz AVL List GmBH, 2002.

[87] NGK Spark Plugs. [Online]. Available: http://www.ngksparkplugs.com/tech_support/spark_plugs/p3.asp?mode=nml [Accessed March 20, 2011] .

[88] L. Hamilton, M. Rostedt, P. Caton, and J. Cowart, “Pre-ignition characteristics of ethanol and E85 in a spark ignition engine,” *SAE 2008-01-0321*, no. 1, 2009.

[89] S. Lee, C. Bae, R. Prucka, G. Fernandes, Z. Filipi, and D. Assanis, “Quantification of thermal shock in a piezoelectric pressure transducer,” *SAE 2005-01-2092*, 2005.

[90] E. Rosseel, R. Sierens, and R. Baert, “Evaluating piezo-electric transducer response to thermal shock from in-cylinder pressure data,” *SAE 1999-01-0935*, 1999.

[91] D. Soltis, “Evaluation of cylinder pressure transducer accuracy based upon mounting style, heat shields, and watercooling,” *SAE 2005-01-3750*, 2005.

[92] A. Randolph, “Cylinder-pressure-transducer mounting techniques to maximize data accuracy,” *SAE 900171*, 1990.

[93] A. Higuma, T. Suzuki, M. Yoshida, Y. Oguri, *et al.*, “Improvement of error in piezoelectric pressure transducer,” *SAE 1999-01-0207*, 1999.

[94] Malvern Instruments, “Laser diffraction particle sizing,” 2011. [Online]. Available: http://www.malvern.com/LabEng/technology/laser_diffraction/particle_sizing.htm [Accessed September 29, 2011] .

[95] Malvern Instruments, “Using Mie theory and the Fraunhofer approximation,” 2011. [Online]. Available: http://www.malvern.com/LabEng/technology/laser_diffraction/mie_theory_fraunhofer.htm [Accessed September 29, 2011] .

[96] M. Miller and C. Nightingale, “Measurement of the changes in mixture preparation that occur during flow past the inlet valve of a spark-ignition engine,” in *International Conference Automotive Power Systems, Environment and Conservation: 10-12 September 1990, Chester College, Chester*, no. C394/004, p. 157, Dept of Mech Eng , University College, London, 1990.

[97] H. Lenz, G. Fraidl, and H. Friedl, “Fuel atomization with mixture preparation systems of SI engines,” *SAE 885015*, 1988.

[98] Malvern Instruments, “Spraytech application note: Measuring sprays containing propellants or volatile components,” tech. rep. [Online]. Available: http://www.malvern.com/malvern/kbase.nsf/allbyno/KB001250/$file/MRK881-01.pdf [Accessed September 29, 2011] .

[99] E. Cossali and Y. Hardalupas, “Comparison between laser diffraction and phase doppler velocimeter techniques in high turbidity, small diameter sprays,” *Experiments in fluids*, vol. 13, no. 6, pp. 414–422, 1992.

[100] H. Hiroyasu, M. Arai, and M. Tabata, “Empirical equations for the sauter mean diameter of a diesel spray,” *SAE 890464*, 1989.

[101] M. W. Chase Jr., ed., *NIST-JANAF Thermochemical Tables*, Gaithersburg, MD: National Institute of Science and Technology, 4th Ed., 1998.

[102] T. Daubert, R. Danner, H. Sibul, and C. Stebbins, *Physical and thermodynamic properties of pure chemicals: data compilation*. Taylor and Francis London, 1997.

[103] L. P. GmbH, “Landolt-bornstein substance / property index,” August 2009. [Online]. Available: http://lb.chemie.uni-hamburg.de/search/index.php [Accessed January 2011] .

Appendices

Appendix A

Inlet Manifold Design

The inlet manifold was designed to achieve three main goals.

These goals were to allow for the:

- the heating of the inlet air
- the upstream injection of fuel
- the recording of pertinent data in the manifold, with temperature measurement the primary objective.

These characteristics were required to allow for the separation of the charge cooling effect from the autoignition influence on the knock resistance of the fuels used in the study. This was to meet the objectives of the experimental study, as described in Chapter 3.1.

Figure A.1 shows a schematic of the inlet manifold, while Figure A.2 shows the completed manifold in place on the engine.

Heating of Inlet Air

The inlet air heating would have to provide sufficient heating to allow for the full evaporation of the fuel to fulfil the PRE manifold operating conditions, whose goal was to fully evaporate the fuel.

A 3-phase 12 kW heater was selected during the initial phases of the study to meet all possible heating requirements. This was during the phase of the investigation when methanol , together with the engine's maximum operation speed of 5400 RPM and a bar of boost were still being considered as possible experimental set points. Thus the heater was well within the eventual experimental requirements.

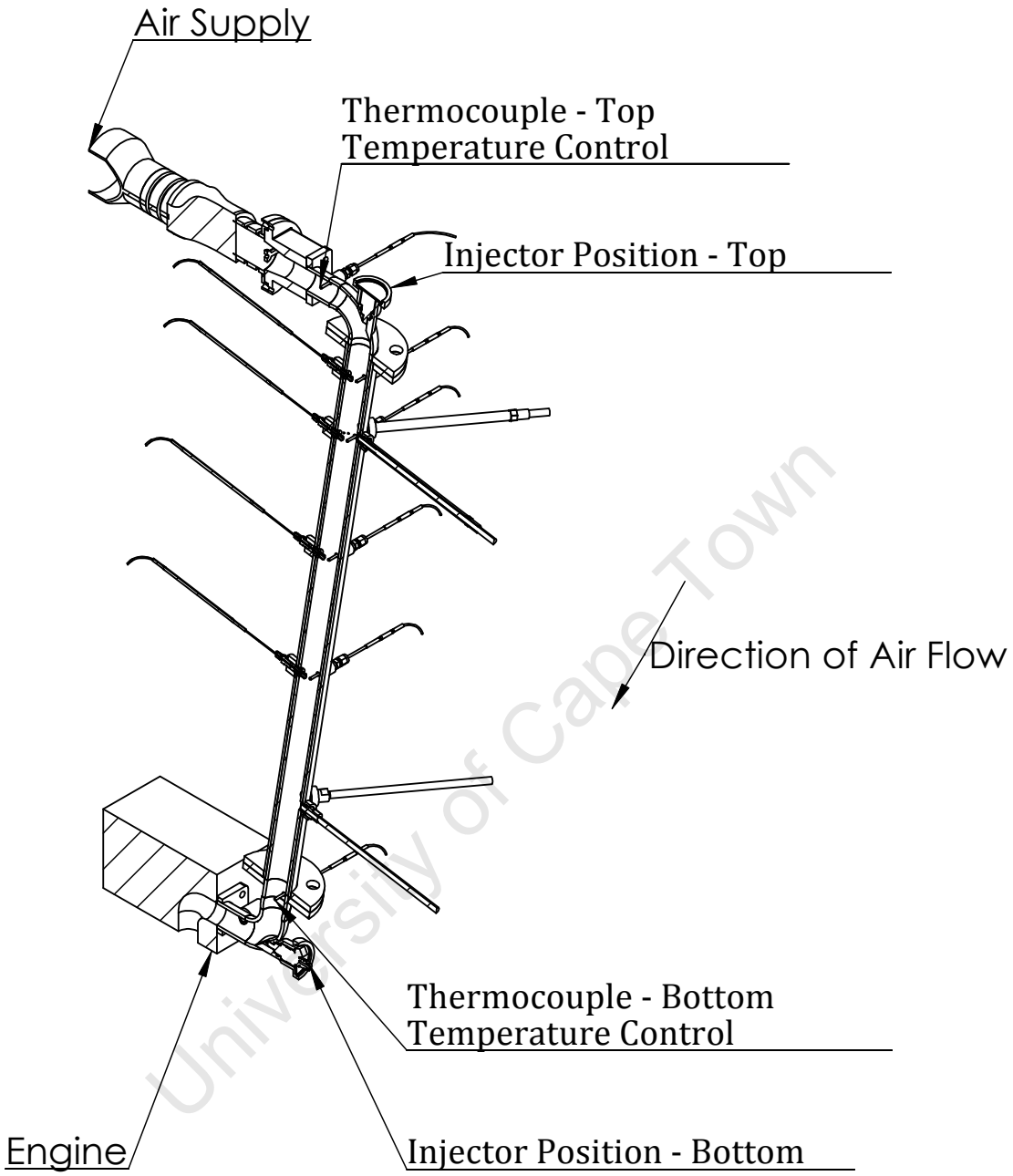

Figure A.1: Schematic of inlet manifold

Injection of Fuel

The manifold was required to house the injector both in the traditional PFI position as well as an upstream position. Figure A.2 shows the two positions that were provided for the injector.

The bottom injection point was designed to match the original injector manifold in terms

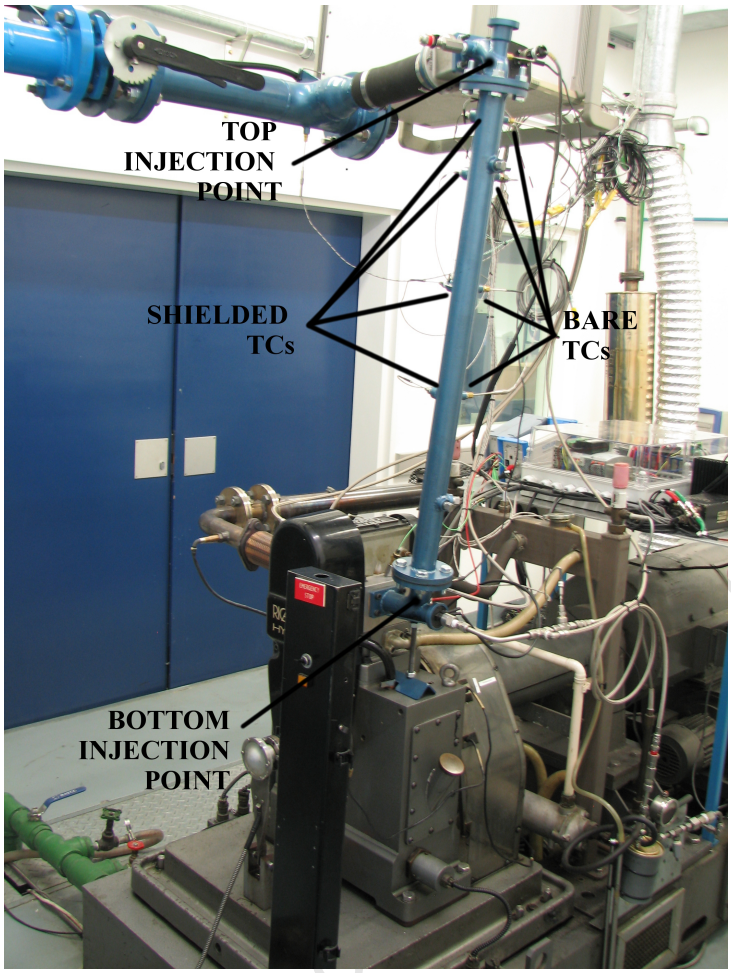

Figure A.2: Inlet manifold used during experimental work

of geometry with relation to the cylinder head port and inlet valve. The top injection point was designed so that the fuel would be injected down the centre of the manifold length.

Temperature Measurement

Two types of temperature probe were used. A shielded thermocouple, illustrated by the schematic of Figure A.3, was aimed at giving an indication of the gas temperatures along the manifold, while plain thermocouples were inserted to measure droplet temperatures.

These two types of thermocouple were used to provide an indication of the evaporation process occurring along the length of the manifold. This is discussed in further detail in the main body in Chapter 3.2.3.

Furthermore thermocouples were placed to gain an understanding of the wall temperatures seen. They were placed at two points, one at the half-way point of the inlet manifold and one at the quarter-way point from the upstream injection position. The thermocouples consisted of bare wire thermocouples placed on the inside of the

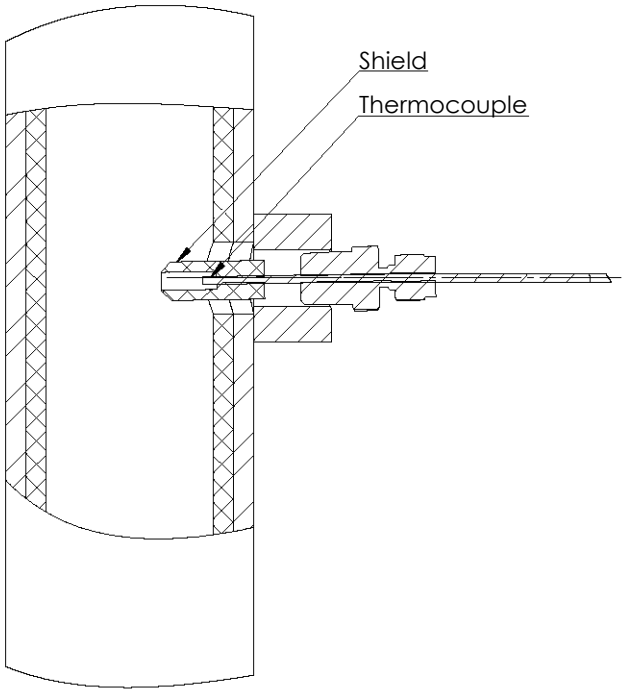

Figure A.3: Cross section schematic of shielded thermocouple design

Teflon liner. Bare wire thermocouples were also placed at the same point between the liner and the manifold pipe, as well as on the outside of the manifold pipe.

The thermocouples on the inside of the Teflon liner were used to determine the wall temperature present, which was used in the modelling study as an input.

Appendix B

Combustion Data Processing

B.1 Pressure Trace Smoothing

The raw pressure trace, captured at 0.1 CAD resolution, was smoothed and converted to 1 CAD resolution before being saved to hard drive. (A section of each trace where knock occurred was stored at the raw 0.1 CAD resolution). This smoothed trace was also used for a number of calculations subsequently, such as the heat release.

The smoothing was done by the Indicom 1.6 software, where a high pass filter was used to smooth the trace.

Figure B.1 shows a sample full pressure trace, and the subsequent smoothed trace. A logarithmic plot of pressure versus volume is shown in Figure B.2, to further highlight this. The noise from inlet valve closure and the knock oscillations can be seen to be satisfactorily smoothed out, while the pressure trace is not compromised in terms of shape or peak pressure.

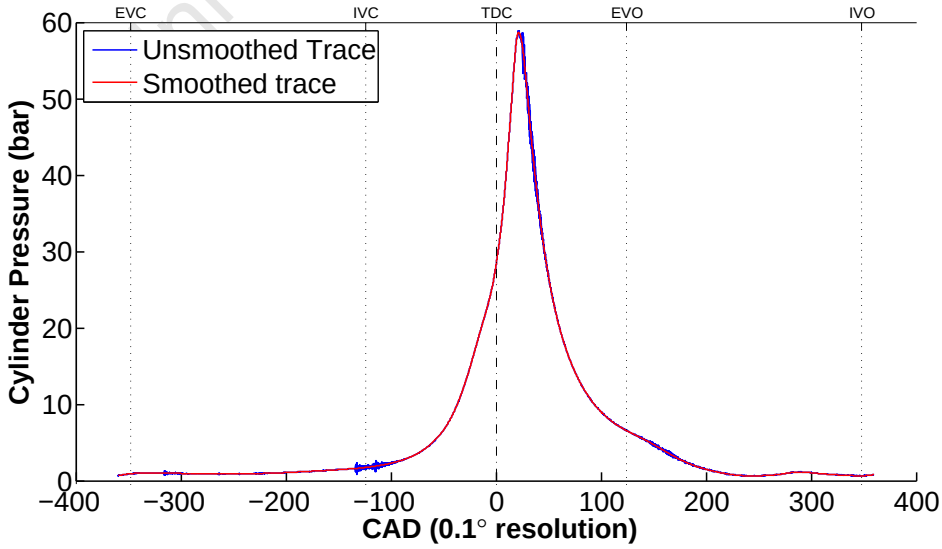

Figure B.1: A pressure trace, showing noise and smoothing thereof

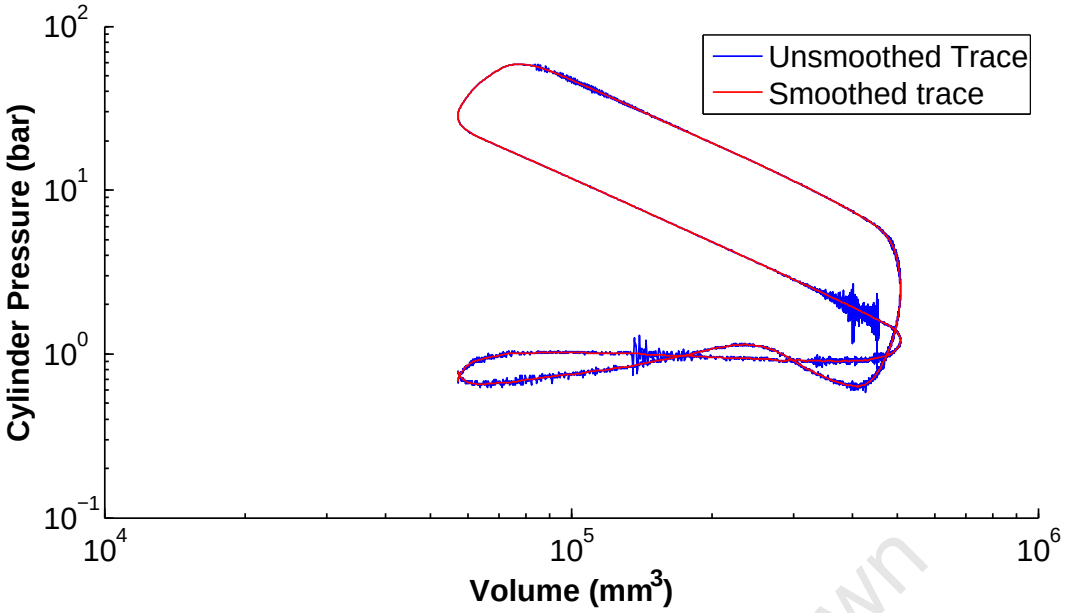

Figure B.2: Log pressure-volume plot, showing noise and smoothing thereof

B.2 Absolute Pressure Referencing

The use of piezo-electric transducers for in-cylinder pressure measurement presents the challenge of determining the absolute pressure value of the recorded trace, as the transducer only measures the relative change in pressure. This process is referred to as 'pegging' the trace, or zero-line detection.

To test whether the absolute pressure value is correct, a log P-V diagram can be used. The essence is that the inlet and exhaust stroke should be straight on the diagram. Any curvature indicates an error in the absolute pressure referencing. Other faults can also be detected with this diagram [85].

The pressure trace pegging proved a challenge in this work as the most regularly and easiest to use methods failed. In hindsight the thermal shock, as described in Appendix C.5, was clearly the cause for this.

The method that was found to work in this study was a thermodynamic zero-line pegging. It involves the assumption of a constant polytropic coefficient for a section of the trace. This section of pressure trace is then compared to a calculated pressure change over this span using the assumed polytropic coefficient. This method uses a section of the trace that is not influenced by the thermal shock, which explains its success compared to the other methods attempted.

Equation B.1 applies to a volume of gas under polytropic compression/expansion.

$$\frac{p_{2,meas} + \Delta p_n}{p_{1,meas} + \Delta p_n} = (\frac{V_1}{V_2})^n = C \tag{B.1}$$

Therefore :

$$\Delta p = \frac{C p_{1,meas} - p_{2,meas}}{1 - C} \tag{B.2}$$

where	p	:	pressure
	V	:	volume
	C	:	calculated constant
	n	:	assumed polytropic coefficient
subscripts:	1	:	1st chosen point
	2	:	2nd chosen point

The values recommended for n for a petrol engine are 1.32 to 1.33, while the range recommended for the calculation is during compression, from about 80 to 60 CAD before TDC.

Reference [86] was used in determining this and offers other methods as well.

Figure B.3 shows the final log PV diagram, where the inlet and exhaust stroke show straight line gradients.

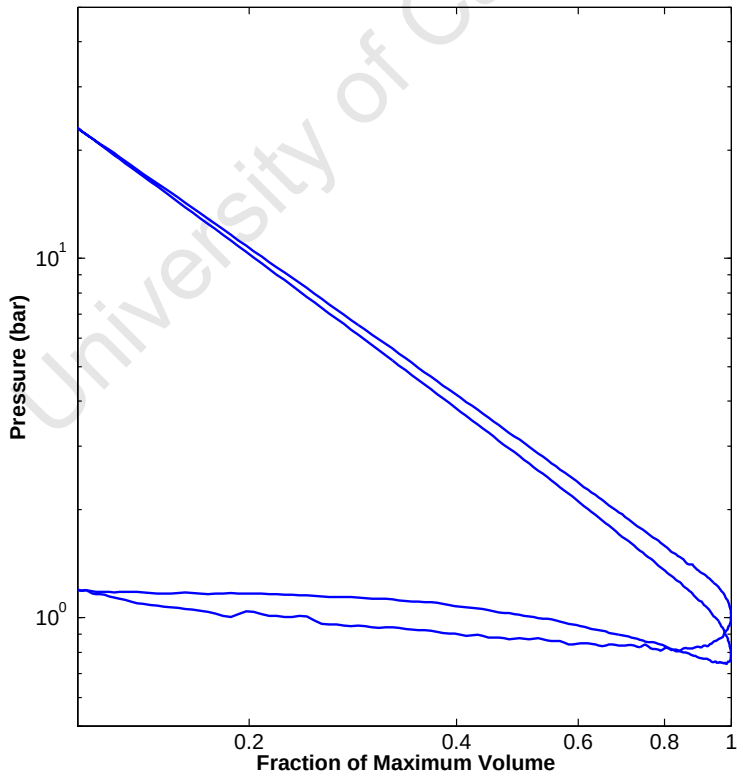

Figure B.3: Log PV diagram of sample motored trace

B.3 Knock Point Detection

The determination of the point where knock occurs in every trace was required. This was both for comparison with the model's prediction of where knock would occur as well as for the heat release fitting, to fit the Wiebe function to the non-knocking section of each trace. Two methods were employed based on different criteria.

The first method made use of the high frequency component from the filtered trace. The trace was passed through an algorithm that detected the first pressure oscillation above a set value and marked this as the knock point. This value was set to 50% of the peak pressure of each knock trace.

This method worked well when the peak pressure of the knock trace was at the beginning of the knock, which was often. However occasionally the peak pressure would be a period after the discernible start of knock, causing the detected knock point to be later than reality by 1 or 2 CADs.

The second method involved use of an algorithm to detect the valley point between the two peaks of the heat release trace of a knocking cycle.

This method suffered when the two peaks were less than well defined. This was especially true when knock occurs very early in the cycle.

Figure B.4 shows the difference between the two strategies in detecting the knock peak. As can be seen, there is a difference between the two knock points detected of about 3 CAD. This seems to suggest that there is a delay between the increasing of the heat release due to knock and the resultant pressure oscillations.

It was decided to use the onset of the pressure oscillations as the knock point in future work. These pressure oscillations are traditionally associated with the detection of knock. The heat release profile method was used for the division of the heat release to allow for the fitting of the Wiebe function to the heat release profile of the non-knocking section of the pressure trace.

B.4 Engine Heat Release

The heat release of the pressure traces was initially calculated by the Indicom 1.6 software. However, due to the pressure pegging occurring in post-processing of the engine data, the heat release had to be recalculated.

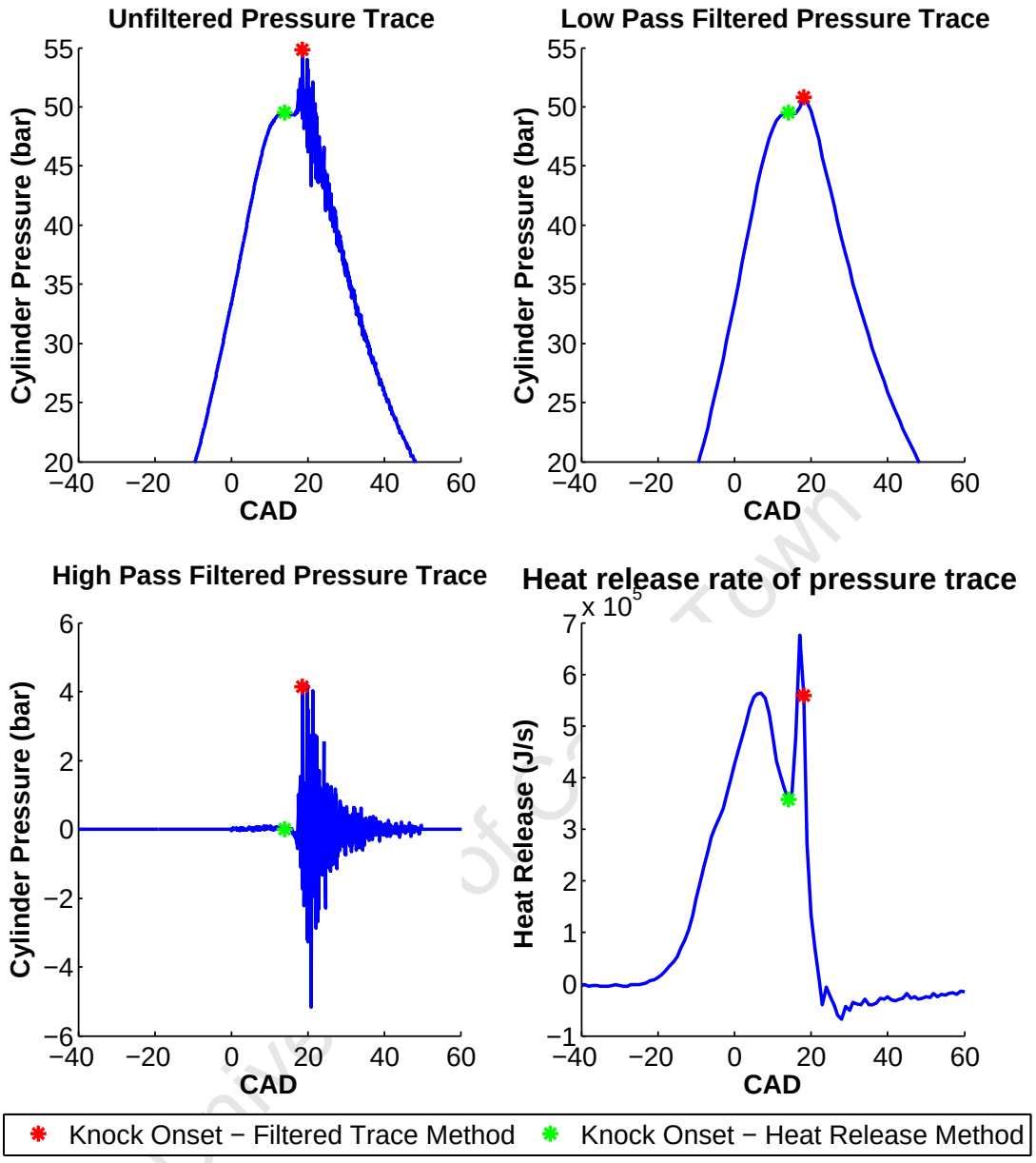

Figure B.4: Comparison of knock point detection strategies

Equation B.3 shows the calculation of the rate of heat release. [8]

$$\frac{dQ_c}{d\theta} = \frac{\gamma}{\gamma - 1} p \frac{dV}{d\theta} + \frac{1}{\gamma - 1} V \frac{dp}{d\theta} + \frac{dQ_{ht}}{d\theta} + \left(\frac{dQ}{d\theta}\right)_{crevice\,effects} \tag{B.3}$$

where	p	:	pressure
	V	:	volume
	Q	:	heat transfer
	θ	:	crank angle degrees
	γ	:	ratio of specific heats
subscripts:	ht	:	heat transfer to chamber walls
	ch	:	combustion heat release

The crevice effects were ignored due to their small influence [8].

B.5 Accounting for Cyclic Variation

Cycle-to-cycle variation in a SI engine occurs for a number of reasons, such as changing air dynamics and variations in flame kernel development [8]. Additionally, knocking is itself a highly variable process. As such this variation needs to be taken into account when trying to determine representative engine conditions.

Figure 3.4 highlights this, as the variation in IMEP over 300 cycles can be seen, with varying intensities of knock occurring.

As the pressure trace itself cannot be averaged to determine an 'average' pressure trace on which the heat release analysis could then be performed, a heat release calculation was performed for each of the 300 cycles. The subsequent Wiebe coefficients were then averaged to produce a representative burn profile for each operation set point.

B.6 Calculation of K and OI

KLSA is the measure of the knock resistance of a fuel that was used in this study. A linear relationship is usually used to relate the antiknock quality to the RON and MON. As such, we can then say that:

$$KLSA = aRON + bMON + c \tag{B.4}$$

However, if we write this as:

$$KLSA = (a+b)\left(\frac{a}{a+b}RON + \frac{b}{a+b}MON\right) + c \tag{B.5}$$

This allows us to equate the OI to

$$OI = \left(\frac{a}{a+b}RON + \frac{b}{a+b}MON\right) \tag{B.6}$$

and

$$KLSA = c + (a + b)OI \tag{B.7}$$

Thus, as we defined earlier the OI as

$$OI = (1 - K)RON + KMON \tag{B.8}$$

We thus have:

$$K = \frac{b}{a + b} \tag{B.9}$$

To calculate K and the OI at a specific operating condition in an engine, a quantitative measure of the antiknock quality of a number of fuels is needed, such as KLSA or KLMP.

The antiknock quality indicator of the fuel (KLSA will be used in this thesis) is then correlated to OI, as in Equation B.10. A K value is then found, through linear regression, that provides the best fit for this correlation [16].

$$OI = \left(\frac{a}{a + b}RON + \frac{b}{a + b}MON\right) \tag{B.10}$$

$$K = \frac{b}{a + b} \tag{B.11}$$

This calculation requires at least three fuels as well as fuels that have RON numbers and MON numbers that show no correlation. Such a correlation would mean that the improvement in the KLSA could be linked to either the RON or MON numbers. As such, the relative contribution of each octane number to the OI would be indeterminable. Without knowing the relative contribution of each octane number, we cannot determine the relative operating condition we find ourselves in.

This information is compiled from work by Kalghatgi et al. [16, 28, 29].

Appendix C

Experimental Investigation Difficulties

Throughout the experimental leg, a number of difficulties were encountered. These ultimately influenced the manner in which the experimental investigation was conducted, as well as the manner in which the data obtained was analysed and used.

Here follows a description of many of the issues encountered. Some that did not have an influence on the final results were included for completeness sake.

C.1 Pre-Ignition during Ethanol Operation

Unusual knock was encountered when running on ethanol under the higher boosted conditions (0.3 - 0.5 bar boost). As the spark timing was gradually advanced from a point of no knock, very faint knock would be seen and then almost immediately violent knock would start occurring.

This knock would runaway and retarding of the spark timing or switching off of the spark would not diminish it. Fuelling would have to be stopped to halt this severe knocking condition. These conditions thus would not allow for control of the KL to the prescribed 1 bar.

Additionally, the pressure trace signal recorded would eventually diminish. This was identified as a data capture error, rather than a real phenomenon, as the engine could still be heard knocking when these traces were seen. Figure C.1 shows raw signal of a typical progression of this knock type, while Figure C.2 shows a progression where this diminished pressure signal was captured.

This event was identified as pre-ignition due to the runaway nature of it and the pressure traces showing early ignition, as seen in Figure C.1.

This event occurs when the AF charge is pre-ignited in the cylinder chamber prior to the spark plug igniting the charge. This ignition is initiated by a hot surface. It is a runaway condition as the charge is now ignited by a hot spot and as such stopping the spark has no effect on the event. Fuelling must be cut to stop this [8].

Inspection of the spark plug further corroborated this hypothesis, as the ceramic of the plug was white with small black deposits, which is characteristic of an overheated

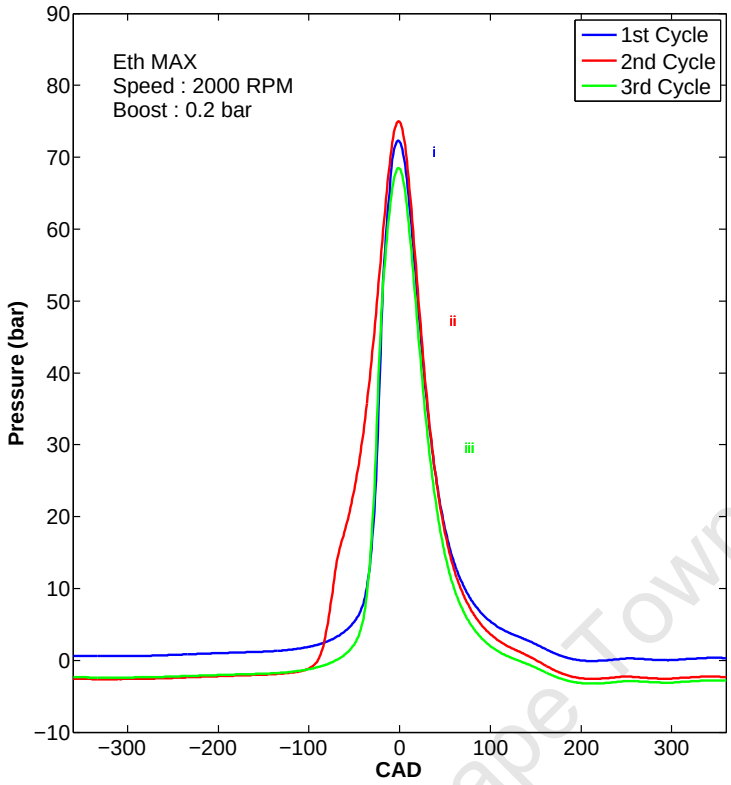

Figure C.1: Ethanol pre-ignition (smoothed trace)

spark plug or a spark plug that has suffered from pre-ignition [87]. This suggests that the spark plug itself was the source of the hot spot. Additionally, alcohol fuels are more sensitive to pre-ignition compared to petrol. [88]. Figure C.3 shows the damaged spark plug.

The spark plug was thus removed and swapped for a colder spark plug. This means that a spark plug with a greater heat sink and thus lower operating temperature was used.

The pre-ignition diagnosis was further justified when the severe runaway knock was solved by this switching to a colder spark plug, with a controllable KL now being achieved on the boosted ethanol runs and the diminished signal no longer appearing.

C.2 Wild Ping on ULP 95 operation

Unusual knock of a different type was found to occur when running under the higher boosted conditions on ULP 95.

This knock was characterized by borderline or near non-existent knock interspersed with huge knock peaks. Figure C.4 shows the captured pressure trace of one such knock event.

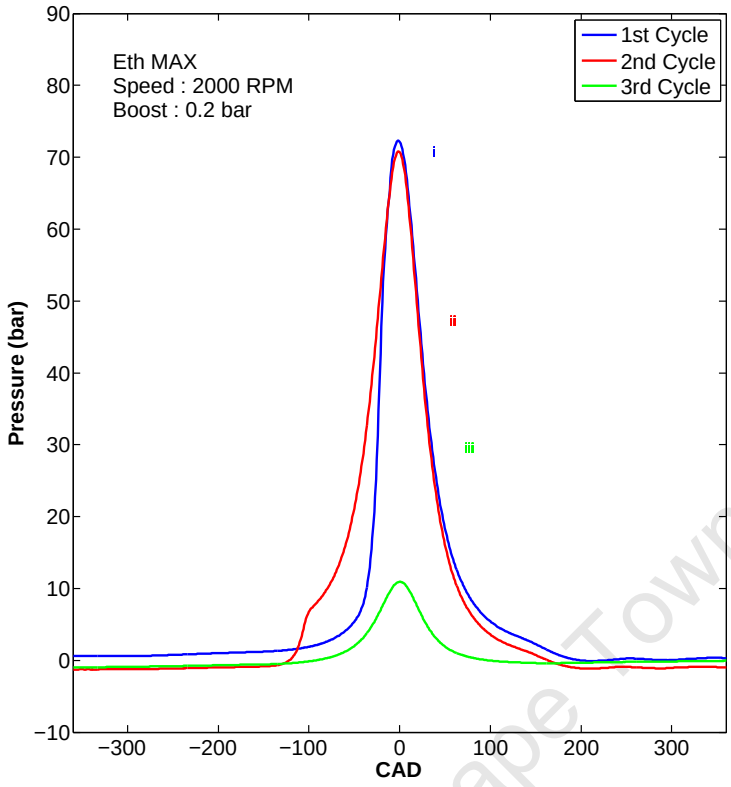

Figure C.2: Ethanol pre-ignition and overheating of transducer (smoothed trace)

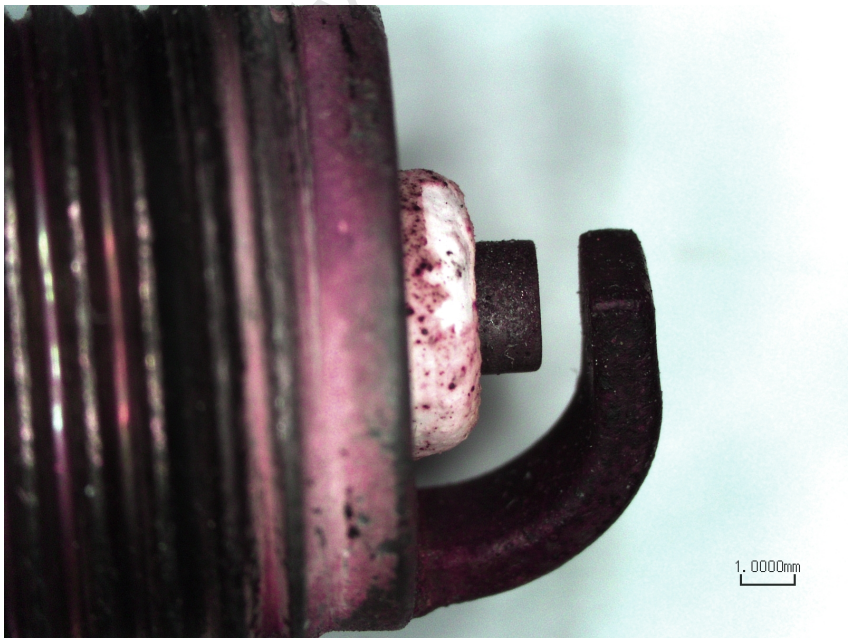

Figure C.3: Spark plug showing signs of pre-ignition

This knock phenomenon would not runaway, and as such pre-ignition was ruled out.

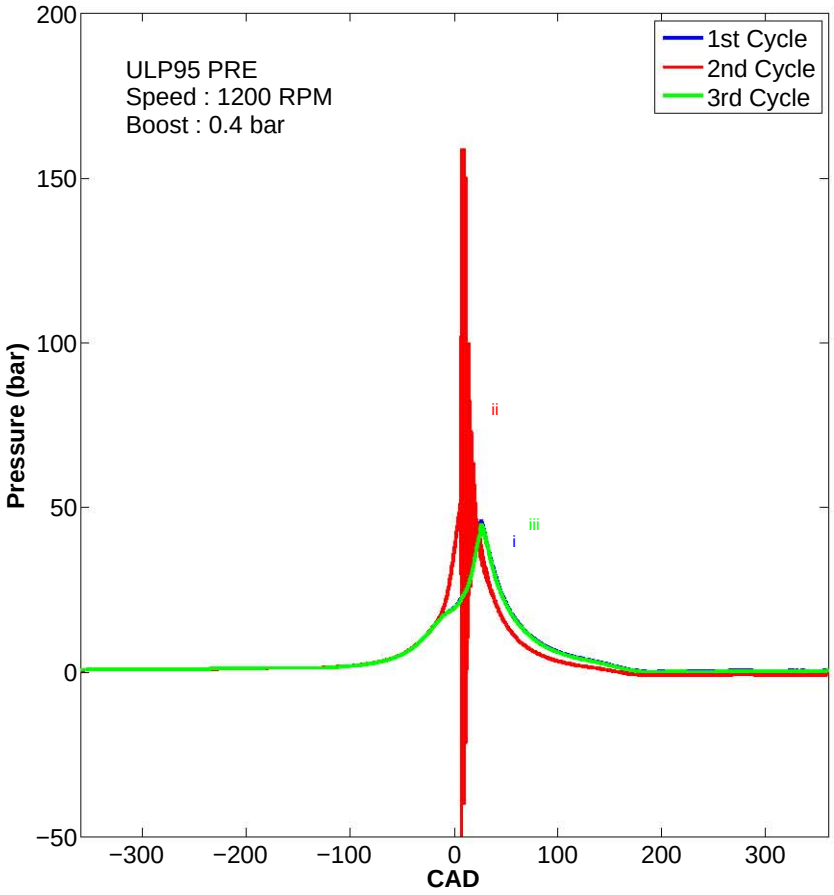

Figure C.4: ULP 95 wild ping (smoothed trace)

This was further corroborated by the spark plug showing no pitting, a characteristic of pre-ignition.

Immediately after this phenomenon had been seen, an exhaust valve failure occurred. Figure C.5 shows the damaged exhaust valve. Figure C.6 shows the damaged valve seat. Signs of pitting are visible on the cylinder head and pitting was seen on the piston face as well.

Wild Ping was hypothesized as the type of knock experienced here. Wild ping is pre-ignition of the fuel/air charge initiated by a glowing deposit. It does not cause runaway pre-ignition, as the glowing deposit that initiates the knock is subsequently destroyed by the knock itself [8]. Thus it produces sporadic knock.

It was thought that the use of the colder spark plug (used due to the surface ignition encountered during ethanol operation, discussed previously) might have resulted in deposit build up on the spark plug.

A spark plug that operates too hot causes surface ignition while too cold and deposits such as soot are not burned off, which usually results in impeded spark discharge [87].

The spark plug was subsequently switched to a hotter one, and the phenomenon was

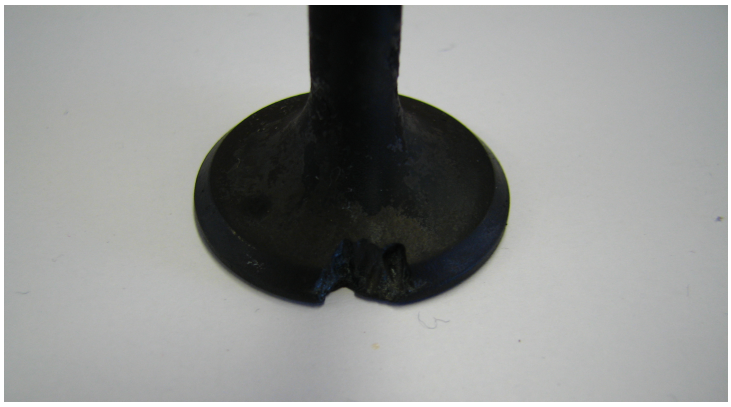

Figure C.5: Damaged exhaust valve, thought to be caused by wild ping

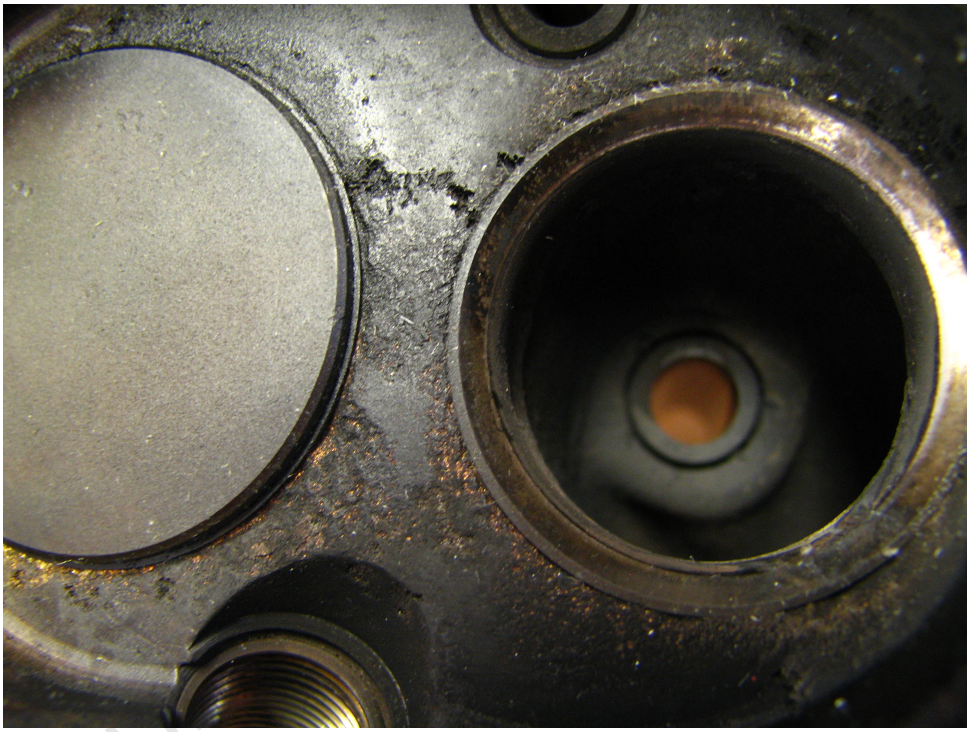

Figure C.6: Damaged valve seat and pitted cylinder head

shown to disappear. This further validates the wild ping hypothesis.

It should be noted that the pitting seen however cannot be solely attributed to the wild ping, as the engine had already experienced the pre-ignition previously mentioned, as well as running under knocking conditions for a number of tests. It thus highlights the damage an engine experiences under knocking conditions.

C.3 Wetting of Manifold Temperature Control Thermocouple

Testing of the first fuel, namely iso-octane, showed up unusual temperature profiles along the length of the inlet manifold at a speed of 4000 RPM under MAX manifold conditions. Figure C.7 displays an example of this temperature drop, as well as the labelling of the various thermocouples along the length of the manifold. The cause for the temperature drop between the T_{HEATER} thermocouple and the $T_{TOP-CONTROL}$ thermocouple was initially unknown.

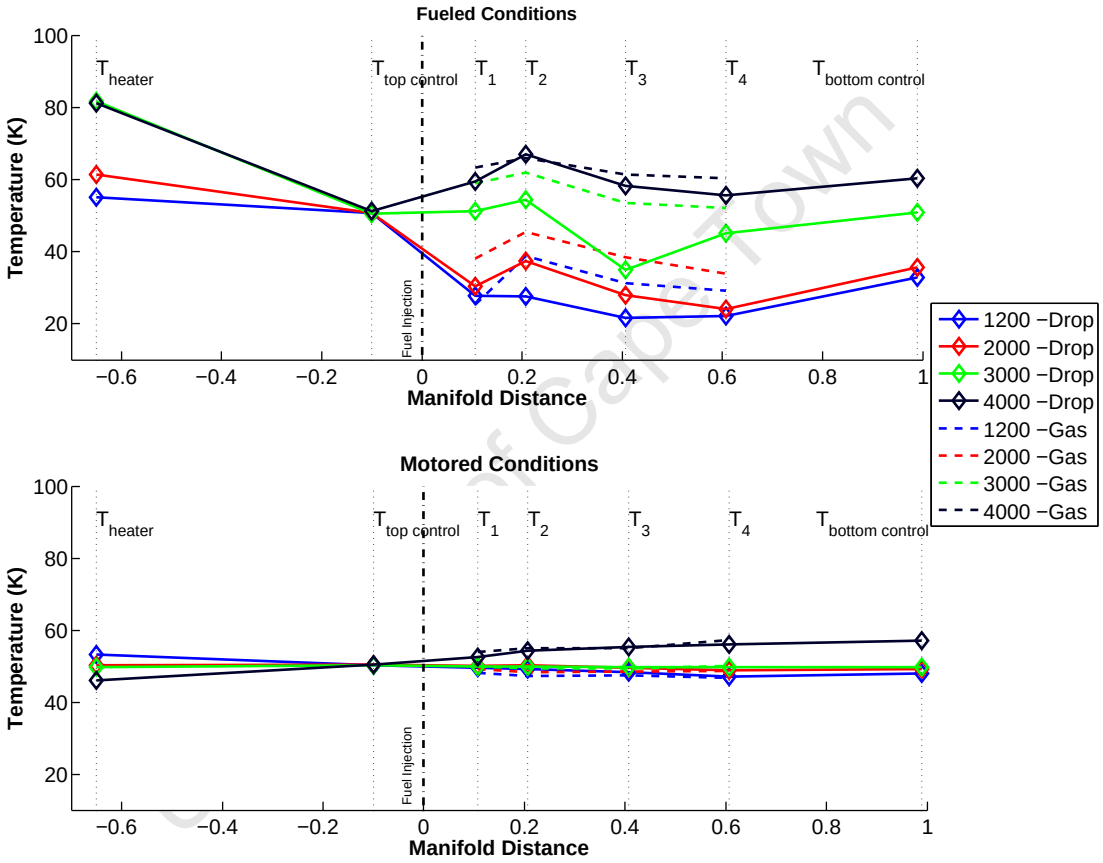

Figure C.7: Wetting of top control thermocouple

This anomaly was noted and testing was continued with the other fuels, with plans made to possibly repeat the runs if a solution was found.

The cause of the problem was discovered during the testing of the second fuel, ethanol. It was noted that as soon as fuel was injected at the top manifold position for the MAX evaporation case, the $T_{TOP-CONTROL}$ thermocouple temperature would drop. This showed that thermocouple wetting was taking place.

This was unexpected, as the $T_{TOP-CONTROL}$ thermocouple was approximately 100 mm upstream of the injector. However the instantaneous dropping of the temperature

Table C.1: Temperature set-points at T_{HEATER} thermocouple

Speed (RPM)	1200	2000	3000	4000
Temperature (℃)	53	50	50	46

when the fuel was injected was obvious.

The cause of this is phenomenon is unknown. The untuned manifold may have resulted in significant pulsation of the air flow causing the liquid fuel injected into the manifold to travel in the reverse direction and wet the upstream thermocouple.

This meant that the temperature control for the MAX manifold cases, where the inlet air was controlled to 50 ℃ at the $T_{TOP-CONTROL}$ thermocouple, was incorrect. The inlet air was heated to a far higher temperature to force the wetted $T_{TOP-CONTROL}$ thermocouple to 50 ℃.

The higher temperatures seen at the T_{HEATER} thermocouple were considered to be true air temperatures as this thermocouple showed no temperature drop when fuel was injected into the manifold, as it was too far upstream of the injection point to allow for wetting through pulsating reverse flow. Subsequently, temperature control was switched to this heater thermocouple.

However the inlet air temperature could not be set to be controlled to 50℃ at the T_{HEATER} thermocouple. There was a difference in temperature between the T_{HEATER} and $T_{TOP-CONTROL}$ thermocouple and a set point of 50℃ at the position of the $T_{TOP-CONTROL}$ thermocouple was still required, to allow for comparison with previous runs that did not suffer from wetting.

To ensure that the air temperature at the $T_{TOP-CONTROL}$ thermocouple was controlled to 50℃, motored traces were used to provide the set points that the air temperature at the T_{HEATER} thermocouple would be controlled to.

The lower half of Figure C.7 shows the motored temperature profiles, illustrating the difference in temperatures between the $T_{TOP-CONTROL}$ and T_{HEATER} thermocouples, and Table C.1 shows the temperatures at the T_{HEATER} thermocouple that were subsequently used as control set-points for the MAX case.

This was applied to all subsequent fuels tested, with the ethanol runs redone, which only excluded iso-octane from this correction. The dyno failure, described shortly, unfortunately did not allow for retesting of the iso-octane.

The temperature profiles of each of the iso-octane MAX runs were then individually inspected and compared to the motored runs to identify signs of wetting. Those runs where wetting was evident were subsequently excluded from the study. The wetting of the thermocouples fortunately only influenced the higher speed runs, as can be seen in Figure C.7, limiting the impact of this effect.

C.4 Noise Influence on Knock Measurement

Noise was seen to influence the KL determination when operating at 4000 RPM under certain conditions. This problem was identified when runs at 4000 RPM did not exhibit the exponential increase in mean knock peak as the spark was advanced.

Figure C.8 compares the two cases where the progression into knock can be seen. The top graph shows the previously mentioned exponential increase in knock while the lower figure shows a near linear increase in knock peak as spark timing is advanced, with the knock peak going above the KL of 1 bar. Note the difference in spark advance scales used on the two figures which is also illustrative of the problem.

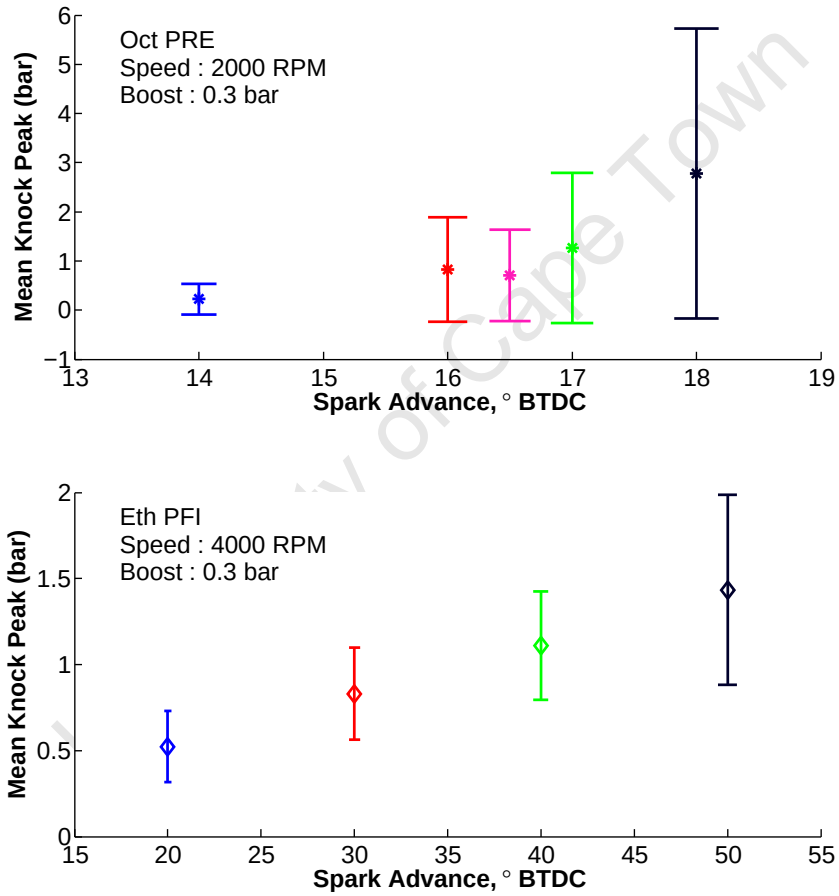

Figure C.8: Influence of noise on knock amplitude progression

An attempt was made to solve this by changing the cut-off frequency of the high-pass filter that determines the knock limit, to filter out the noise. However, this had little effect, as the noise and knock signal were shown to be inseparable with this method.

As time conducting the experiments passed, it was found that experience helped identify the noise influenced data. To combat it, the spark timing was advanced until

a satisfactorily random knock signal was found, where the occurrence of knock was guaranteed. This signal would show though a knock peak well above the 1 bar KL.

The timing was then retarded back to non-knocking conditions and then advanced to a degree before the previously noted knock signal. This data was then recorded and taken as a representation of actual knock. This though was only possible where the noise influence was small and the knock intensity only taken slightly over the pre-determined KL.

However under some conditions this was not achievable as the noise influence was too great or the exponential increase in KA was never seen. While data was recorded at these points, the results were subsequently ignored for the knock analysis and data fitting.

C.5 Thermal Shock

Low level Thermal Shock

Puzzling in-cylinder pressure traces were found during the exhaust and inlet stroke of the fired runs, especially when compared to the motored pressure trace during this period, or the pressure seen in the inlet manifold. This is illustrated in Figure C.9.

The fired traces show lower exhaust and inlet stroke pressures than the motored traces, despite the fired traces having higher exhaust pressures due to combustion. The traces also eventually meet up at the end on the inlet stroke, thus dismissing pressure referencing errors as the cause.

After discussion and initial research, thermal shock was suggested as a possible cause.

Thermal shock refers to when the piezoelectric pressure transducer produces erroneous readings due to the thermal loading it experiences during combustion. The exposure of the transducer surface to the flame and heat during combustion causes temporary expansion of the transducer diaphragm, forcing the diaphragm to deflect [89]. As the transducer measures pressure by the deflection of the diaphragm, this effect produces a shift in the pressure readings.

All piezoelectric pressure transducers in fact suffer from this phenomenon and as such it is even quoted on the transducer data sheet the amount of thermal shock that one can expect from the transducer.

Lee et al. [89] and Rosseel et al. [90] show that the effects of thermal shock can continue into the exhaust stroke while Soltis [91] finds evidence of transducers that suffer well into the inlet stroke.

A high speed pressure transducer measuring the absolute pressure of the exhaust manifold can be advantageous in cases of thermal shock as it can provide comparisons much as the inlet pressure transducer did in this study, as seen in Figure C.9. An exhaust pressure transducer would however provide an indication of the

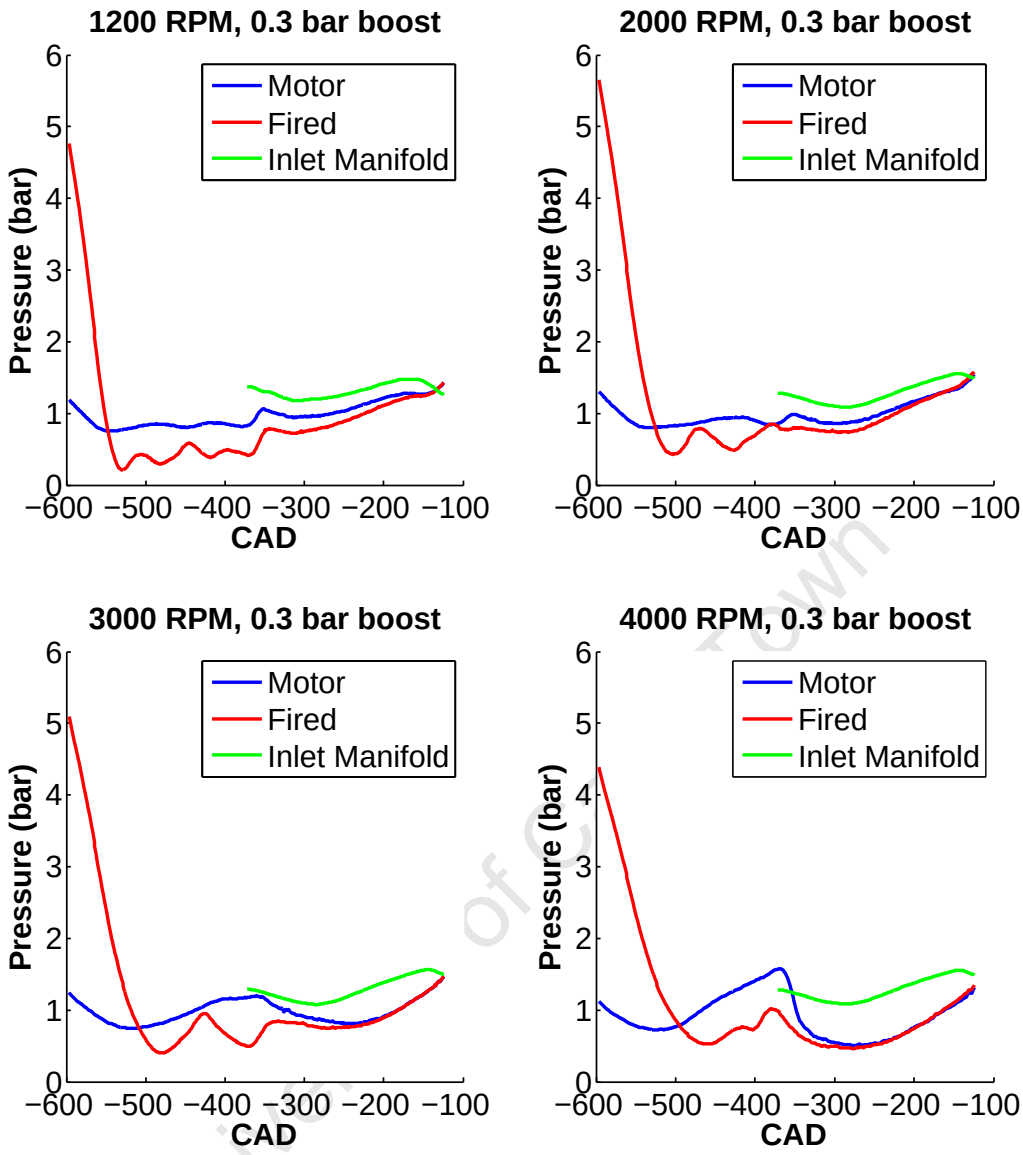

Figure C.9: Breathing pressure traces - motored and fired

thermal shock in the exhaust stroke, where thermal shock is most severe and would thus allow for the detection of less apparent thermal shock than that detected here.

An approach to identify whether data suffers from thermal shock is the Randolph segment theory, initially proposed by Randolph in [92]. This method looks at taking certain segments of the engine cycle and comparing the cycle-to-cycle variability of these segments. This highlights if there is cycle-to-cycle variability that is greater than expected for sections of the plot that should not experience much cycle-to-cycle variability. Indication of excessive cycle-to-cycle variability would suggest the presence of thermal shock.

Figure C.10 shows the segments that are used, namely the exhaust stroke (C1-C2),

intake stroke (A1-A2) and compression stroke (B1-B2). During these periods, cycle-to-cycle variability is expected to be low, so the presence of such variability points to thermal shock.

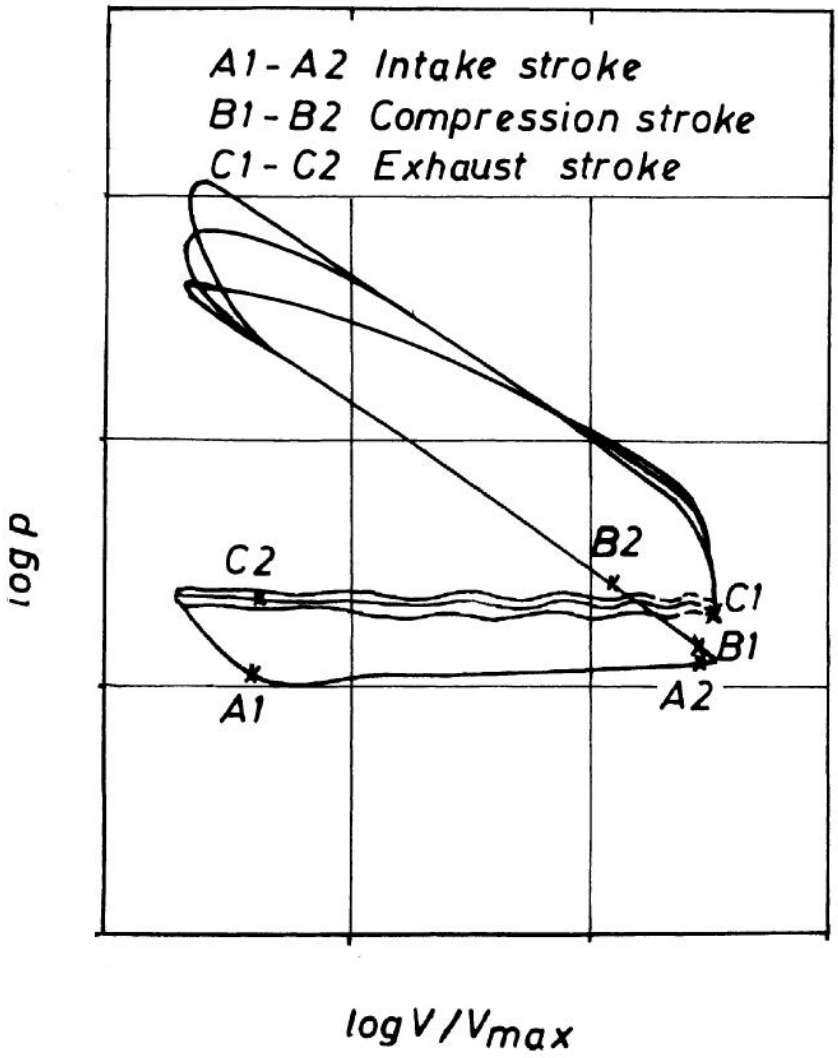

Figure C.10: Segments used for Randolph segment method, shown on a log p-V diagram

Figure C.11 shows the application of the Randolph segment theory to one of the test runs. If the points plotted are close to the origin, the variability is low and so no thermal shock is indicated. If the points form a line with a gradient of 1 it indicates cycle-to-cycle variability was generated outside of the segment. This is as the end points of the segment are both offset by the same amount, resulting in the plotting of a 45° line.

General scattering indicates cycle-to-cycle variability generated during the segment, and thus points to the presence of thermal shock in that segment [90].

Cycle-to-cycle variability was found in the exhaust stroke. Rosseel et al. [90] classified a number of transducers with various resistances to thermal shock using this method. Using this as a benchmark for how much variability is expected with minimal thermal

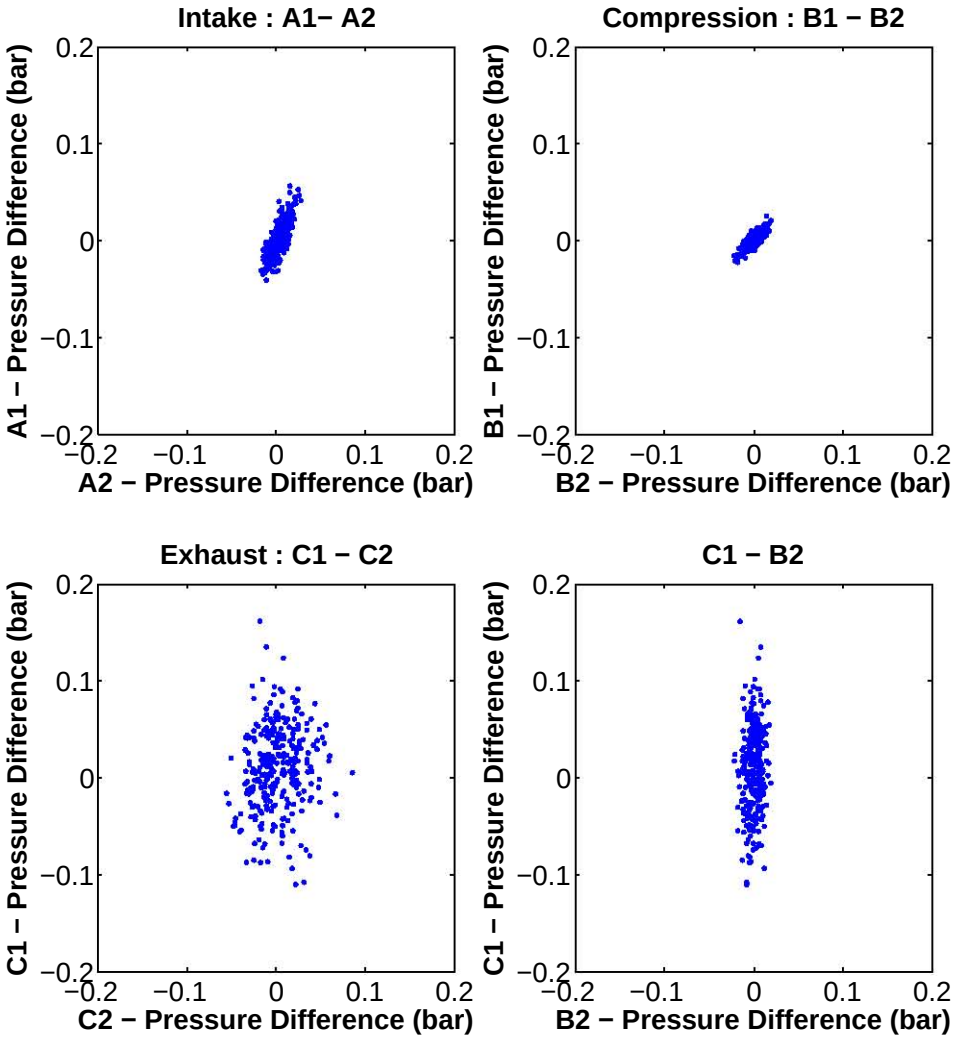

Figure C.11: Randolph plot

shock present, the variability seen in Figure C.11 is above acceptable limits. This data points then to the presence of thermal shock.

There is a possibility however that this variability is caused by exhaust gas dynamics. The analysis does at least ensure that thermal shock is not disproved.

The combination though of the variability together with evidence from Figure C.9, where the motored trace shows a far higher pressure during the breathing stroke, strongly points to thermal shock lowering the fired runs breathing pressure trace.

The quantification of the thermal shock's influence on the data captured is impossible without information about the temperature loading on the transducer (which would allow corrections to be made, as described by [89] and [93]) or the comparison with a more accurate transducer run in the same engine.

The effect it has on the readings however can be inferred from the other works done on the subject. The thermal shock will primarily cause a lowered pressure reading from

approximately the point of peak temperatures until possibly the end of exhaust or even intake stroke.

This will then cause erroneous IMEP calculations, lower the peak pressure and influence both the position of the 50% Mass Fraction Burnt (MFB) point as well as the 10 - 90% MFB duration [91]. The timing of the peak pressure will not be effected however [91].

The influence on KA is unknown. The transducer used in these experiments was located close to the centre of the cylinder head, with the spark plug also near the centre, meaning that the flame would reach the transducer before knock in the unburnt end-gas would occur.

As it is difficult to quantify the thermal delay between when the flame reaches the transducer and when the thermal loading distorts the transducer readings, it is difficult to know both the extent of the thermal shock on the transducer at the time of knock, as well as the influence this thermal shocking would have on the measurement of the high frequency pressure oscillations.

This influence on the measurement of the pressure oscillations and subsequent KL would influence the determination of the KLSA. The change of spark timing and boost (and thus load) would change the magnitude of the thermal loading and so could change the measurement of the KA, thus distorting the KL used throughout the experimental study.

However, as shown already, the KL increases exponentially with advances in spark timing. We can thus expect that any distortion of the KL through thermal shock would not result in a significant influence on the KLSA. The exponential increase of KL would still result in a KLSA at the same place, or very close at least.

Severe Thermal Shock

The transducer was found to produce severely diminished readings under a number of the highly boosted conditions. At the time of these readings, their cause was unknown. However after the above investigation into thermal shock, this can be attributed to severe thermal loading of the transducer.

This is highlighted previously in Figure C.2, where the transducer reading becomes diminished after the pre-ignition. Figure C.12 displays data captured for a non pre-igniting case where the pressure reading transitions from normal readings to become flattened with a lowered peak pressure.

Those runs whose conditions caused severe thermal shock had to be abandoned as no data of any meaningful nature could be captured by the transducer.

C.6 Dyno Failure

The testing was eventually halted due to failure of the dyno control. The dyno was found to no longer control the engine to the given set-speed. For example, at a set

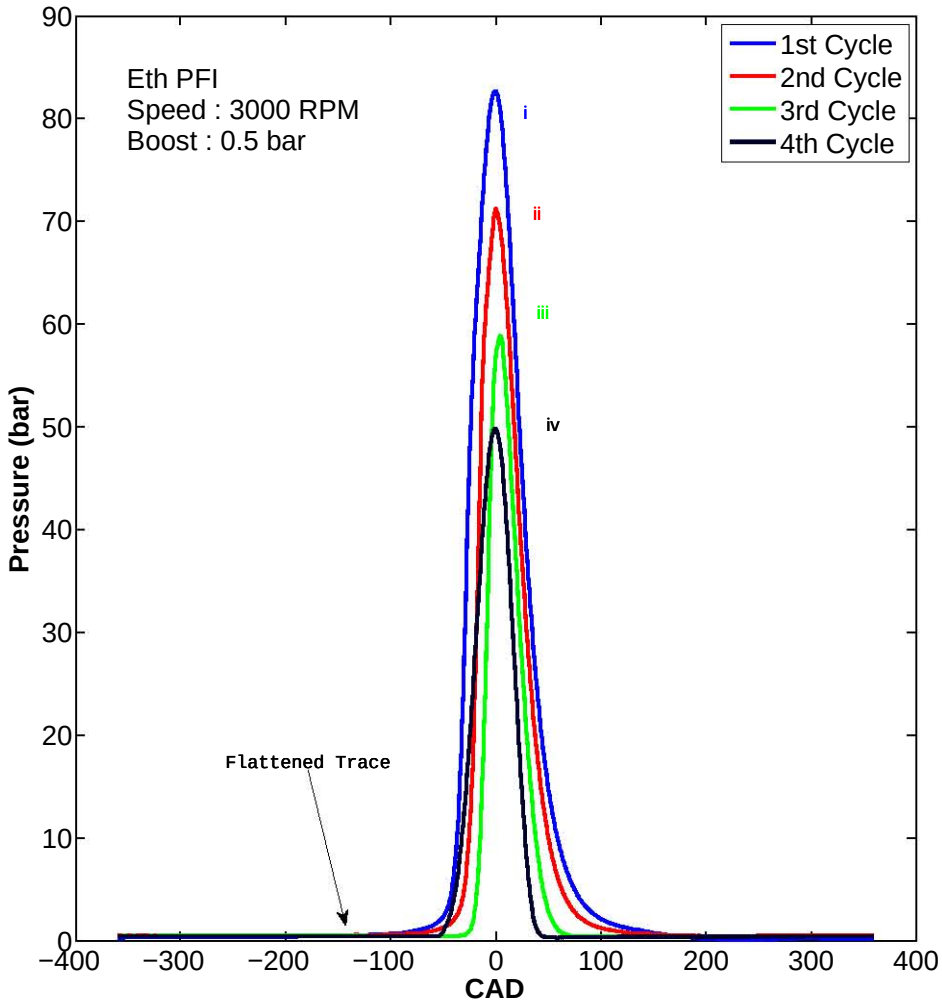

Figure C.12: Pressure trace recorded from transducer suffering from severe thermal shock

speed of 2000 RPM, the engine would sporadically oscillate from 2200 to 2700 RPM.

Unfortunately this failure occurred too late in the testing stages to allow time for repair. As such, this put an early stop to the testing, not allowing for all the initially planned data points to be captured or for the data points that suffered from the various issues detailed above to be re-run.

Appendix D

Injector Characterisation

Measurement of the injector spray droplet sizing was required so as to allow characterisation of the spray produced to allow for more accurate modelling of the droplet evaporation process. The droplet distribution would be represented by the Sauter Mean Diameter (SMD) as determined by a Malvern particle sizer.

D.1 Experimental Set Up

The Malvern particle sizer measures the droplet size distribution of a spray by measuring the deflection of a laser beam caused by the droplets.

This deflection is a result of refraction, the phenomenon where light changes direction due to its change in speed as a result of passing from one medium to another. The droplet size determines both the angle of deflection and the intensity of the scattering, with large droplets scattering light by a small angle and with high intensity and small droplets producing large angle scatter with low intensity. This scattered laser beam signal is then measured on a ring detector, consisting of a series of concentric photosensitive elements [94]. The refracted light pattern produced from a spray is thus dependant on the droplet size distribution, and this size distribution can be determined through Mie Theory or the Fraunhofer Approximation [95]. Figure D.1 illustrates this set-up.

The injector characterised was the one used for the experimental work and was a Bosch pintle type injector (Model number 0 280 150 704). Relevant injector characteristics can be seen in Table D.1.

Table D.1: Relevant injector data

Test Medium	Heptane
Spray Type	Hollow Cone
Spray Angle α_{80}	18°
Operating Pressure	250kPa

The data was recorded and analyzed using the Malvern software provided.

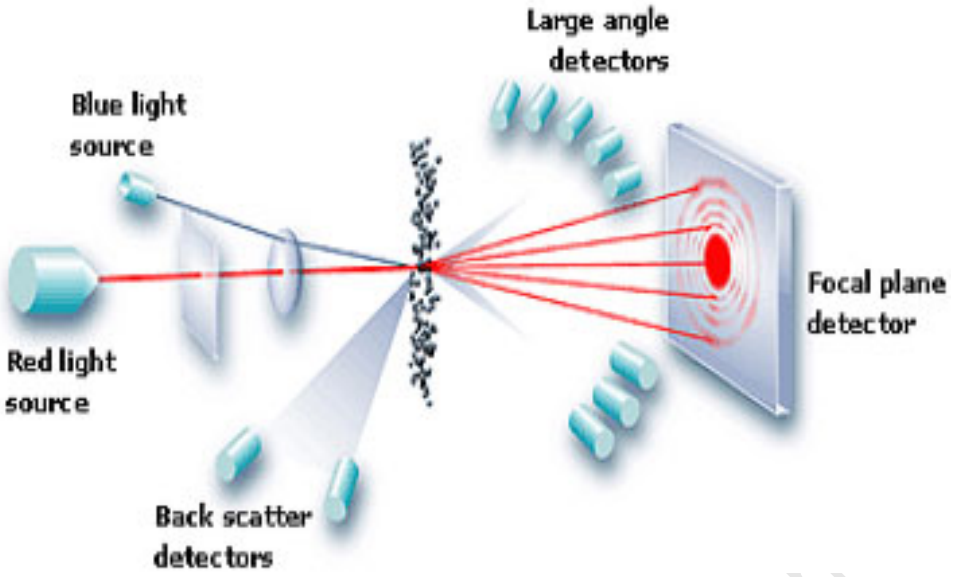

Figure D.1: Schematic of spray size measurement through diffraction techniques (Reproduced from [94])

The results produced represent an inherent mean of the spray produced. This is because sampling occurred at 1 Hz with the injector pulsed at 10 Hz, the rate the injector would be pulsed during operation at 1200 RPM.

The conditions under which the characterisation took place can be seen in Table D.2.

Table D.2: Injector characterisation default operating points

Fuel pressure	bar	2.5
Ambient Pressure	bar	1
Fuel Temperature	℃	19 - 21
Ambient Temperature	℃	19 - 21
Fuel		iso-octane
Distance from injector tip	mm	85
Distance from central axis	mm	5
Pulse Width		10 ms
Total cycle time		110 ms

D.2 Investigation Results

D.2.1 Beam Steering - Evaporative Effects

The initial test runs of the injector characterisation were performed on ULP 95. A distinctive bimodal distribution was observed, with an overwhelming quantity of very large droplets. Figure D.2 shows an example of this distribution.

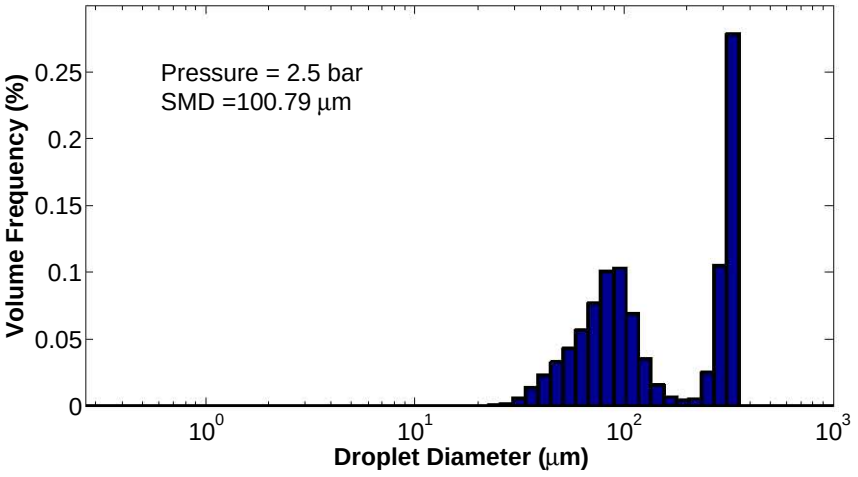

Figure D.2: Droplet size distribution for ULP 95 displaying beam steering

These results raised serious concerns, as the author had not come across any evidence of pintle injectors producing either a bimodal spray distribution or droplet sizes of this magnitude. Instrumentation error was not expected as this particular Malvern sizer had been successfully used just prior to characterise jet fuel sprays. It was found that varying fuel pressures, injector excitations, injectors (all of similar type) and beam position within the spray also had no effect on this distribution. The results were further called into doubt when it was found that the large second hump was present even when the laser was used to measure the very fine mist of fuel droplets just to the side of the injector spray.

A review of literature documenting the use of light diffraction techniques for spray droplet sizing (and in particular Malvern laser particle sizers) shed light on this problem.

Miller and Nightingale [96] and Lenz and Fraidl [97] make mention of this phenomenon and explain that the cause arises from evaporation of the fuel within the spray. As the laser sizer determines the droplet sizes from the refraction of the laser beam as it passes through the spray droplets, the presence of fuel vapour causes additional refraction as the beam passes through the vapour. This distorts the reading to indicate the presence of large droplets.

It was decided to attempt the characterisation with a less volatile fuel. iso-Octane was used, and while the second hump was reduced the bimodal distribution remained. Figure D.3 illustrates this second hump while Figure D.4 shows the raw data captured for Figure D.3, showing the signal captured by each detection ring.

Review of literature by Malvern [98] showed that they refer to this as “beam steering” and the recommended solution is to eliminate the readings of the lower detection rings.

The laser beam refraction is measured by a set of concentric detection rings, numbered from the inside central rings outwards. The refraction angle produced is smaller the larger the droplet. As a result, the central rings measure the presence of the largest droplets, and so not including them in the calculation eliminates the

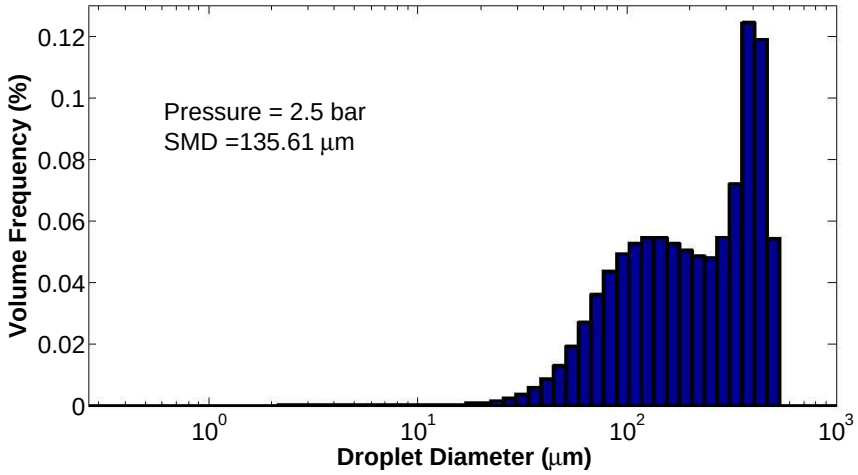

Figure D.3: Droplet size distribution for iso-octane, showing beam steering

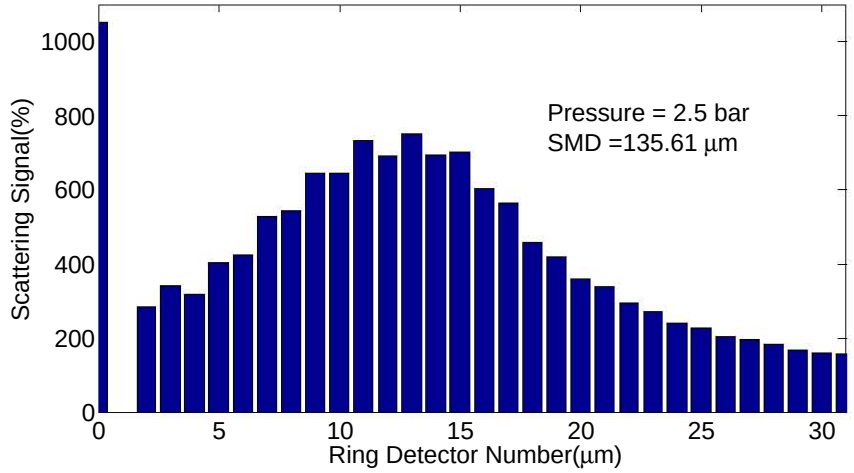

Figure D.4: The raw scattering data for iso-octane, showing beam steering (The 1st detection ring is faulty)

erroneous signal. This can be easily achieved by the changing of a setting on the particle sizing software.

This method must be exercised with caution, as the elimination of real injector phenomena is a concern. However the spray was seen to have a fine appearance, except for the four or so thicker streams. Measurements were not made though in these streams, and they were deemed to contain a small overall quantity of the fuel.

Other approaches are available, such as Cossali and Hardalupas [99] who prevent this problem by conducting the spray characterisation in a test chamber that is filled with saturated vapour of the test fuel. However this approach is out of the scope of this project.

As a result it was decided to adopt the elimination of ring detector data. Analysis of the scattering data seen in Figure D.4 shows that there is a hump present in the lower

detection rings that ends at the 5th ring. This hump is indicative of beam steering that is occurring. Comparison of data across the tests showed however that elimination of data from the 4th ring and lower did in fact remove the bimodal distribution.

Figure D.5 shows an example of the change in calculated particle distribution this approach produced, applied to the data from Figure D.4 and D.3.

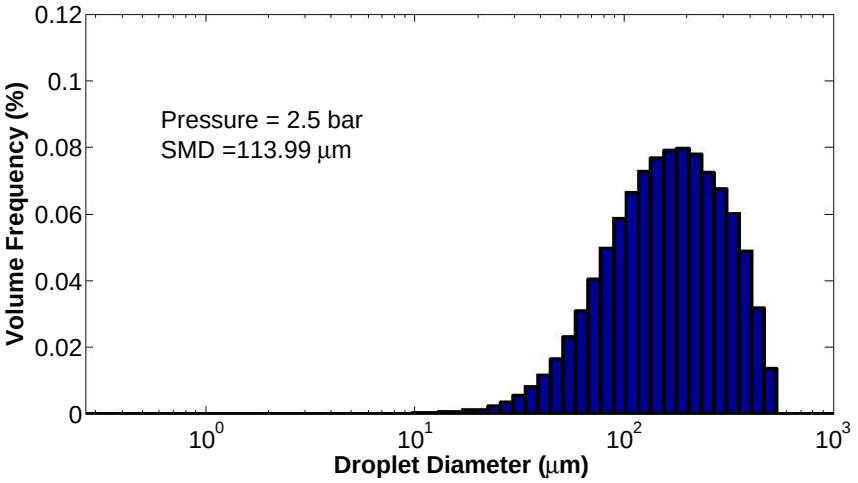

Figure D.5: Droplet size distribution for iso-octane, showing corrected droplet distribution

D.2.2 Injector Spray Distribution and SMD

Pressure effects

A pressure sweep was conducted from 1.5 to 4 bar (gauge). The results for the pressures from 2 bar and above can be seen in Figure D.6. At 1.5 bar the injector did not atomize the fuel, instead "hosing" the fuel in a single stream. These results were thus omitted.

This increase in atomization of a spray as fuel pressure increases is a well known phenomenon [22].

While atomization increased with increased fuel pressure, the spray angle was seen to visibly increase as well, particularly at the 4 bar set-point. This worsens the transient response of a port-fuel injector, as the fuel is not as directly targeted onto the back of the inlet valve.

A final injection pressure to be used for the engine operation of 3 bar was chosen (rather than the recommended 2.5 bar), as this reduces the sensitivity of the spray distribution to the expected 0.5 bar decreased pressure differential the injector will experience under boost manifold conditions (the SMD of the droplet distribution decreases by 10 μm from 3 to 2.5 bar, but 30 μm form 2.5 to 2 bar) while providing the correct spray angle.

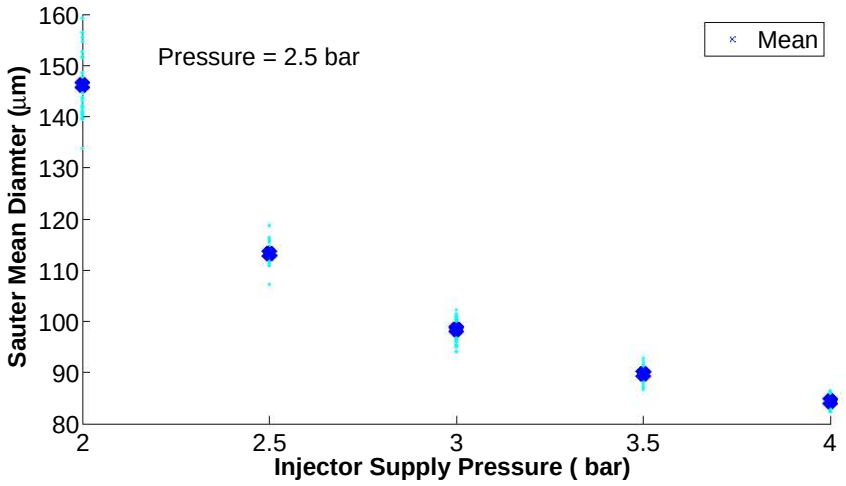

Figure D.6: Pressure effects on SMD for iso-octane

Spray Symmetry

A sweep of readings perpendicular to the spray axis was taken to assess the symmetry of the spray cone. Figure D.7 illustrate these results.

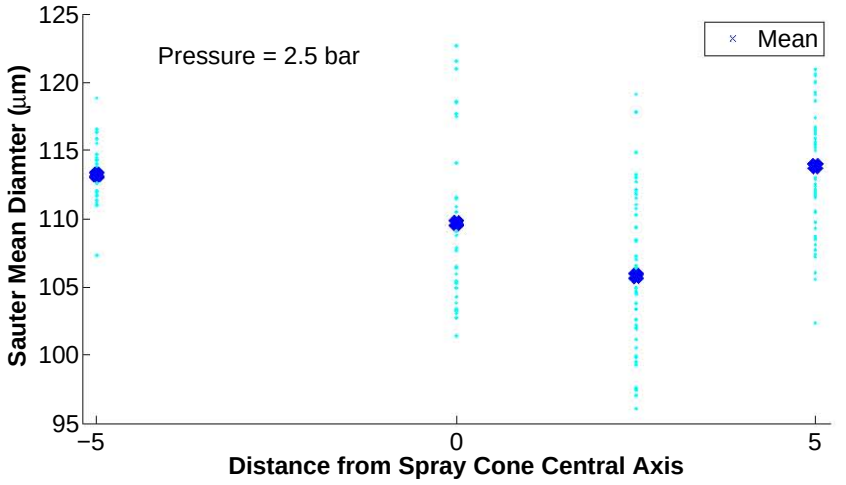

Figure D.7: Spray symmetry for iso-octane

The distribution is shown to be largely symmetric around the cone axis.

Comparison with previous research

These results can be seen to fall within the range provided by literature. Lenz et al. [97] used a Malvern Particle sizer to characterise a pintle type injector operating on n-Heptane at an axial distance of 50 mm. This study showed that the SMD of the droplet distribution ranged from approximately 100 to 200 μm, depending on the timing of the measurement after the start of each injection pulse.

D.2.3 Influence of fuel types on SMD

The influence of fuel types on the spray characteristics was determined through the use of Hiroyasu et al.'s [100] empirical correlation of SMD for low pressure fuel injectors, seen in Equation D.1.

$$d_{32} = 4.12 d_{nozz} Re^{0.12} We^{-0.75} \left(\frac{\mu_f}{\mu_g}\right)^{0.54} \left(\frac{\rho_f}{\rho_g}\right)^{0.18} \tag{D.1}$$

The Reynolds and Weber number are given respectively by

$$Re = \frac{\rho_f U_{inj} d_{nozz}}{\mu_f} \tag{D.2}$$

$$We = \frac{\rho_f {U_{inj}}^2 d_{nozz}}{\sigma} \tag{D.3}$$

where	d_{32}	:	Sauter mean diameter
	d_{nozz}	:	nozzle diameter
	Re	:	Reynolds number
	We	:	Weber number
	μ	:	dynamic viscosity
	ρ	:	density
	U_{inj}	:	injection speed
	σ	:	surface tension
subscripts:	f	:	fuel
	g	:	gas

Rearrangement of Equation D.1 produces Equation D.4. This assumes that volume flow rate is constant for the fuels.

$$d_{32} = {\rho_f}^{-0.45} {\mu_f}^{0.42} {\sigma_f}^{0.75} K \tag{D.4}$$

The difference in SMD can then be determined relative to iso-octane, illustrated for ethanol in Equation D.5.

$$\frac{(d_{32})_{eth}}{(d_{32})_{oct}} = \left(\frac{(\rho_f)_{eth}}{(\rho_f)_{oct}}\right)^{-0.45} \left(\frac{(\mu_f)_{eth}}{(\mu_f)_{oct}}\right)^{0.42} \left(\frac{(\sigma_f)_{eth}}{(\sigma_f)_{oct}}\right)^{0.75}. \tag{D.5}$$

The difference in resulting SMD after using the appropriate fuel properties can be seen in Table D.3.

Table D.3: Fuel effects on Sauter mean diameter

Fuel	Change in SMD, relative to iso-octane
toluene	+ 5%
ULP 95	- 6%
ethanol	+ 20%

D.2.4 Influence of Ambient Air Speed on SMD

All tests were conducted in stagnant ambient air. However, air velocity in the intake manifold influences atomization. Figure D.8, reproduced from Lenz et al. [97] shows the influence of the mean intake velocity on the average SMD measured.

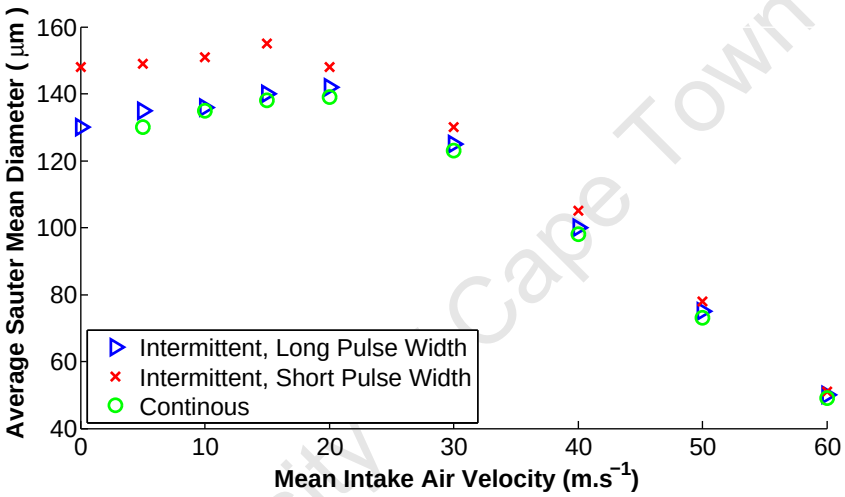

Figure D.8: Influence of air speed on atomization [97]

Based on this, it was decided to keep the initial SMD constant, as the air speeds seen within the manifold were not expected to go above 20 m.s^{-1} with the 4000 RPM air speeds to be of the order of 10 m.s^{-1}.

D.2.5 SMD Values used for Modelling

The value of 100 μm was chosen as the representative SMD for iso-octane at 3 bar supply pressure. A value 120 μm was chosen for ethanol, to account for the 20 % increase in SMD predicted by Equation D.1.

Appendix E

Inlet Manifold Modelling

This chapter details the various relations used in the modelling of the evaporation process that occurs in the inlet manifold. This is achieved through a model that comprises of empirical relations for the heat, mass and momentum transfer that occurs throughout this process.

For ease of use sake, certain details described in the main body are reproduced here.

E.1 Overview

The mathematical model describing the inlet manifold evaporation was required to predict the associated temperature drop of the inlet charge.

The process within the inlet manifold is a highly dynamic process, with rapidly fluctuating pressures occurring throughout the manifold with two-phase flow occurring. However, it was decided that a well thought out one-dimensional model would be able to provide sufficient prediction of the bulk processes at hand. This approach has been used before for this type of modelling [43, 65, 69].

A one-dimensional steady state model was thus chosen. The model is a multiphase model consisting of three zones, namely a film, gas and droplet zone. This is illustrated in Figure E.1, where the interactions that cause a rate of change of mass ($\dot{m}$), heat ($\dot{Q}$) and momentum ($\dot{m}v$) are shown.

Mass, heat and momentum are transferred between all three zones through classic transport equations. The model includes interactions between the manifold wall and the film and gas zone.

The starting conditions of the gas zone were determined from measurement. The droplet zone starting conditions are determined by the characterisation of the injector spray (detailed in Appendix D.2), while the film condition starting conditions were estimated.

The method used to model the evaporation process, as reviewed in Chapter 2.7.3, was the film theory model, while heat transfer was modelled using the infinite conductivity model. This is the same manner as the previous modelling studies referenced earlier

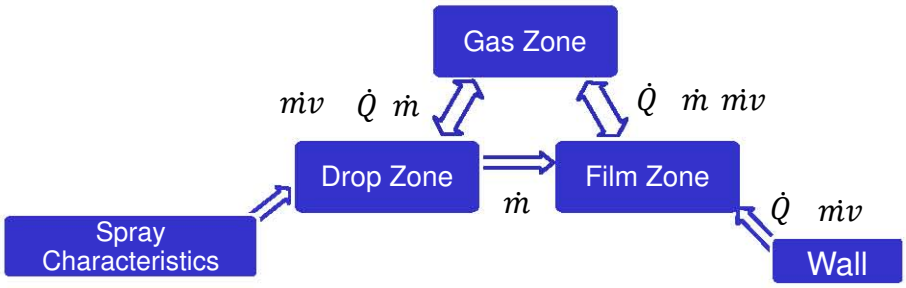

Figure E.1: Schematic of inlet manifold model

[43, 65, 69]. Wall film motion was accounted for through momentum interactions between the gas and film zone. Droplet deposition was also accounted for and made use of the Friedlander and Johnstone relation as described in Chapter 2.7.5.

This model consisted of a so called initial value problem, which consists of a set of ordinary differential equations with the initial values of the functions specified. This was solved through the use of the Runge-Kutta method.

E.2 Governing Equations

The equations were derived through a zonal balance of energy, mass and momentum for the steady state flow of the fluids through the manifold, thus ignoring time. This was done in line with previous models, which can be referenced for further information [43, 53, 54, 61, 65, 69].

Conservation of Energy

This details the effects of the energy transferred on the internal energies of each zone through heating and enthalpy changes due to mass transfer (The influence of the kinetic energy of the mass transferred between zones was ignored, as it was assumed to be of minor significance.)

The conservation of energy equations allow for the prediction of the change in temperature of each zone.

Droplet Zone

$$\dot{m}_d c_{p,d} \frac{dT_d}{dx} = \frac{dQ_{g2d}}{dx} - \frac{d\dot{m_{d2g}}}{dx} h_{fg,d} \tag{E.1}$$

Gas Zone

$$\dot{m}_g c_{p,g} \frac{dT_g}{dx} = -\frac{dQ_{g2w}}{dx} - \frac{dQ_{g2f}}{dx} - \frac{dQ_{g2d}}{dx} \tag{E.2}$$

Film Zone

$$\dot{m}_f c_{p,f} \frac{dT_f}{dx} = \frac{dm\dot{}_{d2f}}{dx} c_f (T_d - T_f) - \frac{dQ_{w2f}}{dx} - \frac{dQ_{f2g}}{dx} - \frac{dm\dot{}_{f2g}}{dx} h_{fg,f} \tag{E.3}$$

where
T : temperature
$\dot{m}$: rate of mass transfer
Q : rate of heat transfer
c_p : constant pressure specific heat
x : distance
h_{fg} : enthalpy of vapourisation

subscripts:
f : film zone
g : gas zone
d : droplet zone
w : wall zone
$g2d$: transport from gas to droplet zone etc

Conservation of Mass

This details the effects of the mass transferred between zones, through evaporation of the film and droplets and impingement of the droplets onto the film.

This allows for the prediction of the change of the droplet diameter, film thickness and gas density.

Droplet Zone

$$(\frac{1}{2}\rho\pi n D^2)\frac{dD}{dx} = -\frac{dm\dot{}_{d2g}}{dx} \tag{E.4}$$

Gas Zone

$$\rho_g \frac{d\rho_g}{dx} = (\frac{1}{A_g v_g \rho_g}\left(\frac{dm\dot{}_{d2g}}{dx} + \frac{dm\dot{}_{f2g}}{dx}\right) - \frac{A_g}{dx}\frac{1}{A_g} - \frac{dv_g}{dx}\frac{1}{v_g} \tag{E.5}$$

Film Zone

$$(v_f \pi d_m)\frac{dt_f}{dx} = \frac{1}{\rho_f}\left(\frac{dm\dot{}_{d2f}}{dx} - \frac{dm\dot{}_{f2g}}{dx}\right) - \frac{dv_f}{dx}\pi d_m t_f \tag{E.6}$$

where	D	:	diameter of droplet
	n	:	number of droplets passing per second
	t_f	:	thickness of film
	$\dot{m}$	:	mass transfer
	x	:	distance
	v	:	speed
	ρ	:	density
	A	:	cross sectional area
	d_m	:	diameter of manifold pipe
subscripts:	f	:	film zone
	g	:	gas zone
	d	:	droplet zone
	w	:	wall zone
	$g2d$	:	transport from gas to droplet zone etc

Conservation of Momentum

This section details the effects of the momentum influences between the zones, where interaction occurs through friction and drag forces between the gas and the film and droplet zones respectively, as well as the influence of the momentum transfer when mass is transferred.

This allows for the prediction of the velocities of the various zones.

Droplet Zone

$$(\frac{1}{6}n\pi D^3\rho)\frac{dv_d}{dx} = \tau_{gd}\frac{n}{v_d} \tag{E.7}$$

Gas Zone

$$\rho_g A_g v_g \frac{dv_g}{dx} = A_g\frac{dp_g}{dx} - \tau_{gf}s_g - \tau_{gw}s_w - \dot{m}_d\frac{dv_d}{dx} + v_d\left(-\frac{dm\dot{}_{d2g}}{dx} - \frac{dm\dot{}_{d2f}}{dx}\right) - v_g\left(\frac{dm\dot{}_{d2g}}{dx} - \frac{dm\dot{}_{f2g}}{dx}\right) \tag{E.8}$$

Film Zone

$$\dot{m}_f\frac{dv_f}{dx} = \tau_{gf}s_f - \tau_{wf}s_f - v_f\left(\frac{dm\dot{}_{d2g}}{dx} - \frac{dm\dot{}_{f2g}}{dx}\right) \tag{E.9}$$

where	D	:	diameter of droplet
	n	:	number of droplets passing per second
	$\dot{m}$	:	mass transfer
	τ	:	shear force
	s	:	perimeter
	x	:	distance
	v	:	speed
	p	:	pressure
	ρ	:	density
	A	:	cross sectional area
subscripts:	f	:	film zone
	g	:	gas zone
	d	:	droplet zone
	w	:	wall zone
	$g2d$	:	transport from gas to droplet zone etc

Ideal Gas Law

A derivative form of the ideal gas law was required to determine the change in pressure of the gas from the change in gas temperature and density.

$$\frac{1}{p_g}\frac{dp_g}{dx} = \frac{1}{\rho_g}\frac{d\rho_g}{dx} + \frac{1}{T_g}\frac{dT_g}{dx} \tag{E.10}$$

where	T	:	temperature
	x	:	distance
	v	:	speed
	p	:	pressure
	ρ	:	density
subscripts:	f	:	film zone
	g	:	gas zone
	d	:	droplet zone
	w	:	wall zone
	$g2d$	:	transport from gas to droplet zone etc

Mass Transfer Relations

The mass transfer through evaporation from the droplet to the gas is given by:

$$\frac{d\dot{m_{d2g}}}{dx} = \pi D \overline{\rho_d} D_{AB} Sh \ln(1 + B_M)\frac{n}{v_d} \tag{E.11}$$

where the Spalding number is given by:

$$B_M = \frac{\omega_{vs} - \omega_{v\infty}}{1 - \omega_{vs}} \tag{E.12}$$

and the Sherwood number is given by

$$Sh = 2 + 0.6{Re_d}^{0.5}{Sc_g}^{0.33} \tag{E.13}$$

The mass transfer through evaporation from the film to the gas is given by:

$$\frac{d\dot{m_{f2g}}}{dx} = \pi D_f \overline{\rho_f} D_{AB} Sh_f B_{M,f} \tag{E.14}$$

where the Spalding number for the film is given by:

$$B_{M,f} = \frac{p_{sat,f} - p_v}{p_g} \tag{E.15}$$

and the Sherwood number for a film is given by:

$$Sh_f = 0.023{Re_m}^{0.8}{Sc_g}^{0.4} \tag{E.16}$$

The mass fractions at the surface of a liquid zone or in the free stream is determined using Raoults law and converting the resulting mole fraction to a mass fraction:

$$y = \frac{p_v}{p_g} \tag{E.17}$$

The property $\overline{\rho}$ indicate a representative average property (density in this case) in the boundary layer of the droplet and film. This is determined using an averaging parameter A_r at the reference conditions $\overline{T}$ and $\overline{\omega}$.

$$\overline{T} = T_s + A_r(T_\infty - T_s) \tag{E.18}$$

$$\overline{\omega} = \omega_s + A_r(\omega_\infty - \omega_s) \tag{E.19}$$

The suggested value for A_r is $\frac{1}{3}$ (the so called '1/3' rule).

where	D	:	diameter of droplet
	D_{AB}	:	mass diffusivity
	n	:	number of droplets passing per second
	t	:	thickness
	$\dot{m}$	:	mass transfer
	x	:	distance
	v	:	speed
	ρ	:	density
	ω	:	mass fraction
	y	:	mole fraction
	Re	:	Reynolds number
	Sc	:	Schmidt number
	A_r	:	averaging parameter
	ν	:	kinematic viscosity
	d_m	:	diameter of manifold pipe
subscripts:	f	:	film zone
	g	:	gas zone
	d	:	droplet zone
	v	:	liquid in vapour form
	w	:	wall zone
	∞	:	free stream property
	s	:	saturated vapour gas interface property
	m	:	manifold
	$g2d$	:	transport from gas to droplet zone etc

Heat Transfer Relations

The heat transfer from the gas to droplet is given by

$$\frac{dQ_{g2d}}{dx} = S_d h(T_g - T_d)\frac{n}{v_d} \tag{E.20}$$

where the heat transfer coefficient is determined from the definition of the Nusselt number:

$$Nu = \frac{hD}{k_g} \tag{E.21}$$

where the Nusselt number is determined from the Frossling correlation:

$$Nu = 2 + 0.5276 Re_d^{\frac{1}{2}} {Pr_g}^{\frac{1}{3}} \tag{E.22}$$

The heat transfer from the wall to the film is given by

$$\frac{dQ_{w2f}}{dx} = s_w h_{w2f}(T_w - T_f) \tag{E.23}$$

where the heat transfer coefficient is given by

$$h_{w2f} = \frac{k_f}{t_f} \tag{E.24}$$

The heat transfer from the gas to the film is given by

$$\frac{dQ_{g2f}}{dx} = s_f h_{g2f}(T_g - T_f) \tag{E.25}$$

where the heat transfer coefficient is given by

$$h_{g2f} = \frac{Nu_{g2f} k_f}{d_m} \tag{E.26}$$

with the Nusselt number for this being

$$Nu_{g2f} = 0.023 Re_m^{0.8} Pr_g^{0.4} \tag{E.27}$$

The heat transfer from the gas to the wall is given by

$$\frac{dQ_{g2f}}{dx} = s_{w,exposed} h_{g2w}(T_g - T_w) \tag{E.28}$$

where the heat transfer coefficient is given by

$$h_{w2f} = \frac{Nu_{g2w} k_g}{d_m} \tag{E.29}$$

with the Nusselt number for this being

$$Nu_{g2w} = 0.023 Re_m^{0.8} Pr_g^{b} \tag{E.30}$$

where $b = 0.4$ for heating and $b = 0.33$ for cooling.

where	T	:	temperature
	$\dot{m}$	:	rate of mass transfer
	Q	:	rate of heat transfer
	c_p	:	constant pressure specific heat
	x	:	distance
	h	:	heat transfer coefficient
	k	:	thermal conductivity
	Re	:	Reynolds number
	Pr	:	Prandtl number
	S	:	surface area
	D	:	diameter of droplet
	d	:	diameter
	t	:	thickness
	s	:	perimeter
subscripts:	f	:	film zone
	g	:	gas zone
	d	:	droplet zone
	w	:	wall zone
	$g2d$	:	transport from gas to droplet zone etc

Momentum Transfer Relations

The shear force on the droplets by the gas is given by:

$$\tau_d = \frac{1}{2} C_D \rho_g \left(v_g - v_d\right) \left|v_g - v_d\right| \tag{E.31}$$

where the drag coefficient is given by

$$C_D = 2.3 {Re_d}^{-0.37} \tag{E.32}$$

The shear force of the gas on the film is given by;

$$\tau_{g-f} = \frac{1}{2} f \rho_g \left(v_g - v_{fs}\right) \left|v_g - v_{fs}\right| \tag{E.33}$$

where the Fanning friction factor is given by:

$$f = \frac{16}{Re} \qquad \text{when} \qquad Re < 3000 \tag{E.34}$$

$$f = 0.0053333 + 7.0364 \times 10^{-7} (Re - 3000) \qquad \text{when} \qquad 3000 < Re < 4000 \tag{E.35}$$

$$f = \frac{0.0791}{Re^{0.25}} \qquad \text{when} \qquad Re > 4000 \tag{E.36}$$

This equation is also used for drag between the gas and the wall, with a zero velocity replacing the film zone velocity.

The drag on the film by the wall is given by:

$$\tau_{w-f} = 2\mu_f \frac{u_{fm}}{t_f} \tag{E.37}$$

where	τ	:	shear force
	μ	:	dynamic viscosity
	t	:	thickness
	v	:	speed
	ρ	:	density
	A	:	cross sectional area
	Re	:	Reynolds number
subscripts:	f	:	film zone
	g	:	gas zone
	d	:	droplet zone
	w	:	wall zone
	$g2d$	:	transport from gas to droplet zone etc

Dimensionless Numbers

The various dimensionless numbers used are as follows:

$$Pr_g = \frac{c_{p,g}\mu_g}{k_g} \tag{E.38}$$

$$Re_d = \frac{D|v_g - v_d|}{\nu_g} \tag{E.39}$$

$$Re_m = \frac{d_m|v_g - v_f|}{\nu_g} \tag{E.40}$$

$$Sc_g = \frac{\nu_g}{D_{ab}} \tag{E.41}$$

Appendix F

Engine Breathing - Model and Data

A review of the breathing process was undertaken to better understand the engine operation through the use of a model together with the in-cylinder pressure trace information. The presence of transducer overheating was clearly displayed by the breathing data.

F.1 Breathing Model

F.1.1 Overview

The model of the breathing process, namely the exhaust and intake strokes, in the engine was based on a force balance across a “unit” or “slug” of charge entering the engine at each time step, and relating this to the rate of change of momentum of this “slug” of charge.

The various pressure drops due to friction, elbows and discharge were accounted for through classic empirical relations.

The coefficients involved in the determining of the magnitude of the pressure losses were used as tuning coefficients to match the model to the specific inlet dynamics of the engine. These coefficients, while having physical significance, were expected to loose this significance during the tuning process as the complexity of the breathing process (especially with the untuned inlet manifold that was present) and the simplicity of the breathing model would necessitate this.

This method allowed for the determination of the mass flow into and out of the cylinder. This mass flow was checked for sonic choking at the valve and corrected if necessary.

An energy balance was applied to the cylinder, relating the change of energy internal energy of the system to the enthalpy changes due to the mass transfer and heat transfer with the cylinder walls.

The breathing model implemented was taken in large from the content of the course Engine Thermodynamics and Combustion [79].

F.1.2 Governing Equations

Mass Flow Calculation

A force balance was applied to a "slug" of air in the inlet manifold of length L. Relating this to the rate of change of momentum across the "slug" of air results in:

$$\sum F = \frac{m\Delta v}{\Delta t} \tag{F.1}$$

The force acting on a 'slug' of air is given by:

$$\sum F = [(p_{mani} - p_{cyl})A_{valve} - \Delta p_{pipefric}\pi D_{mani}L_{mani} - \Delta p_{elbowfric}A_{mani} - \Delta p_{valvefric}A_{valve} \tag{F.2}$$

The pressure losses were accounted for through the following relations:

$$\Delta p_{pipefric} = \frac{1}{2}K_{f,mani}\rho_{mani}{v_{i-1}}^2 \Delta p_{elbowfric} = \frac{1}{2}K_{elbow}\rho_{mani}{v_{i-1}}^2 \Delta p_{valvefric} = \frac{1}{2}K_{valve}\rho_{mani}{v_{i-1}}^2 \tag{F.3}$$

The velocity of the system can subsequently be solved for

$$v_i = v_{i-1} + \tag{F.4}$$

$$\frac{\left[(p_{mani} - p_{cyl})\, A_{valve} - \frac{1}{2}K_{f,mani}\rho_{mani}{v_{i-1}}^2\pi D_{mani}L - \frac{1}{2}K_{elbow}\rho_{mani}{v_{i-1}}^2 A_{mani} - \frac{1}{2}K_{valve}\rho_{mani}{v_{i-1}}^2 A_{mani}\right]\Delta t}{\rho_{mani}A_{mani}L}$$

If the speed at the valve exceeded the sonic limit of $a = \sqrt{\gamma RT}$, the speed was limited to the sonic limit.

The mass flowing through each valve for each time step is thus:

$$\delta m = \rho A v \delta t \tag{F.5}$$

Conservation of Mass

Applying a mass balance to the control volume produces:

$$m_i = m_{i-1} + \sum \delta m \tag{F.6}$$

Conservation of Energy

Applying an energy balance to an open control volume produces:

$$\Delta U_{vol} = Q_{in} - W_{out} - \Delta H_{out} \tag{F.7}$$

The cylinder was treated as an open control volume and applying an energy balance as in Equation F.7 for each time step, and with rearrangement produces:

$$m_{u,i}u_{u,i} - m_{u,i}u_{u,i} + 0.5(p_i + p_{i-1})(V_{u,i} - V_{u,i-1}) - h_{in}\delta m_{in,i} - h_{ex}\delta m_{ex,i} - h_{cyl,i}\delta m_{cyl,i} = 0 \tag{F.8}$$

The ideal gas law was applied to the zone as well:

$$\frac{TR_u m_{u,i}}{M_{u,i}} - p_i V_{u,i} = 0 \tag{F.9}$$

where
F : force
m : mass
v : speed
Δt : time increment
p : pressure
A : area
L : length
K : loss coefficient
γ : ratio of specific heats
R : universal gas coefficient
ρ : density
U : internal energy
W : work
H : enthalpy
Q : heat transfer
h : specific enthalpy
M : molar mass

subscripts:
i : time increment
u : unburnt zone
in : inlet manifold gas
ex : exhaust manifold gas

F.2 Breathing Data

Figure F.1 shows sample breathing traces for each respective speed with the motored trace and the pressure from within the inlet manifold overlaid. These dynamics did not

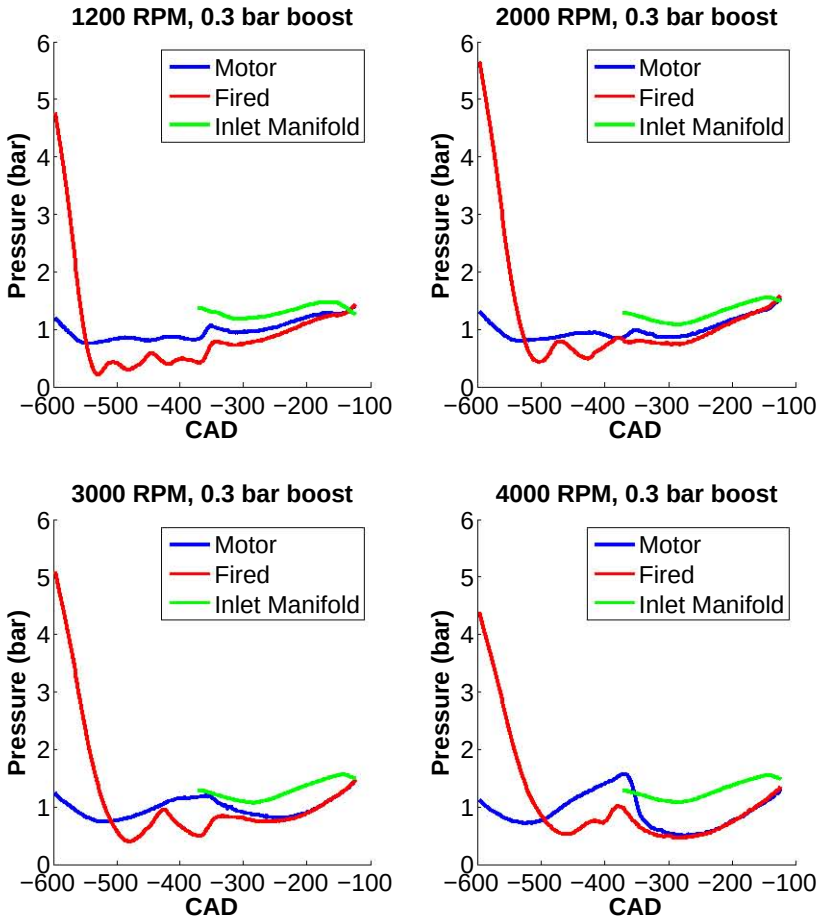

Figure F.1: Breathing traces - PFI conditions, 10 kPa boost

alter between manifold cases nor boost pressures. The boost pressure merely raised or lowered the overall pressure.

Table F.1 shows the valve timing for the engine, thus the traces shown are from from Exhaust Valve Open (EVO) to IVC.

Table F.1: Engine valve timing

IVO	-372 CAD
IVC	-124 CAD
EVO	-596 CAD
EVC	-348 CAD

The influence of the pressure transducer overheating is immediately apparent, as the pressure in-cylinder is recorded to drop below atmospheric during the exhaust stroke. Additionally, the motored trace shows higher pressure, despite experiencing lower exhaust pressure due to the lack of combustion. The inlet manifold trace further highlights that the pressure seen within the boosted inlet manifold is even higher.

The fired data and motored data do meet up again at the end of the inlet stroke. This shows that the pressure transducer heating effects have worn off by that stage in the cycle and realistic readings are once again recorded.

Figure F.2 compares the model to the pressure traces within the cylinder. The model struggled to simulate the breathing process. While the inlet portion was simulated with fair accuracy, the model struggled with the initial exhaust process with its pressure fluctuations.

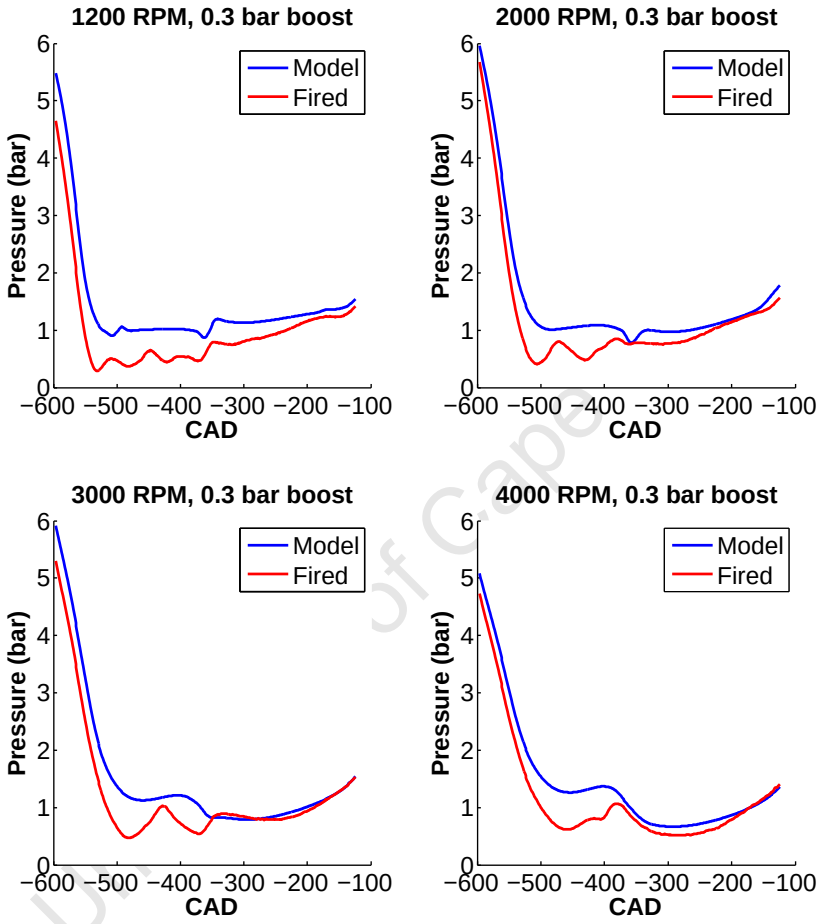

Figure F.2: Comparison of breathing model and data trace

In particular, it struggled to simulate across the speed range. The fits shown are a best compromise across the speeds. A model fit that more closely represented the particular pressure waves present could be achieved for a single speed, however this then would decrease the fit accuracy at the other speeds.

The complex breathing dynamics across the speed range clearly requires a more complex breathing model formulation, as opposed to the model used, which is a relatively simple formulation that ignores such influences as viscosity.

The model was required however to provide some insight into the possible REG fraction that would be present at IVC. Table F.2 shows the predicted values. The model

predicted very low REG values as well as REG values that increase with speed. These two findings were used in the combustion modelling process.

Table F.2: REG at IVC predicted by breathing model

Speed (RPM)	REG (%)
1200	3.0%
2000	2.6%
3000	3.4%
4000	4.2%

Appendix G

Thermodynamic properties

This chapter details the calculation of the various thermodynamic properties used through the study as well as the determination of the influence of dissociation on the combustion gas constituency.

The combustion and breathing model required the determination of the specific heat at constant pressure (c_p), internal energy (u), enthalpy (h) and entropy (s) of the various AF (burnt and unburnt) mixtures encountered throughout the processes.

G.1 Specific Heat

The specific heat was calculated from the the coefficients supplied by the JANAF tables [101] applied to the fit of the form:

$$c_p = a_0 + a_1 T + a_2 T^2 + a_3 T^3 + a_4 T^4 \tag{G.1}$$

where c_p : specific heat
T : temperature
a : fitting coefficient

G.2 Enthalpy and Internal Energy

The enthalpy of state at a temperature T is given by:

$$h_{state}|_T = h_{formation}|_{0K} + h_{sensible}|_T \tag{G.2}$$

where the $h_{formation}|_{0K}$ can be determined from the JANAF table values [101], as it is given by

$$h_{formation}|_{0K} = h_{formation}|_{298K} - h_{sensible}|_{298K} \tag{G.3}$$

The enthalpy of state can then be determined from the c_p relation mentioned above, as enthalpy can be calculated from specific heat as follows:

$$C_p = (\frac{\partial h}{\partial T})_p \tag{G.4}$$

$$\therefore h_{sensible}|_T = \int_0^T c_{p,(T)} dT \tag{G.5}$$

By integrating Equation G.1 we can thus derive the sensible enthalpy:

$$h_{sensible}|_T = a_0 T + \frac{a_1}{2}T^2 + \frac{a_2}{3}T^3 + \frac{a_3}{4}T^4 + \frac{a_4}{5}T^5 \tag{G.6}$$

The internal energy is obtained from the simple relation of:

$$u = h - RT \tag{G.7}$$

where u : internal energy
T : temperature
h : enthalpy
R : universal gas constant

G.3 Entropy

The entropy of state at a temperature T is similarly given by:

$$s_{state}|_T = s_{formation}|_{0K} + s_{sensible}|_T \tag{G.8}$$

To determine the $s_{sensible}|_T$, a relation that relates it to the enthalpy was used.

Since

$$h = u + pv \tag{G.9}$$

we can then say

$$dh = du + pdv + vdp \tag{G.10}$$

Using the definition of entropy under adiabatic conditions

$$ds = \frac{dQ}{T} \tag{G.11}$$

and from the conversation of energy where

$$dq = du + Pdv \tag{G.12}$$

Combining these and rearranging

$$ds = \frac{dh}{T} - \frac{vdP}{T} = \frac{C_p dT}{T} - \frac{RdP}{R} \tag{G.13}$$

Entropy can thus be calculated from the enthalpy and specific heat relations mentioned earlier, as integrating the previous equation

$$s_{sensible}|_T = \int_0^T \frac{C_p}{T} dT - R \int^p 2_p 1 \frac{1}{P} dP \tag{G.14}$$

and substituting in the relations for C_p produces

$$s_{sensible}|_T = a_0 \ln T + a_1 T + \frac{a_2 T^2}{2} + \frac{a_3 T^3}{3} + \frac{a_4 T^4}{4} \tag{G.15}$$

and similarly as the enthalpy, the $s_{formation}|_{0K}$ is determined from values from the JANAF tables.

G.4 Gibbs Free Energy

The Gibbs energy is calculated from the definition as

$$g^0 = h^0 - T^0 s^0 \tag{G.16}$$

where h^0, T^0 and s^0 denote the values at the reference pressure of 1 atm.

G.5 Other Properties

A number of temperature dependent properties were calculated using the fits supplied by [102]. These properties were:

1. Liquid density (ρ)
2. Vapour pressure (p_v)
3. Latent heat of vapourisation (h_fg)
4. Liquid and gas dynamic viscosity (μ)
5. Surface Tension (σ)
6. Thermal Conductivity (k_g)

Constant values at 25℃ were used for the diffusion coefficients (D_{AB}), obtained from [103].

G.6 Dissociation

The burnt zones chemical composition will be influenced by dissociation of the combustion products due to the zones high temperature. The carbon dioxide dissociation (Equation G.17) and the water-gas shift reaction (Equation G.18) were used to represent dissociation.

$$CO_2 \rightleftharpoons CO + \frac{1}{2}O_2 \tag{G.17}$$

$$CO + H_2O \rightleftharpoons CO_2 + H_2 \tag{G.18}$$

The overall reaction modelled was:

$$C_wH_xO_y + A(O_2 + 3.773N_2) \rightarrow aCO_2 + bH_2O + cCO + dO_2 + eH_2 + A(3.773N_2) \tag{G.19}$$

The five product coefficients were solved by solving a system of five equations, seen in Equation G.20, consisting of three mole balances and the equating of the equilibrium

constants for the two dissociation reactions.

$$\begin{aligned} a + c - w &= 0 \\ 2b + 2e - x &= 0 \\ 2a + b + c + 2d - y - 2A &= 0 \\ {K_{P1}}^{WGS} - {K_{P2}}^{WGS} &= 0 \\ {K_{P1}}^{COD} - {K_{P2}}^{COD} &= 0 \end{aligned} \tag{G.20}$$

The two expressions for two equilibrium constants were calculated from

$${K_{P1}}^{WGS} = \frac{ab}{cd} \tag{G.21}$$

$${K_{P2}}^{WGS} = e^{\frac{-\Delta G*}{R_u T}} \tag{G.22}$$

$${K_{P1}}^{COD} = \frac{cd^{\frac{1}{2}}}{a} \tag{G.23}$$

$${K_{P2}}^{COD} = e^{\frac{-\Delta G*}{R_u T}} \tag{G.24}$$

where the Gibbs free energy is calculated for the water gas shift reaction and the carbon dioxide dissociation from

$$\Delta G*^{WGS} = -{g_{CO}}^0 - {g_{H_2O}}^0 + {g_{CO_2}}^0 + {g_{H_2}}^0 \tag{G.25}$$

$$\Delta G*^{COD} = -{g_{CO_2}}^0 + {g_{CO}}^0 + 0.5{g_{O_2}}^0 \tag{G.26}$$

where	K	:	equilibrium constant
	R_u	:	universal gas constant
	T	:	temperature
	v	:	stoichiometric coefficients
	g^0	:	Gibbs free energy
superscripts:	WGS	:	water gas shift dissociation
	COD	:	carbon dioxide dissociation

Appendix H

Engine Start-up and Shut-down Procedures

H.1 Engine Start-up Procedure

1. Visually inspect the engine and subsystems for any loose connections, loose pipes, leaking fluids and possible short circuits.
2. Inspect the fuel drum and fuel system, ensuring that no leakage or loose fittings are present.
3. Turn the engine over for at least two revolutions to ensure that the engine and dynamometer are free to turn.
4. Check the engine oil level and the coolant level in the header tank.
5. If the PLC cabinet is off, switch it on.
6. If the control PC is off, turn it on and load the LabVIEW, Calview and Eta software.
7. Turn on the ventilation system for the test cell at the facility's main control board. This particular test cell does not have a dedicated ventilation/extraction system, and has to use the Heavy Duty (HD) test cell's system. Therefore, the switches must be turned on for the AHU1 (Auxiliary Handling Unit), the extraction fan and HD test cell.
8. Open the shut-off valve for the building's chilled water circulation system, which is located on the door next to the thyristor drive. Make sure that water is flowing into the test cell's drain from the fuel chiller unit's exit pipe. If there is no water flowing then the facility's water pumps must be turned on. The switches for the pumps are located on the facility's main control board in the control room.
9. Turn on the thyristor drive with the handle at the base of the unit, which is situated in the corner of the test cell.
10. Ensure that all charge amplifiers are connected to their respective pressure transducers.

11. Turn on the switches for the ECU box's power supply and charge amplifier, which is located beneath the electronics table that is located above the dyno.

12. Open the air extraction vent that is above the exhaust pipe. Close the IQT vent, which is located in the corner next to the thyristor drive. This will ensure that all exhaust gas is properly evacuated from the test cell and the engine is supplied with fresh air.

13. Close all the test cell doors. This is important for the ventilation system to function properly and to contain the engine noise.

14. On Eta, turn on the water and oil heaters and the water, oil and fuel pumps (The heaters do not work unless the pump switches are switched on). Wait 15min for the oil to reach at least 60℃ before starting the engine. Once the engine has reached its operating temperature, both heaters can be turned off. (The water heater is not designed to heat the engine to operating temperature, but rather help keep the engine at operating temperature when being motored)

15. If the AVL Indiset is disconnected or connected to the other test cell, disconnect these cables and connect the Hydra test cell cables.

16. Turn on the AVL Indiset using the switch located on the back panel. The Indiset is situated on top of a portable cabinet.

17. Check that oil pressure and coolant pressure is present and sufficient for operation.

18. Ensure that CalVIEW has connected to the target and then launch the host VI by clicking the play button.

19. Press the red Dyno 'RESET" button on Eta to reset the safety circuits and warning lights. The dyno will not start without first being reset. Once it has been running for a few seconds, the "RESET" light will turn off and the dyno will switch to "AUTO'.

20. Set the engine speed on Eta to its idle speed, 800 RPM.

21. Set the dyno controller switch to the "off" position. This will allow the dyno to automatically alternate between motoring the engine and absorbing torque and acts as an automatic engine control mode. Once the engine is operational, the dyno can be switched to absorb, which will prevent the dyno from attempting to motor the engine should the speed fluctuate, and will also give a better torque reading. The engine can also be run in the automatic mode.

22. Press the 'ON' button on the dyno controller to begin motoring the engine and use the speed setting to adjust the engine's speed to the desired value.

23. Eta and CalVIEW host VI should now be reading the engine speed, and the engine should be ready to start.

24. On the CalVIEW front panel, if any of the warning lights on the front panel indicate a fault (“Crank Stalled”, “Sync Stopped”, “Critical Fault” or “Non Critical Fault”), flip to the “Faults” tab or the “EPT” tab and click on the appropriate “Clear Faults’ button to reset them.

25. When you are ready to start the engine and you are certain that everything is in order, click the “Engine Run Enable’ button. This is a safety switch to ensure that nothing is accidentally turned on. If the “Engine Run Enable” button is not enabled, then all switches and controls will be disabled and you will be unable to engage any of the systems.

26. Flip to the “Main Engine Control” tab. This tab allows the user to control the throttle position, spark timing and fuel injection variables.

27. Make sure the throttle valve is open by increasing its angle and then enable the fuel injection.

28. Finally, enable the spark plug and slowly increase the fuel injection duration until combustion begins.

H.2 Engine Shut-down Procedure

1. On the CalVIEW front panel disable the fuel injection and then the spark plug.

2. To stop the dyno, press the “DYNO STOP” red button on the Eta control panel. The dyno will gradually slow until it stops.

3. Turn off the “DYNO ON” button.

4. Turn off the water and oil heaters and the fuel pump on Eta. However, the oil and water pumps should be left on to circulate and assist in cooling the engine.

5. Turn off the Indiset using the switch on its back panel. The Indiset is situated on top of a portable cabinet.

6. Turn off the switches for the ECU box’s power supply and charge amplifier, which is located beneath the electronics table that is located above the dyno.

7. Turn off the ventilation system for the test cell, which is located on the main control board in the control room. The AHU1, the extraction fan and HD test cell control switches must all be turned off.

8. Once the engine has cooled down, turn off the oil and water pumps on Eta.

9. Turn off the thyristor drive.

10. Close the shut-off valve for the facility’s chilled water circulation system, which is located on the door next to the thyristor drive. Turn off the pumps for the circulation system at the facility’s main control board.

11. Visually inspect the engine and subsystems for any loose connections, loose pipes, leaking fluids and possible short circuits in order to make sure that nothing has been damaged or has failed during testing. Walk around the test cell and double check that everything is off.

12. Eta, CalVIEW and Labview can be closed and the computer shut down if testing for the day has been completed.

13. Turn off the lights and close the test cell doors.